UNIVERSITÄT
DUISBURG
ESSEN

Open-Minded

Mechanical Properties of Antarctic Sea Ice

Felix Paul

UDEMAT
Institut für Materialwissenschaft Universität Duisburg-Essen

Mechanical Properties of Antarctic Sea Ice
Mechanische Eigenschaften von antarktischem Meereis

Von der Fakultät für Ingenieurwissenschaften
Abteilung Bauwissenschaften,
Institut für Materialwissenschaft
der Universität Duisburg-Essen

genehmigte Dissertation zur Erlangung des akademischen Grades
eines Doktor der Ingenieurwissenschaften (Dr.-Ing.)

vorgelegt von

M. Sc. Felix Paul
geboren in Essen

Datum der Einreichung: 30.05.2023
Datum der mündlichen Prüfung: 26.10.2023

Hauptreferent: Prof. Dr. rer. nat. habil. Doru C. Lupascu
Koreferent: Prof. Dr.-Ing. habil. Jörg Schröder

Essen 2023

DuEPublico
Duisburg-Essen Publications online

UNIVERSITÄT DUISBURG ESSEN
Offen im Denken

ub | universitäts bibliothek

Diese Dissertation wird via DuEPublico, dem Dokumenten- und Publikationsserver der Universität Duisburg-Essen, zur Verfügung gestellt und liegt auch als Print-Version vor.

DOI: 10.17185/duepublico/79241
URN: urn:nbn:de:hbz:465-20231106-075621-4

Alle Rechte vorbehalten.

Acknowledgement

I would like to emphasize that this research would not have been possible without the amazing support of several people.

First and foremost, I would like to express my profound gratitude to Professor Doru C. Lupascu for his patience and continuous support during my civil engineering studies, especially during my PhD. tenure. Without Professor Lupascu’s guidance, this work would not have been possible, I owe him a lot for making this PhD journey very special. I am extremely grateful for the support of Professor Jörg Schröder, who generously provided guidance and expertise, especially during the first research cruise on the SA Agulhas II and throughout my PhD programme. Besides that, special thanks go to Professor Carolin Birk for her role as chair of my doctoral examination committee.

Furthermore, I extend my gratitude to Professor Lupascu, and Professor Schröder for preparing the reports, and to Professor Angelika Humbert and Professor André Niemann for their roles as examiners.

However, I cannot overlook the pivotal role played by our partners at the University of Cape Town, South Africa. This endeavor simply would not have happened without Professor Marcello Vichi, who enabled me to discover the secrets of the Antarctic Marginal Ice Zone. He organized the three research cruises I joined and was the chief scientist on the SCALE Winter Cruises 2019 and 2022. His deep knowledge of the Marginal Ice Zone of the Antarctic has helped me to better understand the Southern Ocean and to conduct experiments that were adapted to its conditions during these research cruises. Additionally, in his role as chief scientist, he ensured that all experiments were carried out under optimal conditions. I would like to express my deepest gratitude to the Marine and Antarctic Research Centre for Innovation and Sustainability (MARiS) for the excellent cooperation across disciplinary boundaries.

Figure: Sea ice team on the SCALE Winter Cruise 2019.

Additionally, this project hinged on the generous support from the South African government, which finances the SCALE program. The SCALE cruises are funded by the South African National Research Foundation (NRF) through the South African National Antarctic Programme (SANAP) with contributions from the Department of Science and Innovation and the Department of Environmental Affairs.

In addition, I owe my deepest gratitude to Professor Sebastian Skatulla and Dr. Tokoloho Rampai for inviting me to the SCALE Cruises in 2019 and 2022. Their unwavering support in the extensive preparations of the cruises by providing scientific material and valuable knowledge was indispensable. Professor Skatulla served as the sea ice team leader during the SCALE Winter Cruise 2019, and Justin Pead assumed this role during the SCALE Spring Cruises 2019 and 2022. They both meticulously coordinated the different sea ice tests, from sampling, to storing and testing procedures. They ensured reliable results for all team members and minimized the physical stress.

I would like to express my sincere appreciation to the captains and the whole crew of the SA Agulhas II. The brave crew made the tests possible in the first place which has to be executed under adverse conditions, in storms, severe cold, and at night. Without this outstanding support, the experiments would not have been successful. Moreover, the part of the crew that was not directly involved in the experiments deserves my appreciation for the excellent service during the cruises.

Many thanks go to Dr. Tommy Mielke for the support during the SCALE Winter Cruise 2019, the construction of the polar laboratory, and countless valuable discussions about sea ice.

Special thanks are due to Dr. Carina Schwarz for her ongoing guidance and her valuable assistance in preparing the defense.

I am also thankful to Dr. Hans-Joachim Keck who inspired me with his dedicated work attitude during my studies and my PhD journey.

I would like to extend my sincere appreciation to my colleagues and friends from the University of Cape Town, namely Dr. Rutger Marquart, Riesna Audh, Ehlke Hepworth, Siobhan Johnson, Safiyyah Moos, Hayley Swait, Robyn Verrinder and Ashleigh Womack. Thank you for your scientific contribution and for making the hard work enjoyable. In particular, I would like to thank Dr. Rutger Marquart for the friendship that has developed and grown during the cruises and Riesna Audh for providing the salinity and temperature data of the sea ice.

I am also grateful to all my colleagues from UDEMAT and the department of civil engineering, particularly Tobias Kuhn, for their feedback and the precious time we have spent together.

Finally, this acknowledgement would not be completed without mentioning my family, especially my grandmother, brother, and mother. Above all, I am immensely grateful to Janina for her unwavering support in all my endeavors.

Abstract

Sea ice in the Antarctic is crucial for the global climate. Its seasonal variations are of significant importance for Antarctic bio-habitat, primary production, heat, and carbon dioxide uptake of the ocean. However, the annual sea ice cycle, with extensions and declines in the Southern Ocean, is not completely understood yet. One reason for this is the poor understanding of the mechanical properties of Antarctic sea ice, which differ from the ones of the Arctic sea ice. To overcome the gap, the rheological properties of frazil ice and the compressive strength of pancake ice as well as consolidated sea ice were measured during three SCALE cruises in the marginal ice zone of the Antarctic. Frazil ice, consisting of small ice crystals floating in water, is the first ice forming in the annual freezing cycle of the Antarctic. It later develops into consolidated pancake ice floes and afterward into a consolidated sea ice cover.

The rheological properties of frazil ice are determined with the help of a vane rheometer immediately after sampling the ice from the Southern Ocean. The flow curve of frazil ice can be separated into three phases: In the beginning (1) the shear stress increase caused by hooking of the crystals, followed by (2) a shear stress decrease caused by detangling of the crystals and ultimately (3) shearing between the crystals in the third phase. Frazil ice shows a shear thinning behavior in the third phase with a flow index of $n = 0.5$.

Sea ice compressive strength is tested with two different hand-driven compression jigs. Tests are performed at –10 °C after a short-time storage with a strain rate in the ductile-to-brittle transition zone, as this yields the highest strength. Compressive strength results are presented depending on porosity, brine volume, and sea ice depth. Sea ice strength is higher in spring than in winter, and Antarctic sea ice is generally weaker than its Arctic counterpart.

Kurzfassung

Das Meereis in der Antarktis spielt eine wichtige Rolle für das globale Klima. Die jahreszeitlichen Meereisschwankungen sind von großer Bedeutung für den Lebensraum Antarktis, sowie die Wärme- und Kohlendioxidaufnahme des Ozeans. Trotzdem ist der jährliche Meereiszyklus mit Ausdehnung und Rückgang des Eises im Südlichen Ozean jedoch noch nicht vollständig erforscht. Ein Grund dafür ist das mangelnde Verständnis der mechanischen Eigenschaften des antarktischen Meereises, die sich von denen der Arktis unterscheiden. Um diese Lücke zu schließen, wurden die rheologischen Eigenschaften von Frazil-Eis und die Druckfestigkeit von Pancake-Eis sowie von konsolidiertem Meereis während drei SCALE-Expeditionen in die Marginale Eiszone der Antarktis gemessen. Frazil-Eis, das aus kleinen, im Wasser schwimmenden Eiskristallen besteht, ist das erste Eis, welches sich im jährlichen Gefrierzyklus der Antarktis bildet. Später entwickelt es sich zu festem Pancake-Eis und danach zu einer konsolidierten Meereisdecke.

Die rheologischen Eigenschaften von Frazil-Eis werden mit Hilfe eines Vane-Rheometers direkt nach der Entnahme von Eisproben aus dem Ozean bestimmt. Die Fließkurve von Frazil-Eis lässt sich in drei Phasen unterteilen: (1) Anstieg der Scherspannung durch Verhaken der Kristalle, (2) Abnahme der Scherspannung durch Zerstören größerer Kristallagglomerationen und (3) Reibung zwischen den Kristallen in der dritten Phase. Frazil-Eis zeigt in der dritten Phase ein scherverdünnendes Verhalten mit einem Fließindex von $n = 0,5$.

Die Druckfestigkeit von Meereis wird mit zwei verschiedenen handbetriebenen Druckversuchen geprüft. Die Tests werden bei -10 °C nach kurzzeitiger Lagerung mit einer Dehnungsrate im Bereich des Übergangs von duktilem zu sprödem Bruch durchgeführt, da dies die höchsten Festigkeiten liefert. Die Ergebnisse der Druckfestigkeit werden in Abhängigkeit von Porosität, Salzgehalt und Meereistiefe dargestellt. Die Festigkeit des Meereises ist im Frühjahr höher als im Winter. Das antarktische Meereis ist im Allgemeinen schwächer als sein arktisches Gegenstück.

1 Table of Contents

List of Figures

List of Tables

Abbreviations

A_{crystal}	cm^2	Crystal area
C_{i}		Interstitial concentration
C_{v}		Equilibrium vacancy concentration
$E_{\mathrm{i}}^{\mathrm{f}}$	J	Energy to form an interstitial
$E_{\mathrm{v}}^{\mathrm{f}}$	J	Energy needed to place a molecule
F_{c}	kN	Compression load
k_{B}	J/K	Boltzmann's constant
k_{r}		Mass-ratio of solid salts and of salts in the brine
m_{ice}	kg	Ice weight
R_{v}	mm	Vane Radius
R_{s}	mm	Effective radius of the steel rod
S	kg	Salinity (Subscripts: b: brine; a: air; i: ice, s: salt; ss: solid salt)
S_{A}	kg	Absolute Salinity
S_{int}	J/K	Extra entropy associated with each interstitial
S_{p}	PSU	Practical Salinity Unit
S_{v}	J/K	Extra entropy associated with each vacancy
T_0	°C	Freezing point
T_{min}	°C	Minimum temperature
T_{r}	°C	Residual supercooling temperature
$\mathrm{V}_{\mathrm{ice,rel}}$	%	Relative ice content
$\mathrm{V}_{\mathrm{sam,abs}}$	dm3	Absolute sample volume
$\dot{\gamma}$	1/s	Strain/ shear rate
$\dot{\epsilon}$	1/s	Strain rate
ν_{T}	%	Total porosity
σ_{c}	MPa	Compressive stress
σ_{n}	MPa	Normal stress
τ_0	$\mathrm{N/m}^2$	Yield stress
ω_{magnet}	RPM	Rotation speed magnet stirrer

a		Lattice parameter
$\boldsymbol{b}$		Burgers vector
c_l	mm	Crack length
c		Lattice parameter
d_{ia}	mm	Diameter
d	m	Depth
E	GPa	Young's modulus
F	kN	Force
h	mm	Height
H	mm	Vane height
I		Ice (Subscipts: h: hexagonal, c: cubic)
k		Consistency index
$\boldsymbol{l}$		Disclocation line
l	mm	Sample length
m	kg	Mass (Subscripts: b: brine; a: air; i: ice, s: salt; ss: solid salt)
MIZ		Marginal Ice Zone
$\boldsymbol{n}$		Crystallograhic planes
n		Flow behavior index
P	Pa	Pressure
r	mm	Radius
$\boldsymbol{s}$		Sense vector
T	°C	Temperature
t	s	time
V	dm^3	Volume (Subscripts: b: brine; a: air; i: ice, s: salt; ss: solid salt)
α		Least square fit parameter
Δl	mm	Displacement
ϵ	%	Strain (Subscripts: T: total; e: elastic; d: delayed; v: viscous; c: crack)
η	Pas	Dynamic viscosity
ν	m^2/s	Kinematic viscosity
ρ	kg/m^3	Density (Subscripts: b: brine; a: air; i: ice, s: salt; ss: solid salt)
τ	N/m^2	Shear stress
ω	rev/s	Rotation speed

2 Introduction

Climate change is likely to warm the global surface average temperature by more than 1.5 °C above pre-industrial levels until the end of the 21st century [1]. The temperature rise is driven by an increase in greenhouse gases, such as water vapor, carbon dioxide, methane, nitrous oxide, and chlorofluorocarbons [2]. A rising temperature is affecting the whole world in general and especially the polar regions: consequences of global warming like ice losses and changes in the polar oceans will affect the entire world [3]. The lowest minimum sea ice extent, since sea ice satellite recording started 43 years ago, was recorded in February 2022 [4].

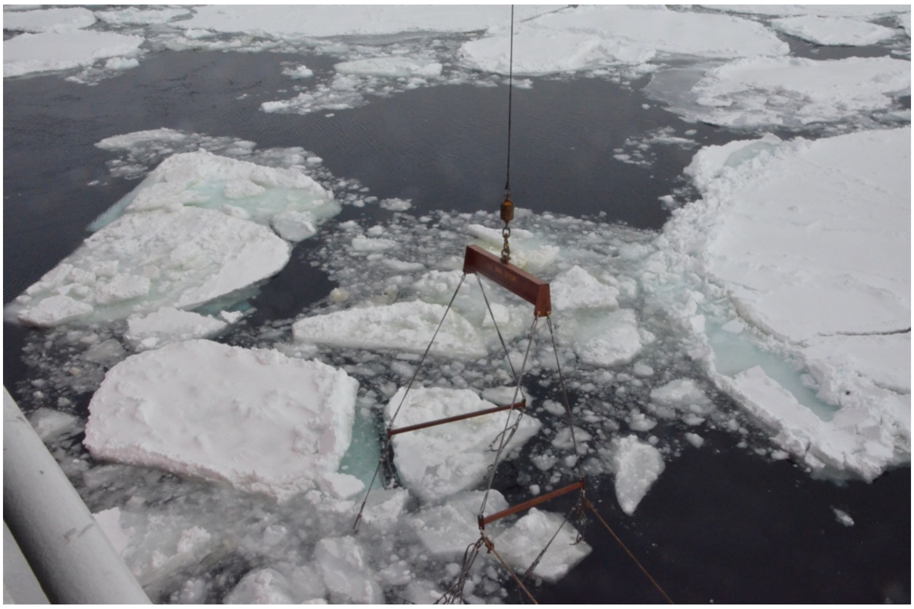

Figure 1 *Sampling of melting ice floes on the SCALE Spring Cruise 2019.*

As stated by the Intergovernmental Panel on Climate Change report about the polar regions [3], the southern ocean surrounding the Antarctic accounts for more than 35 % of the global ocean heat gain. Changes in sea ice thickness and concentration are affecting the chemical synthesis of organic compounds (primary production). Changes in primary production are associated with rapid sea ice changes, concentration and thickness, in the Southern Ocean. Nevertheless, no significant trend of changes in the sea ice concentration and thickness in the Southern Ocean are observed since satellite observations started. Furthermore, several computational models indicate a decrease in sea ice extent, even though no decreasing trend

is captured by satellites. Actually, a modest increase in the sea ice cover is recorded by satellites [5]. In contrast to that, Arctic sea ice decrease is observed and a relation between sea ice decrease, CO_2 emissions, and global temperature is captured in models. [3]
Computational models indicating the sea ice extent for the Antarctic region must be improved, as they cannot predict the sea ice changes in the past. In particular sea ice decreases in the Bellingshausen Sea and increases in the Ross Sea are not captured by current models [3]. A reason for the unprecise computational models could be the limited data available for the Antarctic region, compared to the Arctic region [6]. To overcome the lack of data, coordinated sampling campaigns need to be performed in the Antarctic. One attempt to improve the knowledge of Antarctic sea ice properties and behavior is this study.

In contrast to the Antarctic, a lot of sea ice research has been performed in the Arctic region [7]. One could argue that the mechanical properties of Arctic and Antarctic sea ice are similar and therefore the results of computational models are not affected by using ice properties from the Arctic for the Antarctic. However, this assumption is wrong. While the Arctic in large parts is covered by thick multi-year sea ice, the Southern Ocean surrounding the Antarctic is covered by a thin first-year sea ice cover as displayed in Figure 1 and Figure 2.

Figure 2 *Pancake ice floes floating in the ocean in the Marginal Ice Zone of the Antarctic.*

Until now, the Arctic is covered by a sea ice cover all year long, with a chance of an ice-free Arctic summer at the end of this century [3] due to global warming. The sea ice growth and retreat in the Antarctic on the other side is the largest annual surface cover change on earth [8]. Each year a sea ice cover of approximately 16 million km^2, which is similar to the size of Russia, freezes and melts in the Southern Ocean [9], [10]. The sea ice thickness in the Antarctic is limited to approximately one meter due to a high ocean heat flux, while ice in the Arctic can be several meters thick as the ocean heat flux is lower [11]. Due to its topographic configuration the Southern Ocean is subjected to strong westerly winds and atmospheric circulation, which are on average of a greater magnitude than in the Arctic region. Consequently, Antarctic sea ice growth is the result of turbulent sea conditions that strongly influence its initial phase occurring in the Marginal Ice Zone of the Antarctic. Hence, sea ice properties like brine content, air content, temperature, and inclusions are fundamentally different for the Arctic and Antarctic region, sea ice properties from the Arctic cannot be simply transferred to sea ice models of the Antarctic regions.

Climate affects the formation of sea ice. In the Marginal Ice Zone of the Antarctic, high winds and prominent wave activity in the ocean promote complex sea ice formation [12]. To better describe sea ice formation, its behavior and effect on the climate, insulating properties, gaseous exchange, and surface wave damping, Antarctic sea ice properties need to be further investigated.

The Marginal Ice Zone (MIZ) describes the interface region between the open ocean and pack ice [13] typically comprised of an unconsolidated mixture of heterogeneous ice floe types with a sea ice concentration between 15 % and 80 % and frazil ice in between [14]. Frazil ice comprises small ice crystals floating in the water, which later develop into ice floes, also called pancake ice floes. The MIZ sea ice-floe concentration and coverage fundamentally influence the atmosphere-ocean-sea ice interaction in the polar regions with their formation and coverage following seasonal cycles [15].

Figure 3 *Members of the sea ice team are preparing the ice surface for sea ice coring.*

Frazil ice, consisting of loose ice crystals floating in the water, are the first ice crystals forming in the annual freezing cycle of the MIZ of the Antarctic. Frazil ice crystals appear in an unregular disc-shaped form and grow under turbulent and supercooled conditions in the ocean. After some time, frazil ice crystals agglomerate at the ocean's surface and appear as a grey layer on top of the ocean and later develop into solid pancake ice floes. Frazil ice is situated in between the solid pancakes and acts like a binder between the pancake ice floes [16]. Close to the edge of the MIZ, large ocean waves, winds, and storms lead to fracture, overtopping, and rafting of pancakes. As soon as the ocean is sufficiently damped by the frazil/ pancake layer, a consolidated ice cover will form. This process is described as the pancake cycle [17].

A widely used model for sea ice behavior in the Marginal Ice Zone is the Hibler model [18]. A part to solve the Hibler model, is the non-linear viscous plastic material law presented in Equation 1. For the material law, the stresses are related to the strain rate $\dot{\epsilon}$ [19].

$$\sigma = 2\,\eta\,\dot{\epsilon} + (\xi - \eta)\mathrm{tr}(\dot{\epsilon})\mathrm{I} - \frac{P}{2}\mathrm{I} \qquad 1$$

With the strain rate tensor $\dot{\epsilon}$ and identity matrix I. Two different material properties are present in the material law: the sea ice viscosities ξ and η and maximum ice strength P. Valid, experimental determination of the material properties of sea ice, especially of the compressive strength and viscosity, significantly contribute to reliable computational models.

The aim of this study is to point out the mechanical properties of ice, in particular, the compressive strength of solid sea ice floes and solid consolidated ice as well as the viscosity of liquid frazil ice.

Only a few studies have determined the compressive strength of Antarctic sea ice [7], [20]. Of these two studies, only one conducted the compressive strength test at the ambient sampling temperature right after sampling, while the others conducted the test after a long time of storage.

The viscosity of frazil ice has never been determined in-situ before. All attempts were conducted in large laboratory tanks or with the help of buoy and SAR equipment. With these methods, wave attenuation is measured, and a viscosity parameter is calculated. Assumptions about the ice behavior are made beforehand.

The goal of this study is to contribute profound knowledge on the compressive strength and viscosity of Antarctic sea ice. The study is structured as followed.

Section 3 summarizes the properties of ice and defects in ice in general. The difference between the ductile and brittle failure of ice is pointed out. It is explained how the brine content is calculated with the help of salinity data, followed by the growth process of sea ice. The properties of frazil ice, pancake ice, and consolidated ice are explained and differences between them are pointed out.

Section 4 explains the methods used for this study. The section is separated into experiments conducted on the South African research vessel SA Agulhas II and experiments conducted in the laboratory. The devices and operating instructions to sample liquid and solid frazil ice are presented. Besides that, it is shown how the samples are prepared before testing them. A rheometer to determine the viscosity and two different compression devices are described. For the laboratory experiments, a setup to grow frazil ice crystals and a method to grow solid ice under controlled conditions are presented.

The results of the conducted experiments are presented in Section 5. Results for the compressive strength and Young’s modulus over three cruises are described and compared to each other. It is shown in how the compressive strength changes over the thickness and with varying brine volume. The shear stress and viscosity of frazil ice are plotted. A relationship is established between frazil ice content and shear stress.

The last section of this study is Section 6 where shortcomings of the measurement techniques are discussed, results are summarized and an outlook for future research is given.

3 Ice mechanics

The mechanical behavior of sea ice is affected by its crystal structure and the defects of the ice lattice. The structure of ice, the special features of sea ice, and its growth in the MIZ are explained. Results from previous researchers on the uniaxial compressive strength and viscosity are described.

3.1 Ice structure

Ice is understood as frozen water. It consists of interconnected water molecules, which take the form of different physical phases depending on pressure and temperature. Right now, there are 20 known crystalline phases of ice and several non-crystalline phases of ice [21]. For the crystalline phase of ice the oxygen atoms need to be in fixed position relative to each other. The hydrogen atoms must not be proton ordered, but they have to fulfill the ice rules. The ice rules describe, how protons are distributed within the ice lattice: Two protons must be near each oxygen atom, one proton must be on each hydrogen bond, each molecule is bonded to four other molecules and ice is proton disordered [22]. The three known non-crystalline phases are formed if H_2O is cooled with a cooling rate of about 10^6 K/s and the H_2O-molecules do not have enough time to build a crystalline lattice and therefore form an amorphous ice structure. Amorphous ice on earth only exists in laboratories, even though it is the most common form of ice in the universe [23].

From the 20 known crystalline phases of ice, four phases were found on earth under natural conditions. On the one hand cubic ice I_c is present in the upper atmosphere of the earth, ice VI is found in diamond inclusions and on the other hand ice VII is expected to be present in the earth subduction zones [21]. But the most common ice on earth is the hexagonal ice I_h, which one encounters for example in snowflakes, freezing lakes and sea ice. Due to the limited conditions under which ice I_c , VI and VII occur, only ice I_h will be of interest in this work [24].

The structure that forms while freezing depends on the forces between molecules. The crystals which are formed from water between 0 to -80°C and atmospheric pressure are thin plates with a hexagonal structure and dendritic arms. The most common method to determine the crystal structure is through X-ray diffraction. The first studies in this field were presented in the 1920s. Bragg concluded that each oxygen atom has to be at the gravity center of its four oxygen neighbors. The molecules are arranged at parallel planes called basal planes where the normal to the basal plane (0001) is the c-axis. The fastest growing direction of ice crystals is in the (0001) plane. [25]

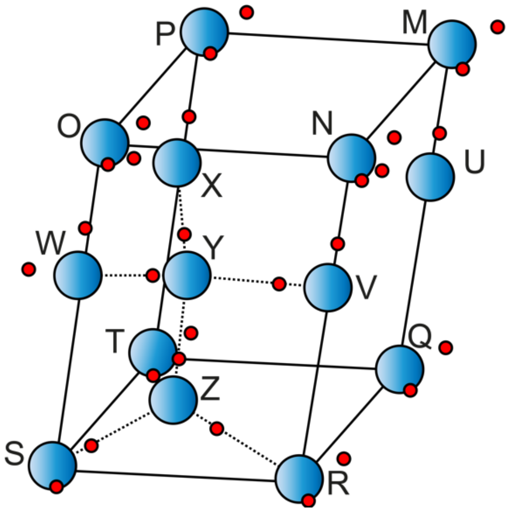

Figure 4 *Unit cell of ice* I_h*. According to* [26].

The unit cell (Figure 4) is the smallest repeating unit of a crystal and can be placed together as often as desired. The unit cell of the hexagonal ice consists of four oxygen atoms. The eight corners of the crystal unit cell (N; M; O; P; S; T; Q; R) each contain 1/8 of an atom. The edges each hold four 1/4 atoms (U; V; W; X) and in the centre are two complete atoms (Y; Z). This results in an open and light structure for the crystal. [26]

The sequence of molecular stacking is ABBAABBA or it can also be written as A'B'A'B'A'B'. This molecular packing scheme is known from many close packed metals. In contrast to the closed pack metals, ice has a very open structure.

At temperatures of terrestrial interest, the distance between two oxygen atoms is 0.276 nm and 0.0985 nm between oxygen and hydrogen. The oxygen and two hydrogen atoms are joined by strong covalent bonds, whereas the water molecules are joined by weak hydrogen bonds. This leads to the low melting temperature of ice. [27]

$P6_3/mmc$ is the lattice description of the oxygen atoms in ice I_h. The primitive lattice is described by the letter P and 6_3 describes the principal axis of symmetry. The principal axis of symmetry is an axis that passes through rings of atoms. The meaning of the letters mmc stands for three symmetry planes in the crystal structure. There is one plane normal to the principal axis of symmetry which mirrors atomic positions, one glide plane and one mirror plane, of which the last two planes are both parallel to the c-axis. [27]

The lattice parameters for ice were measured through diffraction at -20°C with a=0.4510 nm and c=0.7357 nm. The ideal value for hard spheres is c/a=1.633 which is close to the value for ice I_h c/a=1.628, even though the crystal structure of ice I_h is not closely packed [25]. This is due to the size differences of the atoms compared to the atoms distances. The diameter of an oxygen atom is 0.12 nm compared to the distance between two oxygen atoms which is 0.276 nm. Therefor the atomic packing factor is only 0.34, whereas the packing factor for closely packed hexagonal lattices is 0.74. That is the reason ice is less dense than water.

The density of ice can be derived from the lattice parameters and is $\rho = 916.4 \frac{\mathrm{kg}}{\mathrm{m}^3}$ at the freezing point. The low packing factor of ice I_h also explains the decrease of the melting point with increasing pressure. Because there is only one main symmetry plane of thermal conductivity, elastic stiffness and atomic diffusivity are isotropic perpendicular to the c-axis.

3.2 Defects in the ice lattice

Defects in the ice lattice are of great importance for the mechanical properties of ice I_h. In a perfect hexagonal ice lattice, it would be extremely difficult to apply deformation due to the perfect ordering of all bonds [23]. Defects lead to internal shear strain and bending of the atomic bonds. Afterwards, the bending until failure is less than for a perfect bond [27].

Defects can appear on the mesoscale, for example inclusions, cracks, or cavities and they can appear on the microscale. Defects on the microscale can be divided in three groups: point defects, line defects, and plane defects. [28]

This section will deal with the different defects occurring on the microscale in ice I_h.

3.2.1 Point defects

There are five different point defects for ice: interstitials, vacancies, ionic solutes and Bjerrum defects. The first three can occur in all crystal materials, ionic, and Bjerrum defects are unique for ice and often referred to as protonic defects. Each point defect can occur by itself or in combination with other defects. All defects are important for the elastic and creep behavior. [27], [29]

3.2.1.1 *Solutes*

As mentioned before, nearly no foreign atoms are incorporated into the ice lattice. The foreign atoms are rejected during the freezing process. To be able to dissolve a solid solution in the ice lattice three requirements have to be fulfilled. The foreign atoms need to have the right size, a similar type of chemical bonding, and a charge to stay electrostatically neutral. Only a few impurities are fulfilling these prerequisites. For example, ammonium fluoride can be incorporated into the ice lattice of up to 10 weight percent, but it is not present in significant quantities in sea water and therefore of little relevance for sea ice.

An exception for impurities is the inclusion of fluid brine into the solid ice matrix, appearing as brine pockets or brine channels. Important to notice is, that the inclusion of brine does not happen in the ice lattice on the microscale but on a larger scale. [27], [30]

3.2.1.2 *Vacancies*

A vacancy is an empty place in the ice lattice when an H_2O molecule is missing and the defect is in thermodynamic equilibrium with the remaining lattice. A vacancy can occur during crystal growth or if an H_2O molecule at a free surface or interface leaves an empty place in the lattice. This empty space can then move to the center of the crystal.

$$C_{\mathrm{v}} = \exp\left(\frac{S_v}{k_B}\right) \exp\left(\frac{-E_v^f}{k_B T}\right) \qquad 2$$

C_v is the equilibrium vacancy concentration given by the Boltzmann relationship. S_v is the extra entropy associated with each vacancy, k_B Boltzmann's constant, E_v^f the energy needed to place a molecule from the interior of a crystal to its surface, and T the absolute temperature. The implied equilibrium vacancy concentration is $C_v = 10^{-10}$, which is low compared to metals ($C_v = 10^{-3}$ to $C_v = 10^{-4}$), but still high enough to account for prismatic dislocation loops. [27], [29], [30]

3.2.1.3 *Interstitials*

If a molecule is situated within the open space of the ice lattice it is called interstitial, it is also in thermodynamic equilibrium with the ice lattice. Interstitials are formed at free surfaces and interfaces, but they are independent from vacancies. The equation for the interstitial concentration C_i is given by Equation 3.

$$C_i = \exp\left(\frac{S_{int}}{k_B}\right)\exp\left(\frac{-E_i^f}{k_B T}\right) \qquad 3$$

Like the equilibrium vacancy concentration, S_{int} is the extra entropy associated with each interstitial and E_i^f the energy to form an interstitial. Due to the open structure of ice the interstitial concentration for ice is relatively high $C_i = 10^{-6}$ compared to metals. [27], [31]

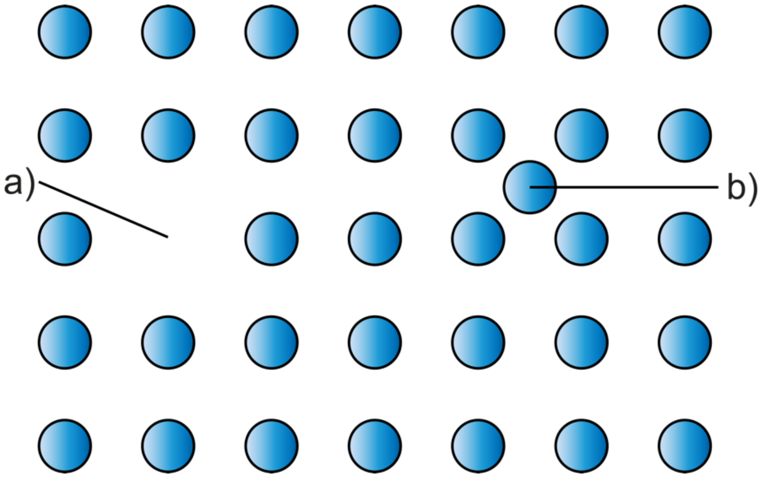

Figure 5 *Difference between a) a vacancy and b) an interstitial. According to* [31].

3.2.1.4 *Protonic defects*

Protonic defects (ionic and Bjerrum defect) result when the Bernal-Fowler rules are violated. The Bernal-Fowler rules say [24]:

1. Two hydrogen atoms are near each oxygen.
2. Only one hydrogen atom can be on or near the line connecting two neighboring oxygen atoms.

Contravening the first Bernal-Fowler rule results in an ionic defect. This means that an oxygen atom is surrounded by three hydrogen atoms, resulting in a positive ion $(H_3O)^+$. On the other hand, if only one hydrogen atom is around one oxygen atom, it leads to the negative ion $(OH)^-$. The chemical reaction is like that in fluid H_2O except that the ions do not migrate as complete units. The process is displayed in Figure 6 b).

When the second Bernal-Fowler rule is contravened, two protons occur on a bond or no protons occur on a bond, resulting in a D-defect (D means doppelbesetzt) or L-defect (L means Leere) (Figure 6 a)).

Without protonic defects, a long-range electrical conduction would not be possible. An ionic defect allows ions to move along bonds, a Bjerrum defect allows ions to move around an oxygen atom. [27], [30]

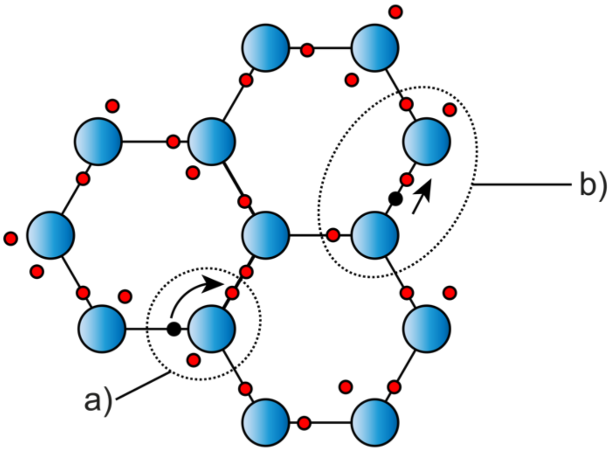

***Figure 6** Protonic defects. a) A proton changes its old position (black) to a new position (red) resulting in a d-defect and l-defect. b) An oxygen atom is surrounded by three hydrogen atoms resulting in $(H_3O)^+$ and $(OH)^-$.* [27]

3.2.2 Line defects

Line defects or dislocations are important for the plasticity of ice. They allow ice to slip under a stress which is several orders of magnitude lower than the calculated shear strength. Dislocations, therefore, lead to a lower deformation energy, compared to a dislocation free crystal. The three main types of dislocations are edge dislocation, screw dislocation and mixed dislocation.

A line defect is described by its Burgers vector **b** and sense vector **s**. The sense vector **s** is a parallel unit vector to the dislocation line **l**. To define the Burgers vector, an atom-to-atom circuit has be drawn in a plane perpendicular to the dislocation, compare Figure 7. If the same circuit would be drawn in a dislocation free crystal, the starting and end point would not be the same. The difference between the starting and end point is the Burgers vector **b**. [32]

Dislocations can slide through the crystal and are therefore fundamental for the plasticity of the crystals. The shear strength of the crystal gets reduced by dislocations, because dislocations bend the atomic bonds and induce shear strain into the crystal. Bending the bonds further till the point of failure than requires a smaller shear stress as for a perfect crystal. Dislocations sliding through a crystals lead to breaking and new formation of bonds, causing the crystal to undergo slip. While the dislocation is wandering through the crystal the Burgers vector stays the same. If a dislocation emerges at the surface it creates a slip line. The number of dislocations is measured in total length per volume m/m^3 and is termed dislocation density. [27], [29], [32]

3.2.2.1 *Edge dislocation*

Edge dislocations have a Burgers vector perpendicular to the dislocation line (Figure 7 ii)). An edge dislocation can be imagined by cutting into a crystal, sliding the parts of the crystal perpendicular to the cut and rejoining the crystal bindings. Edge and mixed dislocations can only slip along one set of crystallographic planes. Crystallographic planes **n** are defined by the Burgers vector and the sense vector. [29], [32]

$$\boldsymbol{n} = \boldsymbol{b} \times \boldsymbol{s} \qquad 4$$

Edge dislocations can appear as in Figure 7 ii) called glide motion, where the bottom crystals are displaced by $\boldsymbol{b}$ compared to the top of the crystal. Dislocation motion perpendicular to the glide plane are called climb motion. Climb motion appears under compression while absorbing vacancies. [33]

Edge dislocations can only climb up or down from the crystallographic plane at point defects or vacancies. [29]

3.2.2.2 *Screw dislocation*

The Burgers vector of a screw dislocation is parallel to the dislocation line. It can be imagined by cutting into a perfect crystals, sliding the parts of the crystal parallel to the cut and rejoining the crystal bondings. Screw dislocations are common in the basal plane and preffered over edge and partial dislocations [34]. A screw dislocation is displayed in Figure 7 iii). Screw dislocations can cross-slip between crystallographic planes. [29], [32]

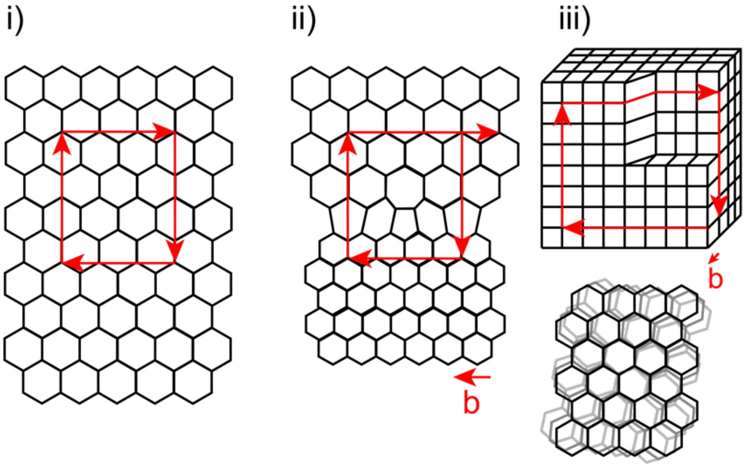

Figure 7 *A dislocation free crystal in i). Burger's vector* ***b*** *for ii) edge dislocation and iii) screw dislocation in a cubic crystal (top) and a hexagonal crystal (bottom). According to* [32], [35], [36].

3.2.3 Partial dislocations

A perfect line dislocation can dissociate into two partial dislocations to reduce its self-energy. A partial dislocation is energetic favorable than a perfect line dislocation. To do so a stacking fault between two partial dislocations is introduced into the lattice. As a result the two new Burger vectors $\boldsymbol{b_1}$, $\boldsymbol{b_2}$ have less energy than the original Burger vector $\boldsymbol{b}$: $\boldsymbol{b}_1^2 + \boldsymbol{b}_2^2 < \boldsymbol{b}^2$. Partial dislocations mostly appear on the basal plane [37]. Three different stacking faults appearing in ice are presented in Figure 8. [33]

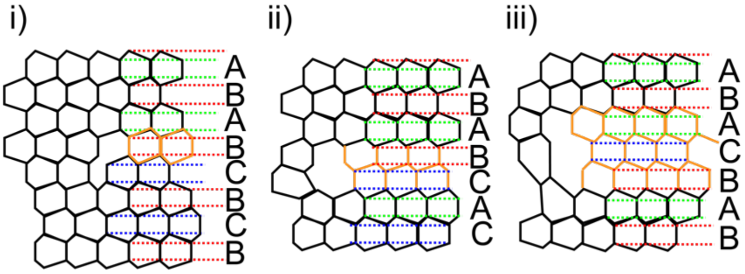

Figure 8 *Three different stacking faults for partial dislocations.*

3.2.4 Plane defects and Grain boundaries

Plane defects are also important for the creep and fracture behavior of ice. Grain boundaries separate regions with the same crystal structure but a different crystal orientation. Most grain boundaries have differences in orientation of more than 10 °, defining a high angle boundary.

3.3 Failure mechanisms

To understand the tests conducted on sea ice, the different failure mechanisms of ice I_h have to be understood. Ice I_h under compression can fail in a ductile, brittle or ductile-to-brittle transition zone and is sensible to confinement. Defects in the ice lattice are the main reason for the failure behavior of ice I_h. Thus, sea ice consists of polycrystals, only polycrystals and no single crystals are considered in the analysis of failure mechanisms.

3.3.1 Ductile behavior

Ductile behavior of ice usually takes place under stress smaller than 1 MPa and strain rates lower than 10^{-3}. Ductile behavior is marked by a smooth stress-strain curve.

If an ice sample is loaded under a constant load, it will start to creep. Total strain ϵ_T for polycrystalline ice can be described by the following equation and separated into three stages of creep:

$$\epsilon_T = \epsilon_e + \epsilon_d + \epsilon_v + \epsilon_c \qquad 5$$

The first stage (primary creep), is divided into two sub-groups. It starts with elastic creep ϵ_e obeying Hook's law. The elastic deformation results from changing the length or shearing of atomic bonds. The elastic creep is followed by time-dependent recoverable strain and delayed elastic strain ϵ_d. The delayed elasticity results from sliding along the grain boundaries. Delayed elasticity is not permanent, but its recovery is not instantaneous. Primary creep can occur up to a strain rate of one percent. Secondary creep or viscous strain marks the second stage of creep. It results from the movement of dislocations and is not recoverable. Viscous creep ϵ_v takes place after the delayed elastic strain approaches zero. Tertiary creep takes place after a sufficiently long time under compressive loading. Micro cracks, which form at the grain boundaries, coalesce and lead to tertiary creep. Tertiary creep is driven by a process called recrystallization. A typical creep curve for ice with its three stages of creep is shown in Figure 9. [26], [38], [39]

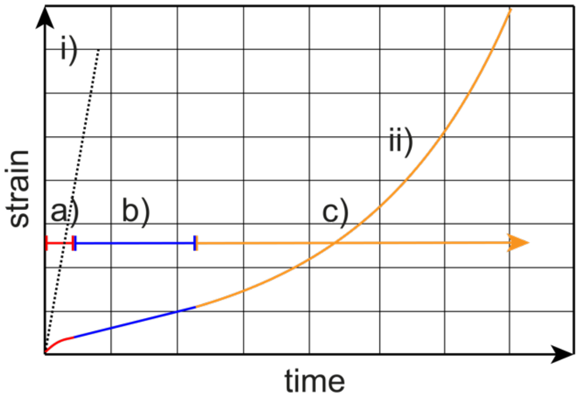

Figure 9 *A typical strain curve for i) brittle behavior and for ii) ductile behavior. Ductile behavior is separated into three phases: a) primary creep; b) secondary creep; c) tertiary creep. According to* [38]

3.3.2 Brittle behavior

Ice I_h, mostly but not always, fails in a brittle manner, if the strain rate is greater than $2 \times 10^{-4} \frac{1}{s}$ [39]. In contrast to ductile behavior, the stress-strain curve for brittle behavior does not show a smooth curve, but rises linearly and suddenly drops off (Figure 9 i)). [40]

The failure process varies for unconfined and confined ice I_h under compression, but both processes start with a parent crack having an angle of 45° to the direction of loading, namely a plane of maximum shear stress. Unconfined and confined ice start to develop secondary cracks, also called wings, at the end of the parent crack. The combination of parent crack and secondary cracks is called wing crack. For unconfined ice the wing cracks keep on growing and start to interact. At terminal failure the secondary cracks lengthen further and split the sample axially. In contrast to that, confined ice under compression develops not only two secondary cracks at the ends of a parent crack, but more secondary cracks between the wings. The secondary cracks result from tensile stress due to the confinement. Opposing face into the ice start gliding, when the shear stress is high enough, leading to tensile stresses within the ice. By formation of secondary cracks, the tensile strength is released. The combination of parent crack and secondary cracks under confinement is called comb crack. The secondary cracks create micro plates between them. If the load is high enough these micro plates break and lead to a collapse of the comb crack. The failure of the comb cracks sheds the load further resulting into a process zone and leading to a shear fault of the sample. [41], [42] As outlined, a wing crack is a prerequisite for brittle failure. Wing cracks originate by sliding along inclined cracks. Sliding along inclined cracks starts if the shear stress τ is higher than the frictional resistance. This leads opposing faces to slide and to develop increasing tensile stress at the crack tips. Wings or secondary cracks nucleate, as described for the confined compression test, if the creep relaxation occurs too slowly. With increasing load, the opposing faces keep on sliding and widen the wings, resulting in a stable crack growth. The process from crack nucleation to a developed wing crack is displayed in Figure 10.

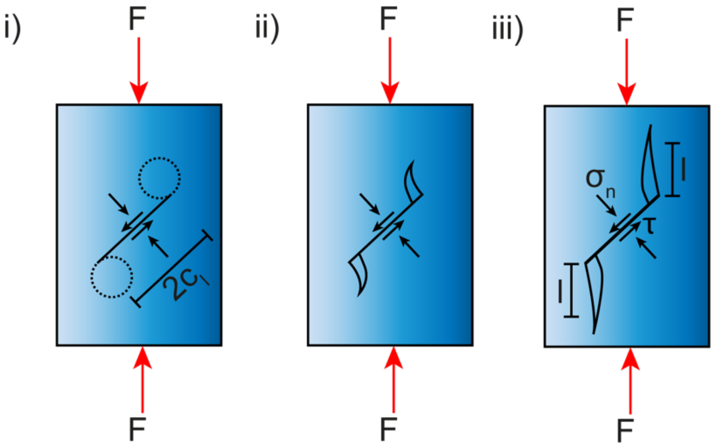

Figure 10 *Schematic drawing of wing crack growth. i) Tensile zones develop at crack tips (dashed circle) with crack length* c_l*; ii) With increasing force F, wing cracks develop at the crack tips; iii) Caused by increasing force the wings elongate to a length l. Shear stress* τ *depends on normal stress* σ_n*. According to* [41].

3.4 Salinity

The salt in sea water is the main difference between fresh water ice and sea water ice. The salt is responsible for many large and small defects in the ice lattice and affects the mechanical behavior of sea ice in many ways.

The salinity of sea water and sea ice is measured in Practical Salinity S_p and is defined on the Practical Salinity Scale from 1981 in PSU [43]. The salinity is measured by the electrical conductivity of the sample. This is defined by the electrical conductivity of the sample ($T = 15\,°C$; $P = 101325$ Pa) divided by the conductivity of a standard potassium chloride solution ($T = 15\,°C$; $P = 101325$ Pa). A ratio of 1 between the two electrical conductivities represents a salinity of 35 PSU, which corresponds approximately to a salt content of 3.5 %. The practical salinity scale is only defined for a salinity between $2\text{ PSU} < S_\mathrm{P} < 42\text{ PSU}$, salinities for $S_\mathrm{P} \leq 2$ PSU can be calculated after Hill et al [44]. Even though salinity is a unitless quantity, it is often referred to in the literature as PSU. Before measuring the salinity by thermal conductivity, it was defined as Absolute Salinity S_A which is the ratio of dissolved material in seawater to the total mass of seawater [45]. The problem of this method is that while evaporating the water many salt crystals evaporate with the water, leading to an inaccurate measurement [46]. [47]

What leads to the different properties of fresh water ice and sea water ice is the behavior of the salt ions. Salt ions are not incorporated into the ice lattice. While the water molecules are freezing, the salt ions either stay in a liquid solution called brine or, if the solution is supersaturated by one component it results in the precipitation of mirabilite precipitates [46]. Standard sea water has a salinity of 35.17 PSU, and the four main components are Cl^-, Na^+, SO_4^{2-}, and Mg^{2+} with shares of 55 %, 31 %, 8 %, and 4 % in weight percent [45]. The remaining 2 % are shared by eleven other ions (see Table 1). For most applications it is suitable to use NaCl, as it represents 85 % of the sea water ions. More precise evaluations also take into account the other ions.

Table 1 *Ion composition of standard sea water in weight-% of total ion weight. According to* [45]

Ions	Ions quantity
	Weight-%
Na^+	30.6596
Mg^{2+}	3.6506
Ca^{2+}	1.1718
K^+	1.1349
Sr^{2+}	0.0226
Cl^-	55.0339
SO_4^{2-}	7.7132
HCO_3^-	0.2981
Br^-	0.1913
CO_3^{2-}	0.0408
$B(OH)_4^-$	0.0226
F^-	0.0037
OH^-	0.0004
$B(OH)_3$	0.0553
CO_2	0.0012

The phase diagram for sea ice Assur [48] shows the amount of brine, solid salts and ice at a specific temperature for sea water with a salinity of 34.325 PSU. This value was investigated before 1960 and therefore differs from the above-mentioned standard sea water salinity of 35.17 PSU. The diagram shows, that, as expected, the ice fraction increases with decreasing temperature. At a temperature of -10 °C the phase diagram displays 77 % solid ice and 23 % brine with a salinity of 141 PSU. $NaCl.2H_2O$ starts to precipitate at -22.9 °C, at -40 °C nearly all sodium chloride is precipitated. At -40 °C the ice concentration has increased to 93 %, 6 % salt crystals and 1 % Brine. Meaning that at all sea ice temperatures typically encountered, a non-neglectable amount of brine is present, which affects the mechanical properties, is present [46].

3.4.1 Porosity Determination

The porosity of sea ice, consisting of gas and brine volume, influences its mechanical properties and is therefore of high interest for this study. The components brine, solid salts, and ice are assumed to be in a thermal equilibrium where the brine is always at the freezing point. The air existing in pockets originates from the freezing process and is independent of the other components [49].The exact implications of gas and brine volume will be outlined in a later section, in this section the focus is kept on the derivation of the equations. The equations used today were derived by Cox and Weeks in 1983. The equations are valid for temperatures in the range of $-2\,°\mathrm{C} \geq T \geq -30\,°\mathrm{C}$ [50]. These equations were extended for higher temperatures by Leppäranta and Manninen for temperatures in the range of $-2\,°\mathrm{C} \leq T \leq 0\,°\mathrm{C}$ [51].

In the equations below, the following abbreviations will be used: m, V and ρ are the bulk mass, volume, and density of a sample, respectively. The components brine, air, pure ice, salt and solid salts are marked by the superscripts b, a, i, s and ss. The symbols m_{x}, V_{x}, S_{x}, and ρ_{x} indicate the mass, volume, salinity and density of the component x.

The pure ice salinity S_i and the brine salinity S_b are defined as follows:

$$S_{\mathrm{i}} = \frac{m_{\mathrm{s}}}{m} = \frac{m_{\mathrm{s}}^{\mathrm{b}} + m_{\mathrm{s}}^{\mathrm{ss}}}{m_{\mathrm{b}} + m_{\mathrm{ss}} + m_{\mathrm{i}}} \qquad 6$$

$$S_b = \frac{m_{\mathrm{s}}^{\mathrm{b}}}{m_{\mathrm{b}}} \qquad 7$$

The mass of salt in the brine is denoted by m_s^b and the mass of solid salts is denoted by m_s^{ss}.

No salt is incorporated into the ice lattice. Therefore, the mass of salt in the whole sample is equal to the sum of the salt mass in the brine and the mass of the solid salts.

$$m \cdot S_\mathrm{i} = m_\mathrm{s}^\mathrm{b} + m_\mathrm{s}^\mathrm{ss} \tag{8}$$

$$m_\mathrm{s}^\mathrm{b} = m \cdot S_\mathrm{i} - m_\mathrm{s}^\mathrm{ss} \tag{9}$$

A factor k_r is introduced, which is the ratio of the mass of the solid salts and the mass of salts in the brine

$$m_\mathrm{s}^\mathrm{b} = m \cdot S_\mathrm{i} - k_\mathrm{r} m_\mathrm{s}^\mathrm{b}. \tag{10}$$

The mass of the salt in the brine can also be described as

$$m_\mathrm{s}^\mathrm{b} = \rho_\mathrm{b} V_\mathrm{b} S_\mathrm{b}. \tag{11}$$

A formula to describe the brine density was developed by Cox and Weeks [52]

$$\rho_\mathrm{b} = 1 + 0.0008 S_\mathrm{b}. \tag{12}$$

It is well known that the mass m_x of a component x depends on the density ρ_x and the volume V_x

$$m_x = \rho_x V_x. \tag{13}$$

If Equation 10 and 11 are combined, an expression for the relative brine volume $\frac{V_\mathrm{b}}{V}$ is obtained.

$$\frac{V_\mathrm{b}}{V} = \frac{\rho S_\mathrm{i}}{\rho_\mathrm{b} S_\mathrm{b}(1 + k_\mathrm{r})} \tag{14}$$

The expression in the denominator is described as $F_1(t)$, thus it depends on the temperature t. A least square fit was calculated by Cox and Weeks [50], that $F_1(t)$ solely depends on the temperature t

$$F_1(t) = \rho_\mathrm{b} S_\mathrm{b}(1 + k_\mathrm{r}) \approx \alpha_1 + \alpha_2 T + \alpha_3 T^2 + \alpha_4 T^3. \tag{15}$$

Values for the coefficients α_0, α_1, α_2 and α_3 were calculated by Cox and Weeks [50] as well as by Leppäranta and Manninen [51]. The values are presented in Table 2.

***Table 2** Factors for Equation 15 according to Leppäranta and Manninen (1988)* [51] *as well as Cox and Weeks (1983)* [50].

	T	α_1	α_2	α_3	α_4
	°C	-	-	-	-
Leppäranta and Manninen (1988)	$0°C \geq t > -2°C$	4.12E-02	-1.84E-01	5.84E-01	2.15E-01
Cox and Weeks (1983)	$-2°C \geq t \geq -22.9°C$	-4.73E+00	-2.25E+01	-6.40E-01	-1.07E-02
Cox and Weeks (1983)	$-22.9°C > t \geq -30°C$	9.90E+03	1.31E+03	5.52E+01	7,16E-01

The derivation of the relative solid salt volume starts with the assumption, that the solid salt mass m_{ss} is proportional to the brine mass m_b and depends on temperature T. Therefore, the factor C is introduced

$$m_\mathrm{ss} = C m_\mathrm{b} \tag{16}$$

$$V_\mathrm{ss} \cdot \rho_\mathrm{ss} = C \cdot V_\mathrm{b} \cdot \rho_\mathrm{b}. \tag{17}$$

Noting that the solid salt density is $\rho_\mathrm{ss} = 1500 \frac{\mathrm{kg}}{\mathrm{m}^3}$, the relative solid salt volume can be written as

$$\frac{V_\mathrm{ss}}{V} = \frac{\rho_\mathrm{b}}{\rho_\mathrm{ss}} \cdot C \cdot \frac{V_\mathrm{b}}{V}. \tag{18}$$

As the mass of the air is neglectable small, the mass of the pure ice m_i is defined as

$$m_{\mathrm{i}} = m - m_{\mathrm{b}} - m_{\mathrm{ss}}. \tag{19}$$

Inserting Equation 13 and 17 into Equation 19 leads to the expression for the relative pure ice volume in the sample.

$$\frac{V_{\mathrm{i}}}{V} = \frac{\rho}{\rho_{\mathrm{i}}} - (1 + C)\frac{\rho_{\mathrm{b}} V_{\mathrm{b}}}{\rho_{\mathrm{i}} V} \tag{20}$$

The relative air volume can be calculated by subtracting the results from Equation 14, 18 and 20

$$\frac{V_{\mathrm{a}}}{V} = 1 - \frac{V_{\mathrm{b}}}{V} - \frac{V_{\mathrm{i}}}{V} - \frac{V_{\mathrm{ss}}}{V} \tag{21}$$

$$\frac{V_{\mathrm{a}}}{V} = 1 - \frac{\rho}{\rho_{\mathrm{i}}} + \frac{V_{\mathrm{b}}}{V}\left((1 + C)\frac{\rho_{\mathrm{b}}}{\rho_{\mathrm{i}}} - \frac{\rho_{\mathrm{b}}}{\rho_{\mathrm{ss}}}\, C - 1\right). \tag{22}$$

Introducing a function for the density of pure ice depending on temperature and defining $F_2(t)$ and a least square fit of $F_2(t)$ according to Equation 15.

$$F_2(t) = (1 + C)\frac{\rho_{\mathrm{b}}}{\rho_{\mathrm{i}}} - \frac{\rho_{\mathrm{b}}}{\rho_{\mathrm{ss}}} C - 1 \approx \alpha_{\mathrm{I}} + \alpha_{\mathrm{II}} T + \alpha_{\mathrm{III}} T^2 + \alpha_{\mathrm{IV}} T^3 \tag{23}$$

$$\rho_{\mathrm{i}} = 0.917 - 1.403 \cdot 10^{-4} \cdot T \tag{24}$$

The coefficient for Equation 23 are displayed in Table 3. The relative air volume is calculated to be:

$$\frac{V_\mathrm{a}}{V} = 1 - \frac{\rho}{\rho_\mathrm{i}} + \rho S_\mathrm{i} \frac{F_2(T)}{F_1(T)} \qquad 25$$

Table 3 *Factors for Equation 23 according to Leppäranta and Manninen (1988) [23] as well as Cox and Weeks (1983) [22].*

	T	α_I	α_II	α_III	α_IV
	°C	-	-	-	-
Leppäranta and Manninen (1988)	$0°C \geq t > -2°C$	9.03E-02	-1.61E-02	1.23E-04	1.36E-04
Cox and Weeks (1983)	$-2°C \geq t \geq -22.9°C$	8.90E-02	-1.76E-02	-5.33E-04	-8.80E-06
Cox and Weeks (1983)	$-22.9°C > t \geq -30°C$	8.55E00	1.09E-00	4.52E-02	5.82E-04

Knowing the relative pure ice, brine, air and solid salt volume, the total porosity ν_T can be calculated. The total porosity is defined as the sum of air volume and brine volume. [49]

$$\nu_\mathrm{T} = \frac{V_\mathrm{a}}{V} + \frac{V_\mathrm{b}}{V} \qquad 26$$

3.5 Sea ice

Sea ice covers about 7 % of the earth's surface and is important for the global climate as well as the ecosystem. Therefore, changes in sea ice concentration and thickness are under scientific observation but are not totally covered by climate models. For example, the sea ice concentration in the Antarctic region in 2007 was below 40 % of the long-time average, but different from the prediction, the decline in sea ice concentration did not increase as expected [11]. On the other side, the sea ice concentration in the Antarctic region reached a maximum extent in 2012, 2013, and 2014, which was not captured by the current models [11], [53].

Different kinds of sea ice are present in the Arctic and Antarctic regions. The Arctic region is dominated by thick multi-year ice, whereas relatively thin first-year ice is present in the Antarctic [11]. During the freezing process, different types of sea ice are present, starting with frazil ice followed by pancake ice floes, and ending with a solid pack ice cover. The different types of sea ice have different properties e.g. crystal structures, salinity profiles or mechanical properties. As this study is about sea ice in the Antarctic Marginal Ice Zone, only sea ice types present in the Antarctic will be considered. The different ice types are presented in this section and displayed in Figure 11 according to the pancake ice cycle by Lange et al. for sea water [17]. Nearly the same process, but in more detail, was described in the literature for fresh water river ice [54].

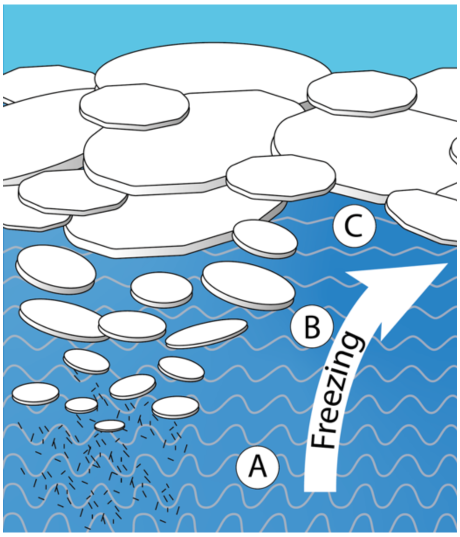

Figure 11 *The pancake ice cycle according to* [17]*. A: Frazil ice formation; B: Formation of pancake ice floes; C: Rafting of pancakes to a closed consolidated sea ice cover.*

If the water is supercooled, meaning that the temperature of the water is below its freezing point, frazil ice will form. The small frazil ice particles are kept in the suspension by the turbulence of the stream or the ocean current. If enough frazil ice crystals are present, they will start to form larger flocs of ice. The frazil flocs will stay in suspension until the buoyant force gets stronger than the water turbulence, which will rise them to the surface. Arising at the water surface, many frazil ice flocs will start to form larger pans of ice, termed pancake ice. The pancakes grow in size, raft together and form larger rafts of ice, until the water is completely covered by ice. [17], [54]

3.5.1 Frazil ice

Frazil ice is the first ice that forms in the annual freezing process of the MIZ in the Antarctic. Its growth requires supercooled water, which means that the water temperature is below its freezing point, turbulence in the water body and, seed crystals. The frazil ice crystals are disc-shaped with a diameter between 0.01 - 16 mm and a thickness ranging from 1 – 100 µm [55]–[57]. If enough frazil ice crystals are present, they start to form larger flocs of ice.

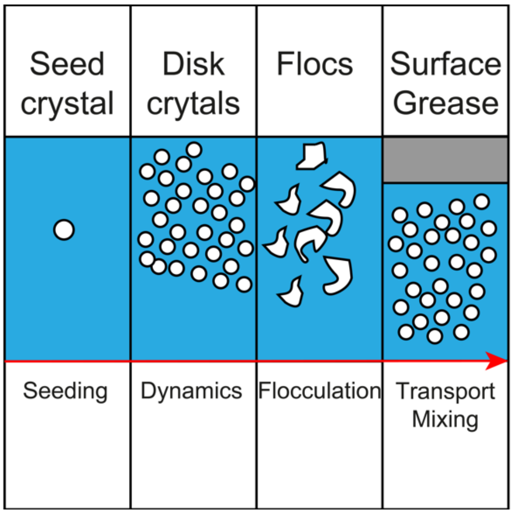

Figure 12 *Frazil ice evolution in natural water bodies according to* [56]. *First a seeding crystal is required, afterwards multiple disk crystals form. The disk crystals develop into agglomerations of disks respectively flocs. Flocs rise to the surface and form a surface grease ice layer consisting of frazil ice, while smaller crystals are still in suspension.*

The scientific term frazil ice was used first in studies of river ice at the St. Lawrence River close to Montreal at the end of the 18th century. The term is most probably a French-Canadian word, which originates from cinders produced from coal. Settlers from France had never seen the slush-like frazil ice back in France and named it according to the familiar cinder material with similar properties and started calling it “frasil”/“frazil”. [58]

3.5.1.1 *Nucleation*

Nucleation is the starting point of crystallization [59]. Nucleation mechanisms can be separated into homogeneous and heterogeneous nucleation. A process is termed homogeneous nucleation, if no nuclei are needed and the nucleation happens spontaneously. On the other hand, crystallization is called heterogeneous if nuclei are needed to start the crystallization [60].

The homogeneous nucleation temperature of pure water is about -38 °C [60], which is much lower than the observed supercooling before frazil ice production of 0.05 - 0.1 °C. For that reason, pure homogeneous nucleation can be excluded from the primary nucleation of frazil ice. Sea water is not pure but consists of many different ions and organic materials, which can serve as heterogeneous nucleation sites. Nevertheless, the inorganic material with the highest known threshold nucleation temperature is silver iodide with -3.5 °C and therefore still lower than the observed supercooling [61]. Phytoplankton, which is available in sea water, could also serve as a heterogenous nucleus but it is only active at temperatures around -4.0 °C [62], bacteria are known that serve as nuclei at about -1 °C [63]. As a result, heterogeneous nucleation by impurities can also be excluded from the nucleation of frazil ice.

The mass exchange occurring at the interface of the water is another possibility for primary nucleation and was researched by Osterkamp [61]. The research target was to find other possible nucleation processes than the ones described before. His research focused on a supercooled freshwater stream, nevertheless, the experiment boundary conditions are transferable to Antarctic sea ice conditions. During the experiment, the stream was supercooled. It had a temperature between -0.012 °C and -0.050 °C. The researchers investigated the mass-exchange process between the water surface and the atmosphere. At air temperatures, lower than -8 °C, ice crystals were observed above the stream while at higher air temperatures no ice crystals were observed [61]. Further experiments also ruled out the possibility that the crystals in the air had a different origin than those from the freshwater stream. Water might be transferred out of the water by ocean waves, evaporation, wind, and bubbles. For example, one breaking bubble produces multiple drops with a size of 1 – 20 µm, which could serve as a germ, if frozen [64].

After the water drops originating from ocean waves, evaporation, wind, or bubbles left the ocean, they need to freeze to serve as a germ for the frazil ice nucleation. A study shows, that for a water droplet with a diameter of 100 µm, it takes 1 s until the steady state condition with the air temperature is reached. For water droplets having a smaller diameter, the equilibrium state will be reached even faster [65]. Therefore, it seems reasonable, that frozen water droplets originating from the ocean and freezing in the atmosphere, cause the primary nucleation of sea water.

The secondary nucleation takes place after the primary nucleation when some ice crystals are present in the ocean. The secondary nucleation is mostly driven by crystal collision due to turbulence, where small ice pieces break free [66]. The impact of turbulence on the secondary nucleation and frazil ice growth rate will be further discussed in Section 3.5.1.3.

In summary, primary nucleation is driven by a mass-exchange process at the interface of the oceans where water droplets originating from the ocean freeze and serve as a germ for homogeneous ice nucleation afterwards. Secondary nucleation occurs due to the collision of frazil crystals where small ice pieces break free.

3.5.1.2 *Supercooling*

Supercooling is, as mentioned before, one important prerequisite for frazil ice growth. If the temperature of a liquid is below its freezing point without freezing, it is called supercooling. Figure 13 shows a typical supercooling graph for fresh water (red) and sea water (blue), the x - axis displays the time t and the y-axis displays the temperature T. T_0 is the freezing temperature of the water. The freezing point of water can be calculated by Equation 27 [67]

$$T_0 = -0.055 \times S. \qquad 27$$

The residual supercooling temperature T_r for freshwater is a constant temperature below the freezing point of water. T_r is the temperature of the water after the primary frazil ice nucleation. The residual supercooling is an important force for the ongoing frazil ice production, it is also called the principal period of supercooling. If the residual supercooling is equal to the freezing point, the frazil ice growth will stop. The minimum temperature of the water is termed T_min. In the beginning, Figure 13 displays a linear temperature decrease caused by a net heat loss of the water until the water temperature reaches the minimum temperature. At the minimum temperature, the water is seeded with a nucleus. Afterwards, the growth and nucleation of frazil ice crystals release energy, leading to an increase in the water temperature up to the residual supercooling temperature. [68]

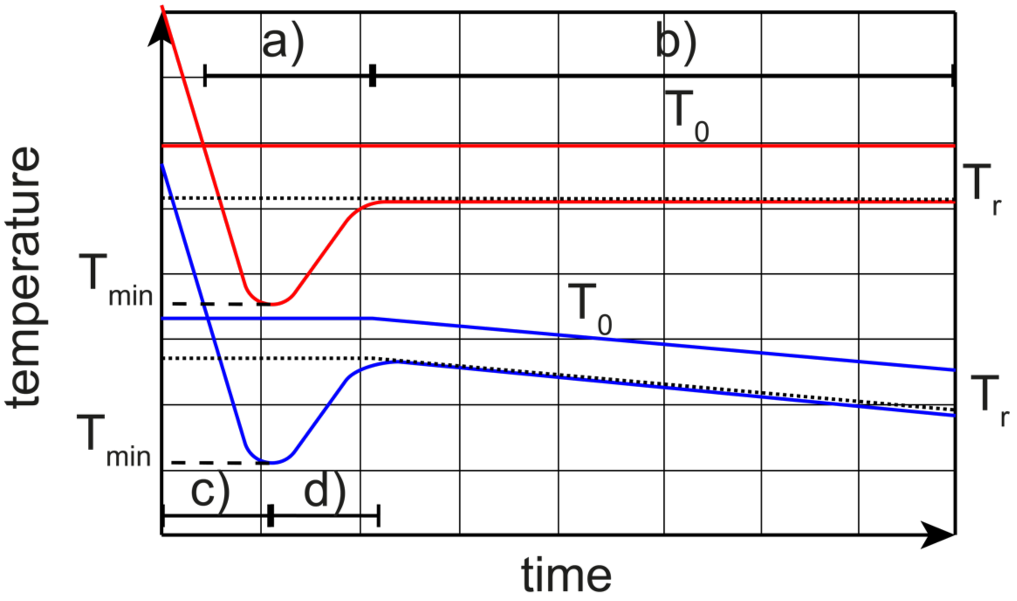

Figure 13 *Supercooling of water for fresh water (red) and sea water (blue). a) supercooling; b) residual supercooling; c) cooling; d) heat release by the crystals. According to* [68], [69].

Supercooling graphs for fresh water and salt water mostly differ in the region of residual supercooling, as displayed in Figure 13. As mentioned before, this region is constant for fresh water ice but decreases slightly linearly for salt water. This temperature decrease is due to the rejection of salt from the freezing ice, lowering the freezing temperature of the water.

In contrast to the salinity, the temperature has a higher impact on the frazil ice production. The temperature development is a good index for the frazil production. As displayed in the schematic Figure 14, the temperature increases with the beginning of the frazil ice production. The temperature increase is caused by heat released from the frazil ice during nucleation and growth.

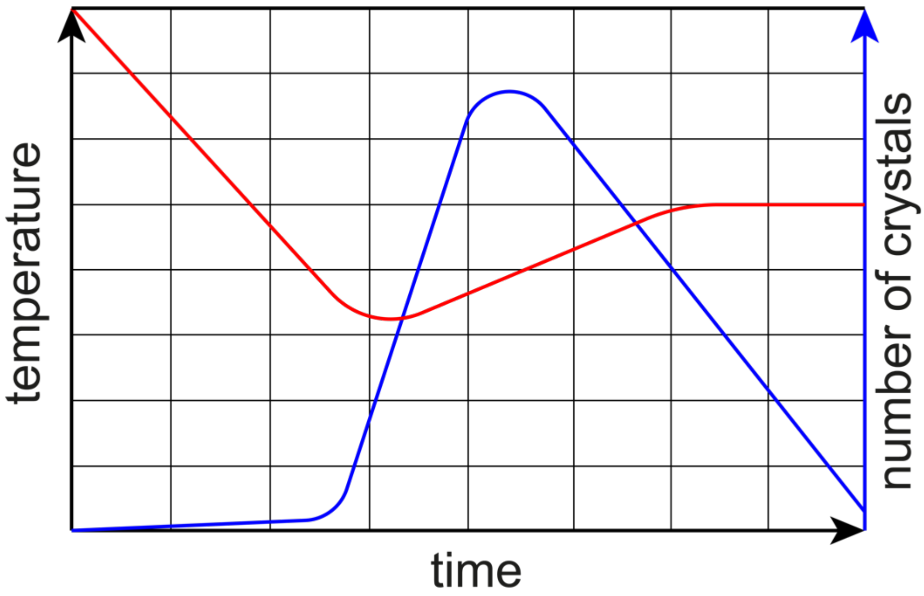

Figure 14 *Schematic drawing of temperature and number of crystals during frazil ice production. According to findings of* [55].

3.5.1.3 *Turbulence*

Turbulence is another important prerequisite for frazil ice production. Without turbulence, a solid ice cover would form as can be seen for lakes. Nevertheless, the literature gives different minimum flow velocities for frazil ice production. The minimum flow velocity obtained in experiments was 9.1 cm/s by Smedsrud [70], 15 cm/s by Hanley [71], 24 cm/s by Hanley [72], and 33 cm/s by Carstens [73]. The spread of the velocities shows uncertainties in the measurements, and the question arises which influence does the turbulence have on the crystal ice growth?

Heat is released when frazil ice crystals nucleate and grow, leading to an increase in the water temperature. Therefore, the temperature is often plotted along with graphs of the frazil ice growth. The temperature is an adequate measure for the frazil ice growth (Section 3.5.1.2).

A stronger intensity in turbulence increases the rate of frazil ice nucleation, which corresponds to a rise in the rate of change of water temperature. This increase in frazil ice growth and nucleation can be explained by an improved heat transfer between the water and frazil ice, as well as by a higher collision rate between the frazil ice platelets. [74]

Experiments conducted by Ye [68] suggest that higher turbulence leads to larger frazil ice particles. The first analysis by Clark [75] generated the idea that the frazil size increases with increasing turbulence up to the point where the size is limited by the weak mechanical properties of the frazil ice crystals. Whereas a second study by Clark [66] draws the conclusion that a higher rate of turbulence limits the maximum size of frazil ice particles, due to more collisions between the particles. The assumption from Clarks [75] first study is repeated without scientific confirmation that the frazil crystals size is limited by the turbulent kinetic energy [66]. An even stronger decrease in frazil crystal size was noted by McFarlane [55] for increasing turbulence. McFarlane also draws attention to the different instruments to induce turbulence in the water. From his point of view, the different mechanisms can lead to different forces on the frazil ice crystals and could affect their size distribution [55].

3.5.1.4 *Morphology*

Frazil ice crystals appear in different sizes and shapes depending on the environmental conditions. Several different shapes and sizes of frazil ice crystals are described in literature. Frazil ice appears as

- “thin circular discs” [61],
- “fine disc-shaped or dendritic crystals called frazil ice” (d_{ia}= 1 - 4mm; h= 1 – 100 µm) [76],
- “initially irregular in shape they develop into disk shape” (d_{ia} = 1 - 2mm; h= 10 - 100 µm) [77],
- “fine spicules, plates or discoids of ice” [78],
- “disc-shaped particles” (d_{ia} = 22 µm – 6 mm) [79],
- “discoidal crystals (d_{ia} =1 – 14 mm)” [74],
- “shapes of disks” (d_{ia} = 1 – 5 mm) [80],

to just name some observations. Most researchers observed a diameter between 1 - 5 mm and a much thinner thickness depending on the preferred growth direction of hexagonal ice.

3.5.1.5 *Sintering*

Once single frazil ice crystals have formed, larger flocs start to form. These flocs form because single crystals start sintering together. Sintering is a process, where particles get bonded without melting them to reduce the surface energy [81]. The shape of the crystals adjusts and sinter to reduce the surface free energy to a minimum. Sintering between two crystals works through a chemical-potential gradient between the point of contact and the surface of the unstressed crystals, leading to mass transport to the contact point. More and more particles sinter and form larger frazil ice flocs. Sintering therefore leads to rapid ice growth and larger particles inside the water. [57]

3.5.1.6 *Quantity/ Concentration*

Frazil ice concentrations have been measured in the laboratory and during field testing campaigns. All documented frazil ice concentrations are well below 1 % and are shown in Table 4. Different techniques were used to determine the frazil concentration: image analyses, sieving techniques, sonar, and conductivity measurements.

Sieving techniques are the only direct measurement attempts performed in the literature. For this technique, a net is placed in front of a water intake and collects all frazil particles drawn to the water intake opening. Subsequently, the weight of the frazil ice crystals is measured [82]. Instead of collecting frazil ice crystals in front of a water intake, it is also possible to pull a mesh through a defined water volume and measure the weight of the ice crystals inside the mesh afterwards. The measured weight is then divided through the water volume resulting in a frazil ice concentration [83]. Additionally, the direct sieving technique allows the determination of particle size and shape precisely with the help of a microscope after the sampling process. Direct measurement techniques are used to calibrate the indirect measurement techniques.

Image analyses are mostly used in the laboratory while growing artificial frazil ice, but recent studies have also operated them in the field. To capture images of the frazil ice growth a camera is either placed inside a frazil tank or outside a tank in front of a glass window. For better visibility of the crystals, polarization sheets can be used in front of the camera. Linear polarization sheets are placed vertically (or horizontally) in front of the light source and perpendicular to the direction in front of the camera. This technique increases the contrast of the pictures. Afterwards, image analysis is mostly done with automatic software which counts the crystals and measures the crystal size and shape.

For acoustic measurements, two different attempts are described in literature to estimate particle size and concentration. The first technique compares the acoustic signal to values measured in the laboratory and the second technique uses scattering models developed for different kinds of particles to estimate the frazil ice particle number.

For the first acoustic technique, frazil ice is generated in a tank and then measured with a direct technique as explained before. In the meantime, a sonar with different frequencies is used inside the frazil tank. Afterwards, the backscattered intensity for the different frequencies is correlated with the direct method resulting in a regression analysis that allows calculating frazil ice concentrations for backscatter data from other test runs.

For the second acoustic technique, scattering models developed for different crystal shapes are used allowing to estimate the crystal sizes and concentrations from the backscattered data. The models depend on assumptions about the density and elasticity of the crystals and the water, particle shape and size as well as acoustic frequencies. As can be seen, this technique requires a lot of assumptions for the material property, crystals shape, and sonar accuracy and is, therefore, more vulnerable compared to the first method. [84]

Another way to determine the frazil ice concentration is via an electrical conductivity measurement. Frazil crystals are electrically non-conductive in contrast to water. Therefore, a sample of water with frazil ice inside can be compared to a sample without frazil ice showing a remarkable difference. The difference of the two measurements and the assumptions that the frazil ice is equally distributed within the sample and that the crystals are isotropic shaped, enables to determine the frazil ice concentration via electrical conductivity. [85]

Table 4 *Frazil ice concentrations measured by different researchers in the laboratory and field with different techniques.*

Study	Field/ Laboratory	Volume-%	Particles	Mass-%	Measurement technique
-	-	%	1/m^3	%	-
Daly and Colbeck [86]	Laboratory		10^5-10^6		Image analyses
Ettema et al. [82]	Laboratory	0.066-0.609	10^5-10^6		Sieving
Ye et al. [68]	Laboratory	0.10-0.17			Image analyses
Ghobrial et al. [83]	Laboratory			0.012-0.135	Sonar/ sieving
Osterkamp and Gosink [87]	Field		10^4-10^7		Image analyses
Tsang [85]	Laboratory	0-0.6			Conductivity
Tsang [71]	Laboratory	0-0.25			Conductivity
Marko and Jasek [88]	Field		10^5-10^7		Sonar
Richard et al. [89]	Field		10^5-10^7		Sonar
Schneck et al. [90]	Laboratory		10^6		Image analyses
McFarlane et al. [79]	Field	0.0001-0.0018	10^4-10^6		Image analyses
McFarlane et al. [55]	Laboratory		10^5-10^6		Image analyses

3.5.2 Viscosity

The property of a fluid to resist to a given shear stress is defined as viscosity. A high viscosity describes a strong flow resistance and a low viscosity a weak resistance. Viscosity can be measured either as dynamic viscosity η in Pas or kinematic viscosity ν in $\frac{\mathrm{m}^2}{\mathrm{s}}$.[91]

The viscosity of frazil ice is especially interesting for the growth of large, congealed sea ice floes and consolidated sea ice. If the frazil ice shows a high viscosity, the ocean is damped stronger than if the frazil ice would show a low viscosity. In the end, stronger damping will result in a faster freeze-up of the ocean. Therefore, the viscosity of frazil ice is crucial for sea ice growth.

Viscosity has been determined for three different stages of sea ice growth, displayed in Figure 11: pure frazil ice, frazil and pancake ice mixture and sea ice floes [92]–[96]. The experiments were either conducted in the field or in the laboratory. To calculate the sea ice viscosity the amplitude attenuation of surface waves was used while traveling through the sea ice cover. For these calculations assumptions about the behavior of the sea ice cover are made e.g. the viscoelastic sea ice model [93] or the viscous two-layer model [97]. The assumptions then affect the calculated viscosity. Examples for the obtained values are as followed.

Newyear and Martin obtained a viscosity between 15 ± 0.3 to 30 ± 0.6 Pas [92], Wang and Shen calculated a viscosity between 20 ± 0.4 to 60 ± 1.2 Pas [98] and Zhao and Shen calculated the viscosity to be 14 ± 0.3 Pas [94]. Another attempt to calculate the viscosity is through the use of SAR images 50 ± 1 Pas [95].

Most of the data were obtained by indirect measurement techniques in the laboratory. The results depend on sea ice models, which were assumed beforehand. Besides that, only a few measurements were performed in the Antarctic Marginal Ice Zone, where the sea ice properties differ fundamentally from those in the north. This may also lead to different values for viscosity. Concluding, the viscosity of sea ice is an essential parameter for numerical calculations, but there is a lack of knowledge of data from the MIZ with direct measurement techniques.

3.6 Pancake and consolidated sea ice

Once the frazil ice congealed to larger flocs, it develops into pancake ice resulting in a pancake and frazil ice mixture on the ocean surface. The ocean is damped by the frazil and pancake ice layer, leading to the formation of large ice floes with diameters greater than ten kilometers. In contrast to the arctic region, where sea ice covers with a thickness over several meters can grow, sea ice thickness in the Antarctic is limited to approximately one meter by the high ocean heat flux [99]. Thicker sea ice can only originate from ridging and rafting of sea ice floes [9].

Most of the information about sea ice thickness was collected during past cruises. Spaceborne methods are difficult to use, as the snow thickness is a crucial parameter to determine sea ice thickness via satellite. Snow thickness is highly variable in time and place, therefore snow thickness measurements need to be improved for better spaceborne sea ice thickness measurements. [99]

The sea ice floe size and thickness are determined by environmental conditions, such as the heat flow from the ocean to the atmosphere and to the ice [100], wind forcing [101], surface turbulence [101], or waves [6]. Even though many mechanisms influencing sea ice growth and decay are known, it is unclear how they interact, and create feedback mechanisms and the importance of each mechanism for sea ice development on its own [5].

During freezing, brine is trapped inside the ice. Brine channels and pockets are a habitat for microorganisms and influence the sea ice density and morphology. Besides brine content, the morphology comprises the grain shape and orientation as well as air voids on different scales. To better understand the depending properties, knowledge of the microstructure is crucial.

The crystal structure of ice is explained in Section 3.1. A “grain” is either a single crystal or a group of crystals with the same alignment. If the term is not specified, a single crystal can be referred to as a grain [102]. Nearly the same factors determining the sea ice floe size (weather conditions, air temperature, snow cover, and deformation) also affect the sea ice grain structure [103]. The texture of sea ice can give information about the freezing conditions and helps when analyzing mechanical tests. To analyze the grain structure, texture and brine content either destructive methods like thin section analysis/birefringence technique or non-destructive methods like magnetic resonance [104], [105], nuclear magnetic resonance [106], [107], microscopy [108], or X-ray tomography [109], [110] can be used. Non-destructive methods have the benefit that in general less sample processing is required, the brine loss can be minimized and for some techniques, a 3-D image of the pore structure can be captured [111].

Figure 15 *Different textures of sea ice: i) granular ice, ii) transitional ice, iii) columnar ice.* [112]

Sea ice texture can be separated into two main classes, granular and columnar dividing into five different classes in total [113]. Granular ice consists of randomly orientated grains, while columnar ice consists of several centimeter-large, vertically elongated grains [46]. The five identified classes [113] are:

1. Polygonal and orbicular granular, see Figure 15 i),
2. Transitional or intermediate granular/columnar, see Figure 15 ii),
3. Mixed granular/columnar,
4. Columnar Figure 15 iii), and
5. Platelet textures.

Optical measurement methods alone do not allow to distinguishing between orbicular granular ice originating from frazil ice or originating from flooded snow. This can only be achieved by looking at stable oxygen data from the ice, requiring another analysis.

3.6.1 Mechanical testing of Sea Ice

Mechanical properties of sea ice, like flexural, shear, tensile, and compressive strengths; are important for the safety of offshore structures and are of great importance for ice-ice interactions [39]. A lot of mechanical tests have been performed on fresh water ice, Arctic ice, and only some tests on Antarctic sea ice. Due to the brine content in sea ice, the mechanical properties of fresh water and sea ice are significantly different. Sea ice is less uniform in its mechanical properties compared to fresh water ice. Testing temperature and strain rate are the main parameters affecting the strength, while sea ice properties also depend on brine content and growth conditions. Arctic and Antarctic ice both originate from sea water, nevertheless the growth conditions, brine content, and age differ fundamentally, as mentioned before [11]. These differences between the three kinds of ice lead to the fact that separate tests must be performed for each kind of ice.

Fracture toughness [20], [114]–[116], shear [117], tensile [117], and compressive strength [7], [20] were tested on Antarctic sea ice. Most of the tests were performed in the McMurdo Sound [114]–[117], not being representative of Antarctic sea ice, as the area is covered over the whole year with ice and is located close to the coast. Besides tests in the McMurdo Sound, tests were conducted at the Lutzow-Holm Bay [20] and Weddell Sea [7].

Fracture toughness measurements are independent of the sample geometry, making it easy to compare between different publications. Fracture toughness tests of Antarctic sea ice can be separated into experiments conducted in the field [114], [116] and in the laboratory [20], [115]. Nevertheless, results for laboratory and in-situ tests differ, as the composition of ice changes during transport and storage [115] and sample size affects the results [114]. Other parameters affecting the results are ice temperature, crack length, and testing method (stress or strain controlled) [114], [116]. It was found that the fracture toughness increases with increasing grain size [20].

Tests on the tensile and shear strengths were performed in multi-year ice close to the coast of Cape Armitage [117]. The tests were performed at different temperatures, the tensile and shear strengths decrease with increasing temperature. At a testing temperature of -10 °C a shear strength of 1.2 N/mm^2 was noted. The shear strength decreases to 0.5 N/mm^2 at -2 °C. The ring tensile strength was used at -6 °C and -2°C to 1.4 N/mm^2 and 1.0 N/mm^2, respectively. It was found that shear and tensile strength are a function of ice salinity and temperature.

Only two studies report on the compressive strength of Antarctic sea ice. One test was performed in the field [7] and one test after a long time of storage [20] of the ice. The tests show a strength decrease with decreasing density respectively with increasing porosity. The maximum strength of the different testing campaigns are 6.09 MPa [7] and 8.1 MPa [20].

3.6.2 Uniaxial compressive strength of Sea Ice

Compressive strength is a commonly used destructive testing method for building materials [118], ice [39], and other materials. For compressive strength, a prismoidal or cylindrical sample is loaded until failure. The stress at failure is known as compressive strength σ_c. If the load is only applied in one direction, the test is considered as an uniaxial test. If the sample is also loaded from the two other sides, it is a triaxial compression test. For this study it was tried to test samples under uniaxial compression.

According to Schulson [27], samples need to fulfill the conditions shown in Figure 16. The sample ends need to be parallel to prevent an uneven load distribution within the sample. The sample should be sufficiently large to be representative of the ice section and include several grains. A diameter-to-length ratio of 1:2.5 is suggested so that a uniform stress distribution within the sample is ensured. A comparison between a sample with a ratio of 1:2.5 and 1:1 is displayed in Figure 17. At last, a cylindrical shape is preferred over a rectangular one to minimize internal stresses. Besides requirements for the sample, also requirements for the testing device must be met. The testing device needs a high stiffness, to obtain stable failure of the sample. The loading platens of the device should be designed so that they do not induce constraints into the sample. [27]

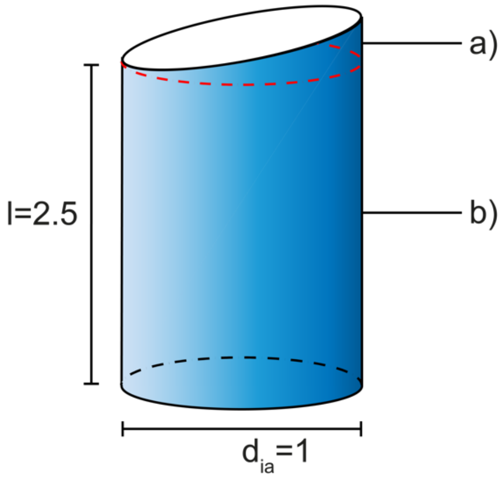

***Figure 16** Factors that must be paid special attention to for compressive strength specimens according to Schulson* [27]. *a) Sample ends should be parallel; b) The size should be sufficient large to represent the ice; A diameter-to-length ratio of 1:2.5 is suggested.*

The strain rate is a crucial parameter for compressive strength testing, as it decides whether the sample fails in a ductile or brittle manner. The highest compressive strength is measured in the ductile-to-brittle transition zone, at a strain rate between $10^{-4}\,\frac{1}{\mathrm{s}}$ and $10^{-3}\,\frac{1}{\mathrm{s}}$ for polycrystalline ice [27]. For Arctic summer sea ice, the transition zone was found to range from $10^{-4}\,\frac{1}{\mathrm{s}}$ to $4 \times 10^{-3}\,\frac{1}{\mathrm{s}}$ for columnar ice and from $3 \times 10^{-5}\,\frac{1}{\mathrm{s}}$ to $8\ \times 10^{-4}\,\frac{1}{\mathrm{s}}$ for granular ice [119]. A ductile stress-strain curve is recognizable by its smooth shape, while a brittle stress-strain curve increases linearly and drops off suddenly [27].

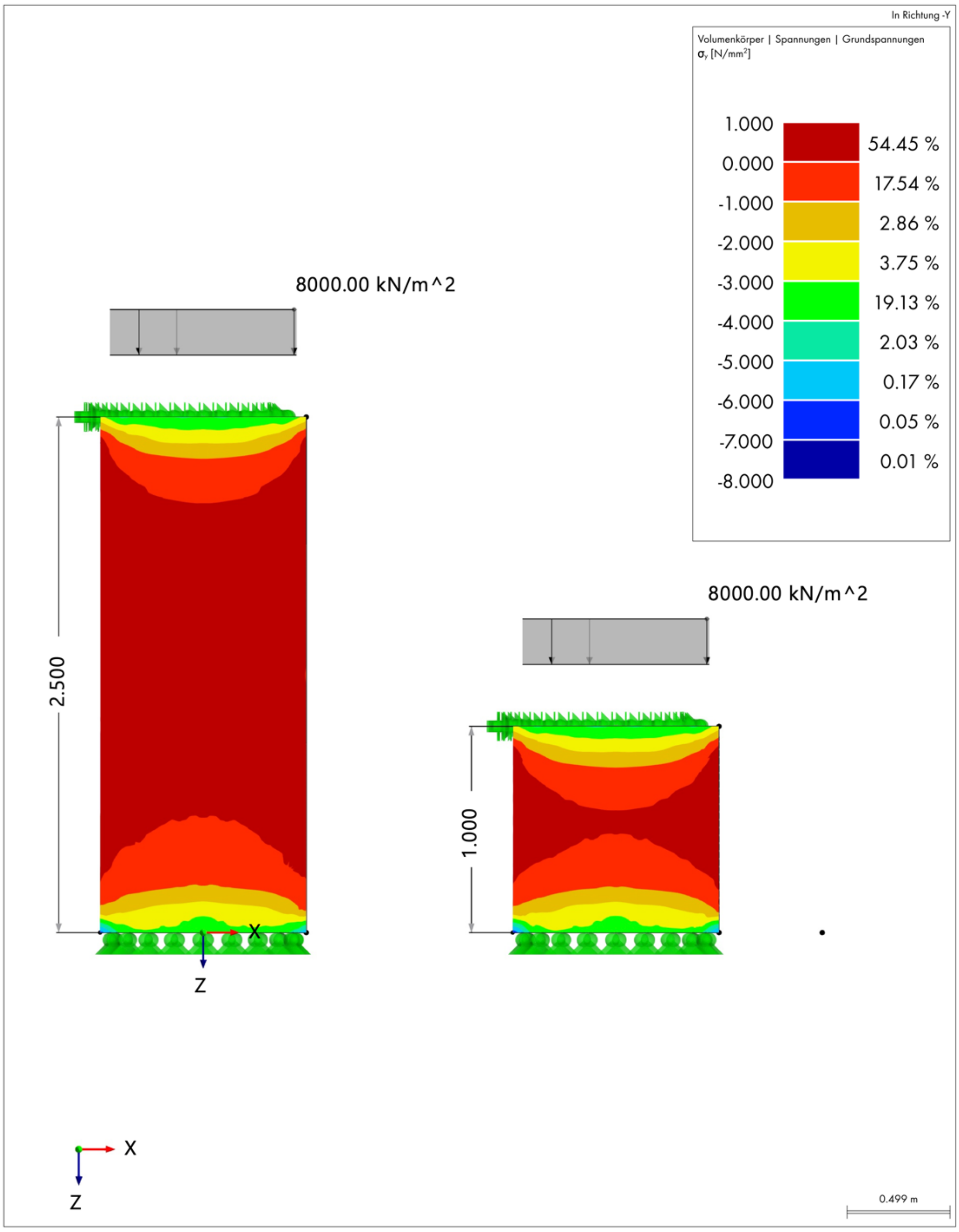

Figure 17 *Example of how the sample length affects the stress inside a sample of 1:2.5 m and 1:1 m. The used software is RFEM 6.02 boundary conditions for the 3D calculation (linear-elastic material law) are as follows: At the bottom the cylinders is fixed in x-, y- and z-direction, at the top they are fixed in x- and y-direction. An area load is applied to the top of the boundary in z-direction. The target length for the pentahedron-shaped finite elements is 0.1 m. Further information about the elements can be found in* [120].

Only two studies measured the compressive strength of Antarctic sea ice, as described in Section 3.6.1. Therefore, the following results also include findings from the Arctic region. Besides strain rate, the strength is influenced by testing temperature, texture, brine content, and porosity. Studies show an increasing strength with decreasing testing temperature, which might be due to shrinking brine inclusion inside the sample [121], [122]. Columnar ice shows a higher strength while failing in the brittle, ductile, or brittle-to-ductile transition zone compared to granular ice [119]. It is also important to note that columnar ice tested along the columns, along the plane normal to the basal plane, shows a higher strength than if tested across the columns, parallel to the basal plane [123]–[126].

Equations were developed to estimate the uniaxial compressive strength for granular ice ($\sigma_{\mathrm{c,G}}$) and columnar ice loaded along ($\sigma_{\mathrm{c,||}}$) or perpendicular to ($\sigma_{\mathrm{c,\perp}}$) the columns of Arctic first-year sea ice [127]:

$$\sigma_{\mathrm{c,||}} = 37\,\epsilon^{0.22}\left[1-\left(\frac{\nu_{\mathrm{T}}}{270}\right)^{0.5}\right] \qquad \mathrm{MPa} \qquad 28$$

$$\sigma_{\mathrm{c,\perp}} = 160\,\epsilon^{0.22}\left[1-\left(\frac{\nu_{\mathrm{T}}}{200}\right)^{0.5}\right] \qquad \mathrm{MPa} \qquad 29$$

$$\sigma_{\mathrm{c},G} = 49\,\epsilon^{0.22}\left[1-\left(\frac{\nu_{\mathrm{T}}}{280}\right)^{0.5}\right] \qquad \mathrm{MPa} \qquad 30$$

The prefactors are determined empirically [127]. The total porosity is calculated in Section 3.4.1 Equation 26.

4 Methods

Section 3 gave an overview of the main topics affecting the measurement methods presented in this section. The conducted tests can be divided into two main groups: tests performed in the field on the SA Agulhas II and laboratory tests. Both test groups yield different results and are necessary to get a complete picture of sea ice in the Antarctic region. Laboratory tests are used to set up testing equipment for field campaigns and collect basic knowledge on sea ice, while tests in the field give insights into actual sea ice conditions in the Antarctic region.

The Institute for Materials Science of the University of Duisburg-Essen provides a cold laboratory with adjustable temperatures down to -25 °C. The laboratory is a converted freezer container, equipped with electricity, a fire alarm system, safety equipment, a workplace, and a wave tank. The exact mode of operation is presented in the Section 4.2.1.

The SA Agulhas II, as shown in Figure 18, is a South African research vessel keel laid in 2011. It has an overall length of 134 m, a breadth of 22 m, and is powered by four main engines (4 engines at 3000 kW) [128]. The vessel is rated in polar class 5, it can operate in medium first-year ice with old ice inclusions all year-round [129]. The vessel is equipped with cold storage rooms, which can be used as laboratories if needed. In addition, fully equipped laboratories can be loaded onto the ship. Further special equipment of the ship used for the experiments is presented in the corresponding sections.

Figure 18 *South African research vessel SA Agulhas II.*

4.1 Experiments on the SA Agulhas II

Two main experiments were conducted on the SA Agulhas II:

- Viscosity of grease and frazil ice,
- and compressive strength of consolidated ice, pancake ice and ice floes.

To do so, the Institute for Materials Science of the University Duisburg Essen participated in three cruises:

- SCALE Winter Cruise 2019 (18.07.-08.08.2019),
- SCALE Spring Cruise 2019 (12.10.-20.11.2019),
- and SCALE Winter Cruise 2022 (11.07-31.07.2022).

All cruises departed and ended in Cape Town (South Africa). Figure 19 displays the trajectory of the SCALE Spring Cruise 2019, the trajectories for the SCALE Winter Cruise 2019 (Figure A 1) and SCALE Winter Cruise 2022 (Figure A 2) can be found in the appendix.

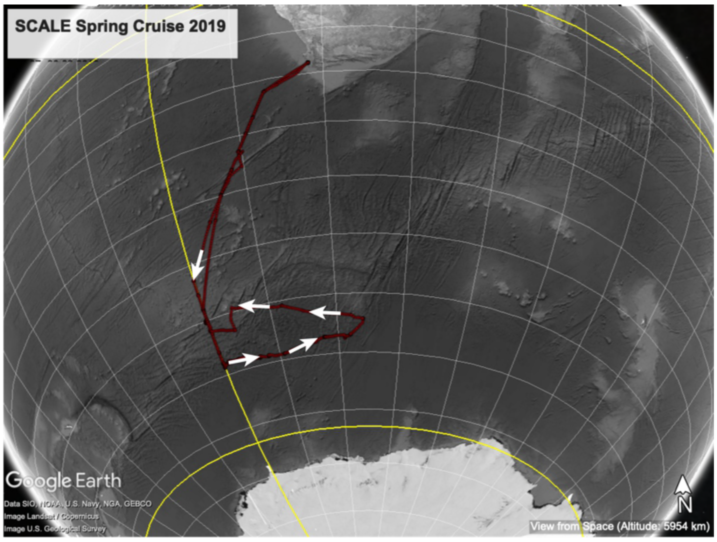

Figure 19 *Trajectory of the SCALE Spring Cruise 2019. The white arrows indicate the direction of the cruise.*

In this chapter the experimental setups and procedures for both tests are explained, as well as the advancement of the testing techniques.

4.1.1 Compression test

On all three cruises, compression tests were conducted. The sampling method, sample preparation, and testing devices are explained in this section. The sampling method did not change much during the three cruises, but the testing device and technique were improved significantly over time. For the SCALE Winter and Spring Cruise 2019, an industrial GCTS compression device was purchased. As the device is originally designed for rock testing, changes were made to meet sea ice requirements (Section 4.1.1.3). To overcome the disadvantages of the GCTS testing device, a new device was developed for the SCALE Winter Cruise 2022 (Section 4.1.1.4).

4.1.1.1 *Sampling*

Sea ice was collected either from pancake ice floes, which were lifted onto the ship, or from consolidated sea ice floating in the ocean.

Pancake ice floes appearing representative for the area were selected and then lifted via a large net moved underneath the floes. After pulling the pancake ice floes up onto the ship's deck with a crane, the samples could be collected. The weight of the pancake ice floes was limited to 5 t by the maximum load-bearing capacity of the crane. Four wooden grids with a height of 20 cm were placed on the deck before unloading the pancake ice floes onto them, to prevent melting of the floes from the ship's heating as well as prevent harming the ship from the corer. Figure 20 shows how a pancake ice floe is placed on a grid. Afterwards, the net is removed and the coring of the pancake starts.

Samples from consolidated ice were retrieved by lowering a basket with three people on the ice. These operations could only be done during daylight, while pancake ice floe collecting could also be done during the night. Furthermore, weather conditions had to be stable during the whole time. The people lowered onto the ice, were harnessed to the basket over throughout sampling. Once the basket was set onto the ice, coring was started. After coring, the basket was lifted back onto deck and the coring team was replaced by a new team to continue coring.

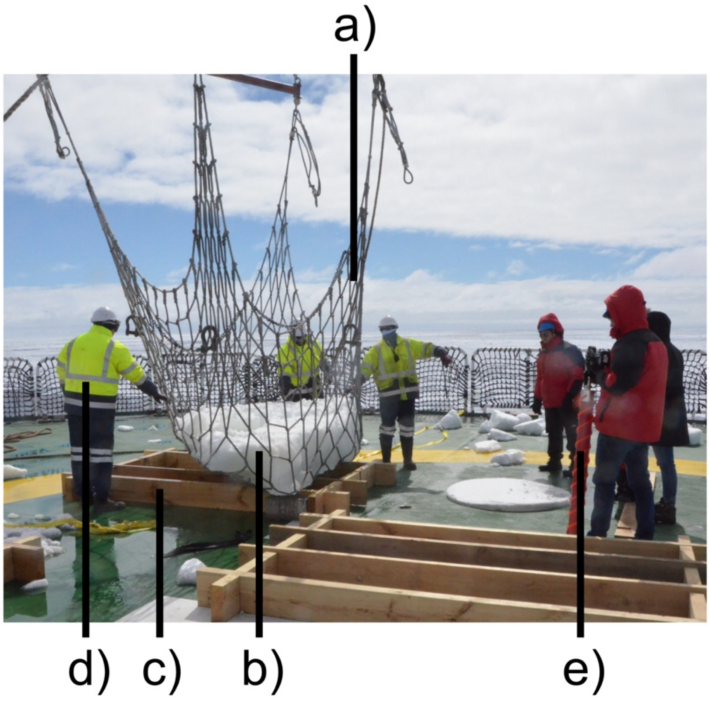

Figure 20 *Picture from pancake ice lifting during the SCALE Spring Cruise 2019. a) Net to lift the ice floe; b) ice floe on the inside of the net; c) grid to prevent harm of the ships deck; d) crew putting the ice floe on the net; e) members of the sea ice team preparing for coring.*

For pancake and consolidated ice, a special core drill (Figure 21) was used to obtain samples from the ice. The core drill hole had an inner diameter of 9 cm resulting in samples with the same size. The length of the cored sample depends on the thickness of the ice but was limited to 1 m by the sea ice corer. The top of the corer (Figure 21 i)) is either attached to an electric or fuel-driven drill. The bottom part has two blades attached to cut into the ice (Figure 21 i) b)) and two metal brackets (Figure 21 i) a)) to prevent the ice from sliding out of the corer once drilling is completed. After drilling, the drill is removed, and the ice core is slid out of the corer into a labeled plastic bag. Besides cores for the compression test, cores for salinity, temperature, and several other measurements were collected. Temperature measurements of the cores started immediately after coring. Depending on the environmental conditions while on consolidated ice, temperature measurements were either done directly on the ice or as soon as the basket was lifted back onto the vessel. All core positions were logged for tracking and for context between the measured values. Afterwards, the cores were immediately transported to a -10 °C cold freezer.

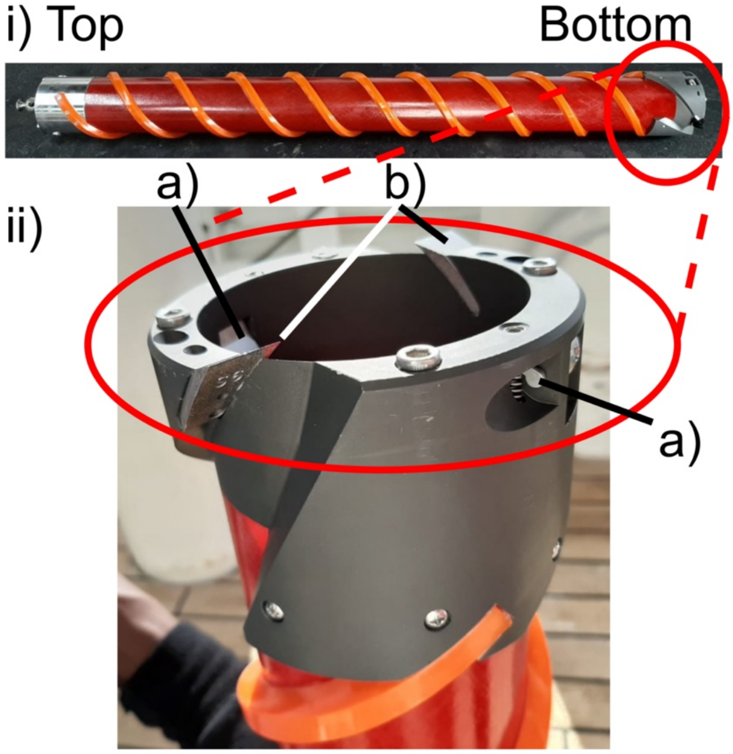

Figure 21 *Sea ice corer used during all cruises. i) The drill is attached to the top (left hand side), the bottom (right hand side) cuts into the ice. ii) Two blades b) cut into the ice. Two metal brackets a) prevent the core from sliding out of the corer.*

4.1.1.2 *Sample preparation*

After completing the sea ice sampling as described in Section 4.1.1.1, the actual sample preparation for testing started. The retrieved cores had varying lengths, some of them were broken and the uneven top and bottom surfaces did not allow testing of the unprocessed cores. The cores were usually stored between 1 to 5 days between coring and sample preparation, depending on the conditions and tasks during the cruise. Before starting the actual sample preparation, photos of the sea ice core, as shown in Figure 22, were taken. After taking photos and measuring the core, it was decided how to cut the core into samples for optimal testing. For cutting, natural constraints like flaws, holes, and existing fractures were considered. The maximum size for a sample depends on the testing device used. The core requirements for the GCTS testing device presented in Section 4.1.1.3 has different core requirements than the custom-designed compression device from Section 4.1.1.4. The GCTS testing device could only test samples up to a length of 13.5 cm, whereas the custom-designed compression device could test samples with a length from 18 cm up to 22.5 cm and samples with a length from 9 cm up to 14 cm. Generally, the sea ice cores were sectioned in a way to obtain the largest samples possible, but to prevent wasting too much of a core, smaller samples were tested as well.

Samples were cut to the maximum length to best meet the requirements of a diameter-to-length ratio of 1:2.5 as explained in Section 3.6.2. Figure 22 i) exhibits the above-mentioned procedure. The core broke during coring into a top and bottom piece, only allowing one large and one small sample to be cut from the top part. The bottom part was trimmed on both ends of the section to create flat surfaces. After cutting the obtained samples were weighed (only for the SCALE Winter Cruise 2022). All information about cutting, fractures, weight, and length of the resulting samples was documented.

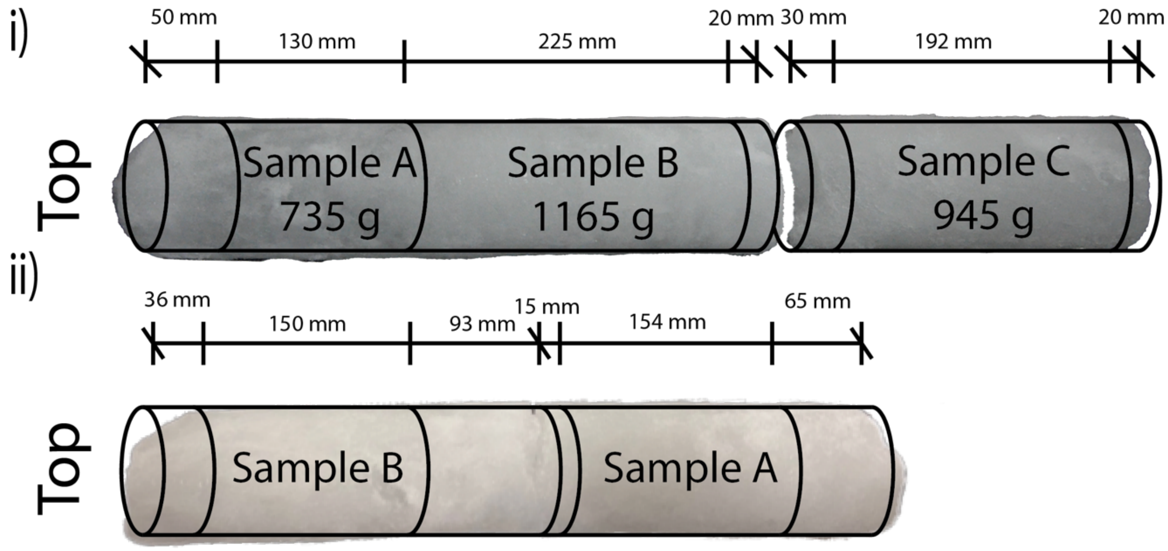

Figure 22 *Sea ice cores from the SCALE Winter Cruise 2022. The lines show the further processing of the sea ice cores.*

Each sea ice core and sample received a unique name to save the data of each core separately. The names of the cores were developed to enable connecting data from different experiments at the same location easily. The name of the top sample in Figure 22 i) is 22WIN-OD4-DE-3-A. The different parts of the name have the following meaning:

- **22WIN**: The core originates from the SCALE Winter Cruise 2022. The abbreviation for the SCALE Winter Cruise 2019 is 19WIN and for the SCALE Spring Cruise 2019 is 19SPR.
- **OD4**: The ice core got sampled at station OD4. Other stations are
    - Winter Cruise 2019: M01; M03
    - Spring Cruise 2019: MIZ2; MIZ3; MIZ6; MIZ7; MIZ8; MIZ9
    - Winter Cruise 2022: B1/B2; OD2; OD3; OD4
- **DE**: The ice core was supposed for the compression test of the Institute for Materials Science of the University of Duisburg-Essen. The test of each core was set before coring started, because different tests had different requirements for the coring process. Therefore, each experiment had a different name.
- **A**: As explained before, the cores were cut into multiple samples. The first sample from the top was named “A”, samples below sample “A” were named alphabetically.

Samples from pancake ice floes collected on the SCALE Winter Cruise 2019 and floes collected on the SCALE Spring Cruise 2019 had an additional letter in between the supposed test (e.g. “DE”) and the sample specification (e.g. “A”) indicating the floe it was taken from. A specification was necessary, as up to four floes were lifted per station. Therefore, the letters “A”, “B”, “C” and “D” were used to name the different floes.

The original locations of the cores on a floe were logged. On consolidated ice, the relative positions of the cores among them were charted on a map. As salinity, porosity, and temperature could not be measured on compression samples, this information was taken from cores close to the compression core. The best cores to do so could be located with help of the core name and map.

4.1.1.3 *GCTS PLT-2W Compression device*

The PLT-2W compression device (Figure 23 i)) is manufactured and developed by the company GCTS Testing Systems. It is designed to measure the point load strength and uniaxial compression of rocks and concrete by applying controlled stress. Its biggest advantage is its compact size and weight of only 16 kg, making it easy to transport and to set-up at different locations. Its maximum load is 100 kN, which was estimated to be enough for sea ice testing. The highest measured compressive strength for Antarctic sea ice is 8.1 MPa [20], which would result in 51.5 kN for our sample geometry. The GCTS system is powered by manually stroking a pressure pump. Applied pressure and resulting displacement are measured by two sensors and everything is recorded and displayed on a mobile device. [130]

The GCTS system, displayed in Figure 23 i), was improved (Figure 23 ii)) by the Institute for Materials Science of the University of Duisburg-Essen for testing of sea ice. The original unconfined compression plates, where the sample is placed onto, had a diameter of only 63 mm, which is too small for sea ice samples with a diameter of 9 cm. To resolve this problem, new compression plates with a larger diameter ($d_{ia} = 98\,\mathrm{mm}$) were manufactured (Figure 23 ii) b)). The top plate was removed to have easier access to the testing chamber and to be able to carry the device better to and from the cold laboratory (Figure 23 ii) a)). While applying load to the sample the bottom plate slides along the steel rods on the left- and right-hand sides. The steel bracket, which slides along the steel rods is narrow and got stuck regularly. Therefore, it got widened (Figure 23 ii) c)). The electronic components for the measurements are located directly under the compression plate. This would be unproblematic for testing dry materials, but brine and water draining from the ice might harm the electric components. For this reason, all slits were sealed with silicone (Figure 23 ii) d)). Lastly, the mobile phone holder attached by the manufacturer to the testing device, was removed and placed next to the device during testing.

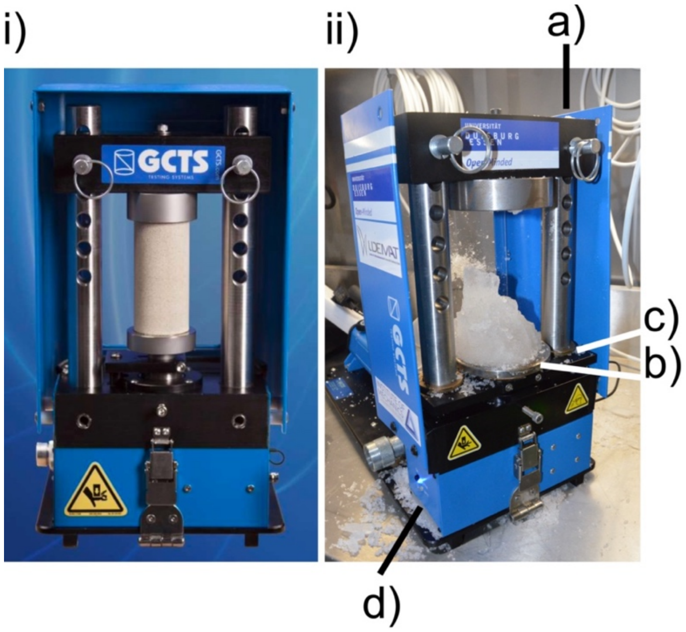

Figure 23 *The purchased compression device i) and the used compression device ii). The following things were changed in the used compression device: a) the top plate was removed to have better access to the testing chamber; b) compression plates with a larger diameter were installed; c) the ring of the lower plate was extended; d) all slits are closed to prevent the penetration of water.*

While using the GCTS testing device, some drawbacks of the device were noticed:

- Data storage: The mobile application showed time-load and load-deformation curves during the test but just recorded the peak stress. Therefore, all tests had to be saved by screenshotting the plots after testing and the data had to be recovered from the screenshots. Asides from the high workload, this method is also inaccurate. If the test ran for too long, the x-axis (time and displacement) expanded further, which made the data difficult to read as it got compressed.
- Arrangement of the electric components: The electric components are located underneath the bottom compression plate in an unsealed container. Liquids originating from the ice, or from condensed water when the device is removed from the cold laboratory could harm the electric components.
- Stiffness of the system: The device was developed for smaller samples, proven by the fact that the original compression plates had to be replaced by plates with a larger diameter. The low stiffness of the device could affect the results.
- Stiff connection of compression plate: Both compression plates had a stiff connection to the bottom beam respectively to the hydraulic cylinder. If the sample ends were not parallel, an uneven load distribution occurred within the sample. An uneven load distribution can lead to an early fracture of the sample.
- The precision of the displacement measurement: The deformation of the sample was recorded with help of only one displacement sensor. If the sample deformed unevenly, one displacement sensor is insufficient for recording the displacement of the sample. Due to the inaccurate readings from the mobile phone, it could not be determined if the inaccuracy was caused by the sensor, the mobile phone or the application.
- Limited disassembling not possible: disassembling of the device is crucial for shipping, repairing, and setting up in the laboratory. The device is difficult to disassemble and not ideal for its intended use.

4.1.1.4 *Custom-designed uniaxial compression device*

To resolve the problems of the GCTS testing device mentioned in Section 4.1.1.3, a new setup was designed for the SCALE Winter Cruise 2022. The custom-designed compression device, displayed in Figure 24, is a stress-controlled compression device, similar to the GCTS device. The hydraulic pump, the hydraulic cylinder, and the pressure sensor were reused from the

GCTS compression device. The custom-designed uniaxial compression device has an overall height of 440 mm, compared to 303 mm of the GCTS device. The diameter of the vertical stainless-steel rods increased from 20 mm to 50 mm. The cross-section of the bottom and top aluminum bars of the custom-designed compression device is 80 mm times 80 mm, while the dimensions of the GCTS top beam are 50 mm times 50 mm.

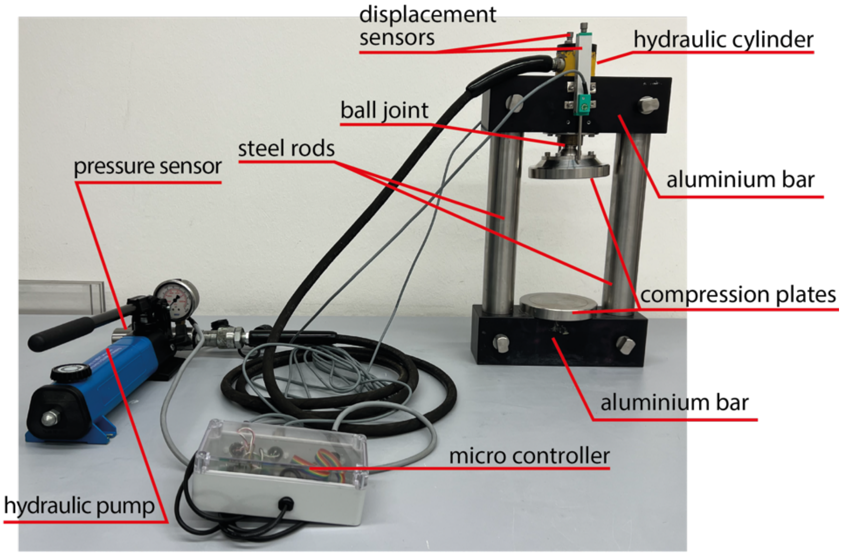

Figure 24 *Custom-designed uniaxial compression device. The pressure sensor, hydraulic pump and hydraulic cylinder were reused from the GCTS testing device.*

The top and bottom compression plates are made from stainless steel and have rough surfaces to prevent slipping of the sample on the plates. Even though rough surfaces are against the rules from Section 3.6.2, they are necessary for this setup. To compensate for uneven or-non parallel sample ends, the top plate is connected to the hydraulic cylinder via a ball-and-socket joint. The maximum displacement of the frame was calculated to be $\Delta l = 0.221\ \mathrm{mm}$ under a load of 100 kN (Figure A 3). After manufacturing the device it was tested to have a deflection of 0.5 mm when loaded with 100 kN. The hydraulic hand pump powers the hydraulic cylinder while a piezo-resistive transducer (MSPT-30W) is connected to the hydraulic circuit. The piezo-resistive transducer changes its electrical resistance depending on the external strain respectively load applied. Instead of one displacement sensor as used on the GCTS device, two displacement sensors are attached on both sides of the top bar. Two displacement sensors allow the measurement of uneven displacement of the sample by calculating the average value of both sensors. The displacement of the top compression plate is measured by the displacement sensor’s tips touching the surface of the top compression plate. Linear potentiometric displacement sensors (Burster 8713) were chosen for this setup. For this sensor type, the output resistance is directly proportional to the linear displacement of the sensor.

For processing the data from the two displacement sensors and the pressure sensor the ESP32 (Espressif) microcontroller was chosen. The analog-to-digital converter (ADC) embedded in the microcontroller purchased for the new compression device, was replaced by an external ADC (ADS1115), due to the nonlinearity of the embedded analog-to-digital converter (ADC). The ADS1115 has a higher resolution, and it allows measurements on smaller scales compared to the embedded one. The analog-to-digital converter starts reading the input signals as soon as the test is started. Fluctuations in the digital output are stabilized by passing the signal through a filter. The signal from the ADC is converted to the equivalent sensor parameter through characterization equations obtained by calibrating the sensors. Afterward, the sensor data is transferred via a serial USB to the computer. On the computer, the data is processed in a self-programmed LABVIEW application. The LABVIEW surface allows to monitor the displacement, and pressure load during the test.

4.1.2 Rheological Test

The mechanical properties of frazil ice are unknown. While tests on the growth, flocculation, and supercooling are common, no examination of the rheological properties of frazil ice with help of a rheometer has yet been performed. Therefore, new sampling methods, testing techniques, and testing protocols were developed. The aim of the newly developed technique is to retrieve undisturbed sea ice samples from the top layer of the ocean. First, the frazil ice sampler is explained, followed by a description of the rheometer and the testing procedure. The experimental setup to investigate the rheological properties of frazil ice are also presented by Paul et al. [131].

4.1.2.1 *Frazil ice sampler*

The frazil ice sampler is designed to collect undisturbed frazil ice samples from the top layer of the ocean. The collected samples have to be large enough, to be representative of the investigated area, but still be good and easy to use. Additionally, the frazil ice sampling should be easily performable and repeatable. It must be noted that the setup is designed without knowing the actual conditions on the vessel and during a cruise.

Figure 25 displays the frazil ice sampler made of stainless steel. The sampler is operated by pulling the green (Figure 25 e)) and red ropes (Figure 25 f)). When pulling the green rope, the steel cylinder (Figure 25 a)) slides along the steel rods (Figure 25 b)) to the top plate (Figure 25 c). The ropes are connected to the bucket via a clamping screw, preventing the rope from material fatigue (Figure 25 h)). The yellow marks (Figure 25 j)) indicate how deep the frazil ice sampler is immerged into the ocean to retrieve a full sample. After pulling up the metal cylinder, the sampler is attached (Figure 25 i)) to the A-frame crane (Figure A 4) of the vessel and lowered to the ocean surface. The A-frame carries the weight of the sampler, while the green and red ropes are only used for opening and closing. The sampler is held in position with the help of ropes attached to hooks on the top plate (Figure 25 k)). By releasing the green rope (Figure 25 e)) and pulling the red rope (Figure 25 f)), the metal cylinder slides to the bottom plate and forms a watertight bucket. Between the loop on the underside, a 'semi-cylindrical metal roll' (Figure 25 g)) is placed to reduce the friction between the rope and the metal plate. A foam mat (Figure 25 d)) is attached to the bottom plate, to prevent water from draining out.

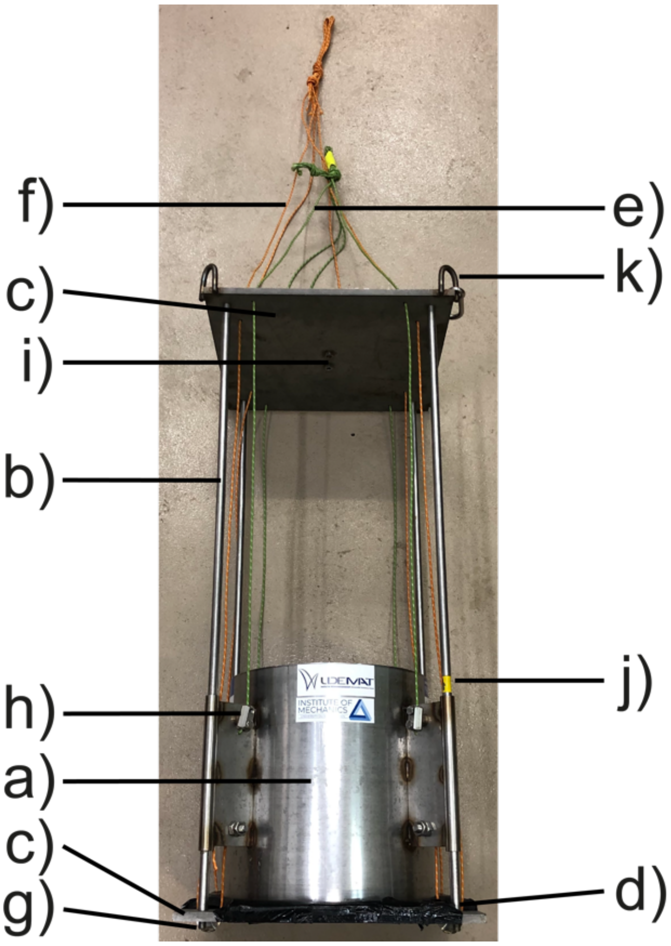

Figure 25 *Frazil ice sampler: The bucket a) can slide along the steel bars b). a) metal cylinder; b) steel bars; c) metal plates; d) foam mat; e) green rope; f) red rope; g) semi-cylindrical metal roll; h) metal bolt; i) metal hook; j) yellow mark; k) metal hook*

4.1.2.2 *eBT-V Rheometer*

Originally designed for fresh concrete by Schleibinger (Schleibinger Geräte Teubert u. Greim GmbH, Germany) the eBT-V rheometer was chosen for this study. The rheometer is robust and is originally designed to test concrete on construction sites. Therefore, it was assumed that the device will also withstand the harsh conditions in the Antarctic. It is compact, portable, battery-driven, and controlled by a smartphone, enabling usage on a cruise. The device can be operated in two different modes: P- and V-mode. For the study of frazil ice, the V-mode is chosen.

For the test, the vane geometry (Figure 26 iii)) is attached to the rheometer as shown in Figure 26 i) f). The vane geometry has a radius of $R_V = 75\ \mathrm{mm}$ and is $h = 150\ \mathrm{mm}$ high. The rheometer is switched on (Figure 26 i) a)) and placed into the frazil sampler (Figure 26 i) g)) by holding it by the handles (Figure 26 i) d)). The measurement principle of a rheometer works as follows: The rheometer starts rotating the vane geometry with a certain speed measured in revolutions per time. Meanwhile, the rheometer records the resistance torque of the measured fluid applied onto the vane. This information, besides dimensions of the measurement geometry and test container, is necessary for calculating the shear rate $\dot{\gamma}$, shear stress τ and viscosity η. The battery is stored behind a waterproof cover (Figure 26 i) b)). Three lights (Figure 26 i) c)) show when the device is switched on and if a measurement is running. Twelve steel rods (Figure 26 i) e) and Figure 26 ii) a)) are attached around the measurement geometry to prevent wall slip on the container surface. The effective radius of the steel rods is 244 mm.

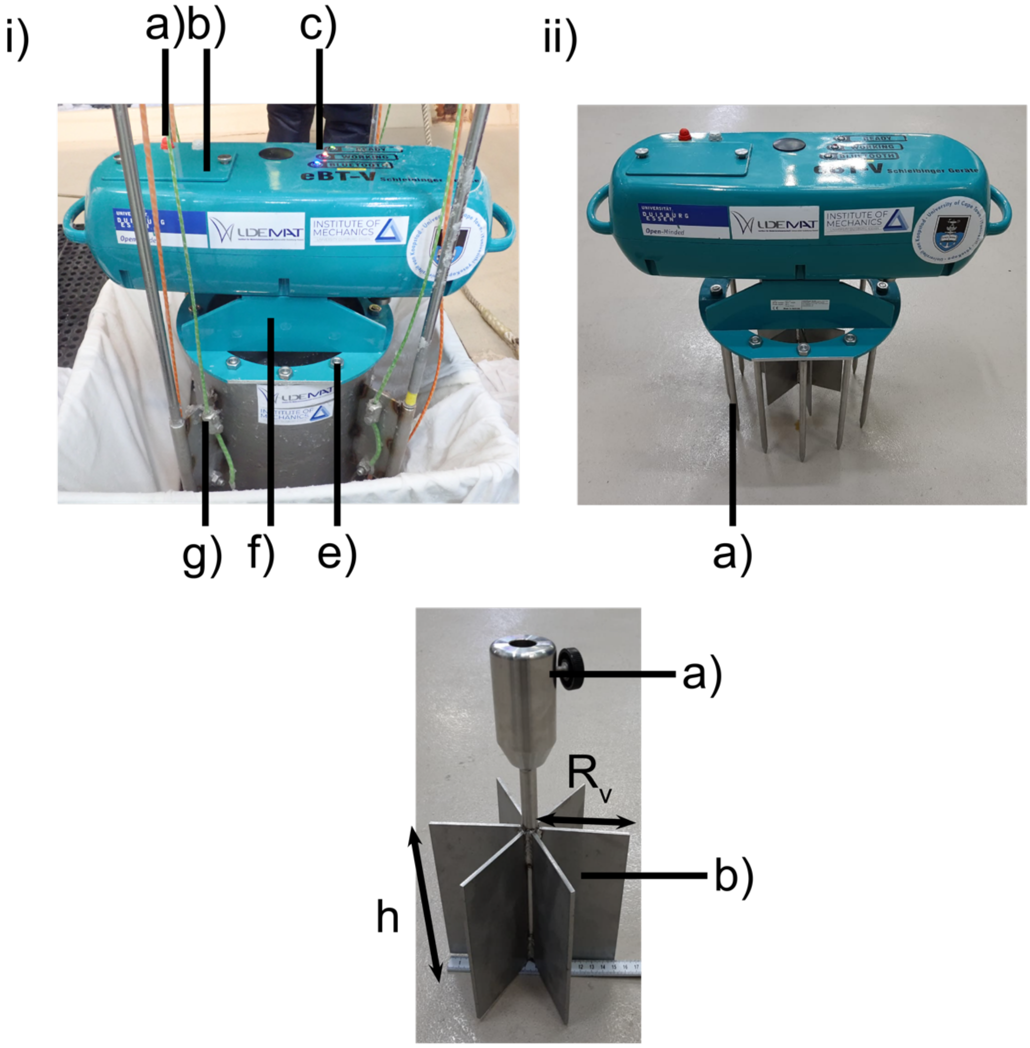

Figure 26 *eBT-V Rheometer i) ii) and vane measurement geometry ii). i): a) power button; b) battery case; c) control lights; d) handle; e) screws with steel rods (hidden in the frazil sampler); f) shaft to fast vane geometry hidden behind green metal plate. ii) a) steel rods. iii) Radius of the vane geometry R_v and height h.: a) screw to fasten vane geometry; b) six vanes.*

4.1.2.3 *Rheological measurements*

Rheology is the study of a material's behavior to applied stress or strain [132]. All materials, even solids like steel (yield point of steel), show rheological properties. This section focusses on the basics of rheology and the vane method.

A fundamental hypothesis by Newton says that the relative velocity of a fluid depends on the internal friction of the particles [133]. Liquids following this law are called Newtonian fluids:

$$\tau = \eta \cdot \dot{\gamma} \qquad 31$$

The shear stress τ in $\frac{\mathrm{N}}{\mathrm{m}^2}$ depends on the apparent viscosity η in $\mathrm{Pa} \cdot \mathrm{s}$ and shear rate $\dot{\gamma}$ in $\frac{1}{\mathrm{s}}$. For Newtonian fluids the shear stress increases linearly, with the slope being the viscosity. The viscosity is constant over all strain rates:

$$\frac{\tau}{\dot{\gamma}} = \eta \qquad \mathrm{Pas} \qquad 32$$

The viscosity of water at 20 °C is $10^{-3}\ \mathrm{Pa} \cdot \mathrm{s}$, which is equivalent to $1\ \mathrm{mPa} \cdot \mathrm{s}$. But not every fluid behaves like a Newtonian fluids. Some liquid exhibit viscosities that are not constant over time but increase or decrease with increasing strain rate. They are called power law fluids. Liquids showing an increasing viscosity are called shear thickening, whereas liquids with decreasing viscosity are called shear thinning.

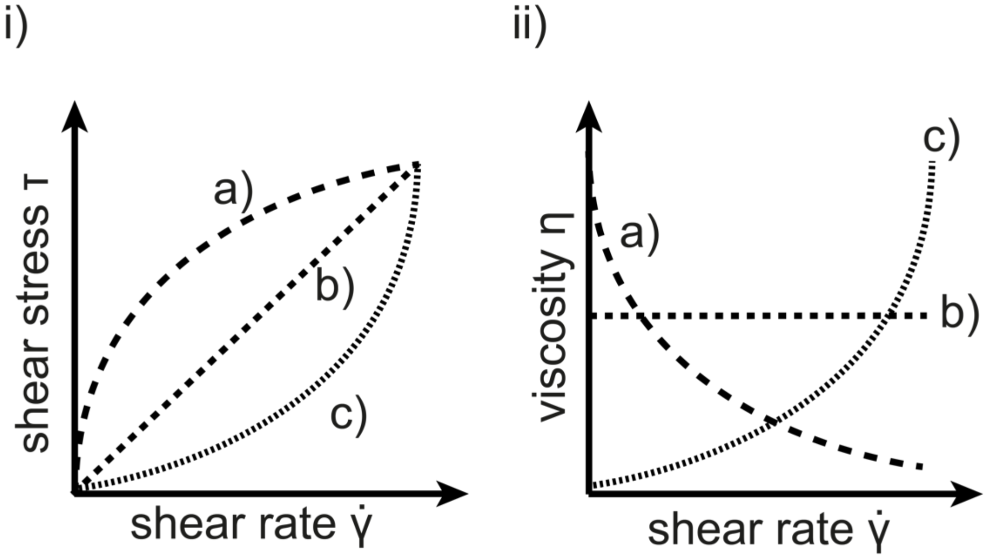

Figure 27 *i) shear rate vs. shear stress; ii) shear rate vs. viscosity. For both graphs is a) shear thinning behavior, b) Newtonion behavior and c) shear thickening behavior.*

Figure 27 shows a i) shear rate vs shear stress plot and a ii) shear rate vs viscosity plot. Both plots in Figure 27 show shear thinning a), Newtonian b), and shear thickening behavior c).

Shear thinning fluids do not show a yield point. The yield point is the area in a shear rate vs. shear stress plot, where the viscosity leaves the elastic region and starts to deform plastically [134]. Before reaching the yield point, a fluid can be treated like a solid. Instead of a yield point, shear thinning fluids show a limiting viscosity at very low shear rates [135]. Products showing a shear thinning behavior are for example polymer melts and fruit or vegetable products [132].

Shear thickening behavior can be obtained in corn starch solution. Due to applied stress, the microstructure of the fluid changes which leads to an increase in viscosity [135].

The most common model to describe different flow curves is the Herschel-Bulkley general model [132]:

$$\tau = \tau_0 + k\dot{\gamma}^n \qquad 33$$

τ_0 is the yield stress, k the consistency index and n the flow behavior index. The model is often used as it can describe shear thinning ($0 < n < 1$ and $\tau_0 = 0$) and shear thickening ($1 < n < \infty$ and $\tau_0 = 0$) behavior. Bingham plastics (n=1 and $\tau_0 > 0$) and Newtonian fluids ($n = 0$ and $\tau_0 = 0$) are also special cases of the Herschel-Bulkley general model. All cases for the Herschel-Bulkley general model can be seen in Table 5.

Table 5 *Parameters for the Herschel-Bulkley General Model. According to* [132].

Fluid	τ_0	n
Herschel-Bulkley	>0	$1 < n < \infty$
Shear thinning	0	$0 < n < 1$
Shear thickening	0	$1 < n < \infty$
Bingham	>0	1
Newtonian	0	1

Similar to Equation 32, the apparent viscosity is calculated by dividing the shear stress τ by the shear rate $\dot{\gamma}$:

$$\eta = \frac{\tau}{\dot{\gamma}} = \frac{\tau_0 + k\dot{\gamma}^n}{\dot{\gamma}} = \frac{\tau_0}{\dot{\gamma}} + k\dot{\gamma}^{n-1} \qquad 34$$

Power law fluid flow behavior is time-independent. However, there are also liquids showing time-dependent property changes. These materials are called thixotropic and rheopectic. Thixotropic materials show increasing shear stress under a constant strain rate, whereas rheopectic materials show a decrease in shear stress under a constant strain rate. They can be described as time-dependent thinning (rheopectic) or thickening (thixotropic) [135].

Shear rate and shear stress can be investigated with the help of a rheometer. As previously described, rheometers are used to measure the viscosity of fluids. All rheometers consist of two main components: the measurement geometry and a cup with the sample. Rheometers can be divided into two groups: Searle and Couette rheometers [136]. In a Searle rheometer, the inner measurement geometry starts rotating and the outer cup stays stationary. The Couette method works the other way around. On that basis, the eBT-V rheometer can be specified as a Searle rheometer.

Dzuy and Boger [137] derived an equation to determine the shear stress of a vane rheometer from the torque along the cylindrical surface of the vane geometry and the top and bottom surfaces:

$$M = 2\,\pi R_V^2 h \tau_w + 2[2\pi \int_0^{R_V} \tau_e(r) r \, dr \, r] \qquad 35$$

The stress along the cylindrical wall is τ_w, whereas the stress at the end surfaces depends on the radius r is τ_e. Knowing that $\tau_e(r) = \tau_w$ the equation can be transformed to the shear stress:

$$\tau = \frac{M}{2\pi R_V^3}\left(\frac{h}{R_V} + \frac{2}{3}\right)^{-1} \quad \mathrm{Pa} \qquad 36$$

With R_V as the radius of the vane geometry, the shear rate was derived by Krieger [138] for power law fluids in concentric cylinder viscometers with the rotation speed ω in $\mathrm{rad/s}$

$$\dot{\gamma} = \frac{4\pi R_S^{\frac{2}{n}}}{\left(R_S^{\frac{2}{n}} - R_V^{\frac{2}{n}}\right)} \frac{\omega}{n} \qquad \frac{1}{s}. \qquad 37$$

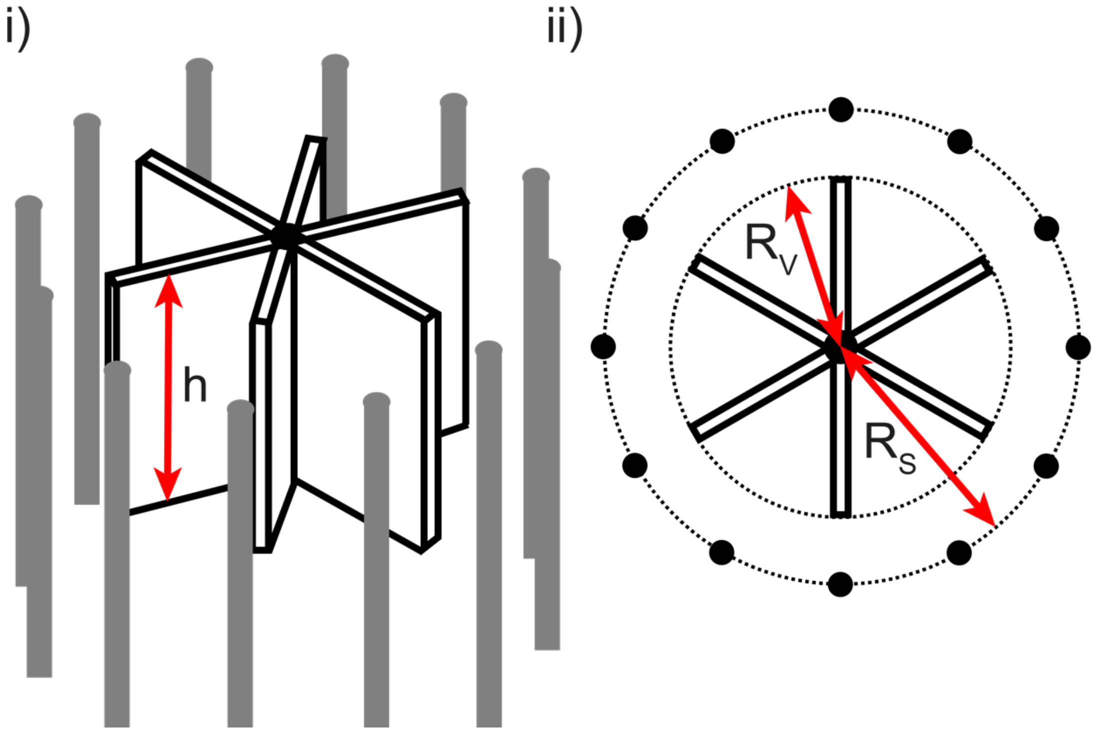

***Figure 28** i) Vane geometry with steel rods to prevent wall slip. ii) top view of the vane geometry with steel rods.*

A drawing of the vane geometry is displayed in Figure 28. The outer ring of steel rods are not necessary for a vane rheometer but prevents wall slip. The effective radius of the steel rod ring is $R_S = 244\ \mathrm{mm}$, the radius of the vane rheometer is $R_V = 75\ \mathrm{mm}$ and the height of the vane is $h = 150\ \mathrm{mm}$.

4.1.2.4 *Testing procedure*

The sampling procedure was devised before the first cruise in 2019 and improved afterwards. For frazil ice testing the frazil ice sampler (Section 4.1.2.1), eBT-V rheometer (Section 4.1.2.2), and equations from Section 4.1.2.3 are needed.

Sea ice sampling and measurement can be best explained in five steps as displayed in Figure 29. In the first two steps, the frazil ice sampler (Figure 25) is used to collect a frazil ice sample. First step the sampler is lowered close to the ocean surface and the metal cylinder is pulled to the top plate of the frazil ice sampler. If the sampler is close to an area with frazil ice it is lowered into the ocean and slowly moved sideways into the frazil ice field. Once the sampler is inside the frazil ice field, the sampler is closed by pulling the metal cylinder to the bottom plate as shown in Figure 25 i). Then, the sampler is lifted onto the deck with the help of the winch of the A-frame (Figure A 4 c)). Once on deck, the temperature and volume of the sea ice sample are measured Figure 25 ii). Afterwards, the rheological properties are determined with the help of the eBT-V rheometer. The rheometer is placed inside the frazil ice sampler directly (Figure 25 iii)). It was decided to leave the frazil ice sample in the sampler for the rheological measurement, to prevent changes of the frazil ice sample. The measurement is started via a smartphone. During measurement, the rotation of the vane starts with a rotation speed of $1\,\frac{\text{revolution}}{\text{minute}}$ and ramps up to $10\,\frac{\text{revolution}}{\text{minute}}$ within 60 seconds.

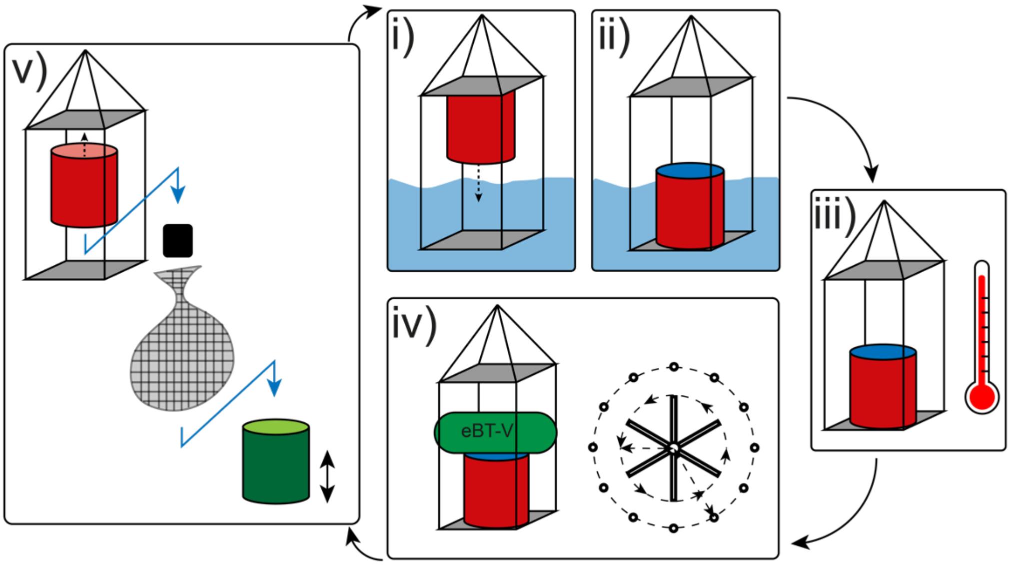

Figure 29 *Five steps of frazil ice sampling and measurement: i) and ii) sampling of frazil ice in the ocean; iii) temperature measurement of the sample; iv) rheological measurement; v) separating frazil ice sample into its components water and floating ice crystals.*

After the rheological measurement ended, the rheometer was removed from the sampler and the frazil ice sample was separated into its components of sea water and frazil ice crystals. This was done by opening the sampler and letting the water flow through a sheet (Winter Cruise 2019) or net (Spring Cruise 2019, Winter Cruise 2022). The water drains through the sheet respectively net into a bucket and the frazil ice crystals are left inside the net / sheet. Thus, the weight of the frazil ice including the net is measured and the volume of the drained water inside the bucket is measured. From both results the relative quantity of each component in the sample are calculated in volume percent.

4.2 Experiments in the laboratory

Laboratory experiments are crucial for understanding sea ice processes in the Antarctic region. On the one hand, laboratory experiments are necessary to develop equipment for the cruises and to verify results from the field. On the other hand, laboratory experiments allow the observation of natural processes in more detail. As described in Section 3.5.1, many experiments conducted to improve the knowledge on frazil ice crystals were performed in the laboratory. The disadvantage of laboratory sea ice tests is that the results represent only very young sea ice, as the experiment can be scaled to a smaller size but not time [139].

Most of the laboratory experiments presented in this study were performed in the polar laboratory of the Institute for Materials Science at the University of Duisburg-Essen shown in Figure 30. The polar laboratory is a modified freezer container equipped with electricity and testing equipment.

Figure 30 *Polar laboratory at the University of Duisburg-Essen with both doors open.*

4.2.1 Polar laboratory

The polar laboratory at the Institute for Materials Science at the University of Duisburg-Essen is a remodeled 20 feet cargo freezer container. It was chosen, as the space inside the university facility is limited and setting up a separate cold room would not have been possible. The 20 feet container has an inside footprint of 13.1 m^2 (width: 2.29 m; length: 5.72 m), and a height of 2.0 m. The container was placed on four point-foundations on a small parking area of the university. To power the container an electric sub-distribution was installed right behind the container. The temperature of the cargo container is controlled by a cooling unit MAGNUM TK 51122-4-MM and can be set between +30 °C and -35 °C. The temperature control panel of the container is situated on the outside. To meet scientific requirements the container was remodeled, while still ensuring its transportability on a cargo ship to a potential cruise on the SA Agulhas II.

The container can be accessed by a large door at the front of the container, which can be opened over the whole width of the container. The large door is very convenient, if the container is used for cargo and allows bigger research equipment to be loaded, but it is inconvenient for daily research use. For example, it is not possible to open and close the original doors from the inside of the container. This would mean that during research activities the doors have to stay open over the whole time, which would spend a lot of energy. Therefore, another door had to be installed. The original doors should remain so that the container could still be shipped. A second door was installed right behind the original door. The new door allows easier access into the container and can be closed completely while working inside the container. To install the new door, a wall was installed 10 cm behind the original doors. The distance between the new wall and the original doors is just big enough so that the new door handle does not block the original ones. The installed wall and door are filled with Polyurethane rigid foam, the new wall can be operated at temperatures between 80 °C and -40 °C. The thermal resistance of the wall and door is 3.45 m^2K/W. While working inside the container, the original doors stay open and only the newly installed door is used.

Besides the new entrance to the container, new electric connections were installed. While using the container as a cargo freezer, no plugs or lights were installed inside the container, the cooling unit was controlled from the outside and no safety equipment was installed. All new electrics were designed for inside temperatures of -20 °C and outside temperatures of -30 °C in case the container is used on the SA Agulhas II. A new electric sub-distribution was installed inside the container right behind the door. Plugs were installed at different locations inside the container. A ceiling lamp was installed besides an emergency light in case the electricity is interrupted. The plugs, the light, and the cooling unit can be switched off from the newly installed sub-distribution inside the container. Furthermore, a fire detector was attached next to the ceiling lamp which gives an acoustic signal in case of fire. To allow a person to work alone in the cold laboratory, a Deadman's switch was attached next to the door. The switch must be pressed every 10 minutes, otherwise, the container will make an alarm so that someone has to check for the person inside the laboratory. This is especially necessary when the container is working at negative temperatures and can avoid serious harm to people inside the container.

The container has internet access via Lan, allowing online monitoring of experiments. Further equipment in the container includes a table to conduct experiments such as the frazil ice growth presented in Section 4.2.3, and a sea ice tank (Section 4.2.2) with a wave generator to simulate the sea ice conditions in the MIZ.

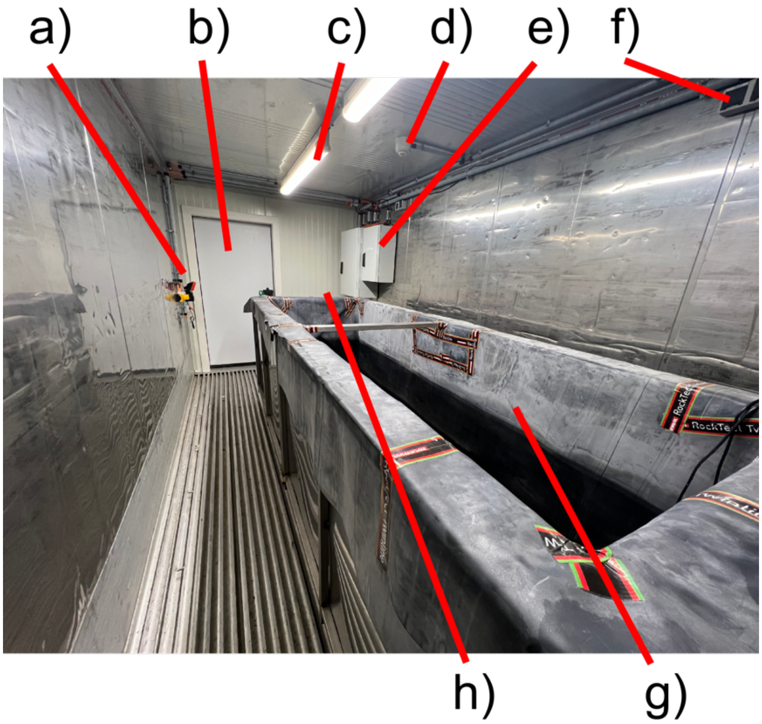

Figure 31 *Cold laboratory at the Institute for Materials Science (University of Duisburg-Essen). a) Emergency switch, Deadman's switch, light switch, emergency light; b) new door with wall; c) light; d) fire detector; e) sub-distribution; f) power plugs; g) water tank; h) (hidden) table for smaller experiments*

Figure 31 shows a picture of the remodeled container. Except for the water tank and table for small experiments, all components are permanently attached to the container.

4.2.2 Wave tank

The sea ice container is equipped with a water tank, shown in Figure 31 g). The tank consists of three layers: an outside non-waterproof stainless-steel container, a layer of insulation material, and a waterproof layer on the inside. Besides that, a wave generator (Figure 32 g)) and bottom heating are attached.

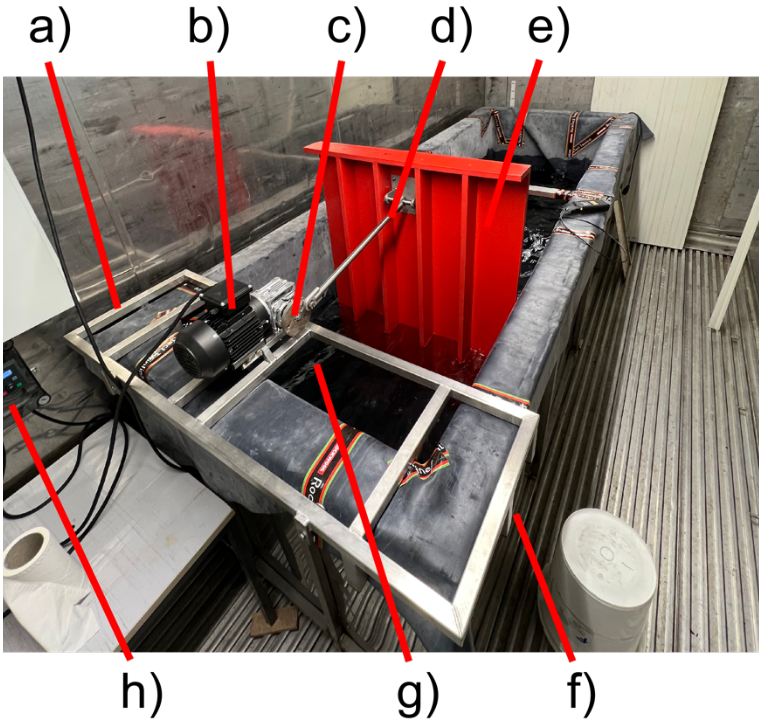

Figure 32 *Wave generator for the sea ice tank. a) Stainless steel frame to hold the engine in position; b) engine for wave generation; c) plate to convert rotating movement into forward and backward movement; d) rod to connect wave paddle to engine; e) wave paddle; f) steel bars to hold the frame in position; g) brace (underneath the water at the bottom of the tank) to change position of the paddle inside the tank; h) control panel for the engine speed.*

The outer steel layer of the tank consists of two identical halves which are connected with the help of clamp fasteners. Each half has a length of 175 cm, a width of 130 cm, and a height of 110 cm on the outside. The separation into two halves enables to load and unload the tank from the container. Between the stainless-steel layer and the waterproof layer, the tank is lined with a heat insulation (Styrodur) to reduce the heat permeability through the tank walls. The insulator has a thickness of 10 cm and is covered by foil to form a watertight tank. The foil (EPDM-foil) is designed for roof construction, it has a thickness of 1.5 mm and it is waterproof. The foil was glued to the steel construction to prevent slipping inside the tank. By not gluing the foil onto the insulation material but into the steal tank, the tank can be detached easily when removed from the container. It must be noted that the container has no drain to prevent having a thermal bridge inside the system. In total, the walls of the tank setup have a thermal heat flux of 7.7 W/m^2 while the open water (-2 °C), which is in contact with the cold air (-20 °C) has a heat flux of 450 W/m^2. The heat flux through the tank is much lower compared to the heat flux between water and air. Additionally, a heating system (140 W/m^2) was installed at the bottom of the tank between the foil and insulation material. The heating system can be adjusted to compensate for the heat flux through the tank walls. Therefore, it is assumed that the heat flux through the tank walls can be neglected for the experiments. Cooling of the artificial tank will only take place through the water-atmosphere interface and not through the wall. The tank has a capacity of 3.2 m^3 (width: 1 m; length: 3.2 m, height: 1 m).

To simulate sea ice growth conditions appearing in the Antarctic Marginal Ice Zone turbulences of the ocean have to be induced. To do so, a wave generator was designed at the Institute for Materials Science. A picture of the wave generator setup attached to the tank is displayed in Figure 32. The wave generator is powered by an engine that is placed on a stainless-steel frame on the tank walls. The frame is held in position by steel bars on the inside and outside of the tank. The position, and thereby the angle of the wave paddle inside the tank can be adjusted by changing the position of the steel paddle on the brace (Figure 32 g)). The speed of the wave generator can be controlled with the help of the control panel (Figure 32 h)). The deflection of the wave paddle, influencing the wave height, is changed by varying the position on the plate shown in Figure 32 c). The plate is attached centric to the crankshaft of the engine. An oblong hole was drilled into the plate to attach a rod (Figure 32 d)) along the hole to change the deflection of the wave paddle. The closer the steel rod is attached to the center of the plate, the smaller the deflection of the wave paddle and vice versa.

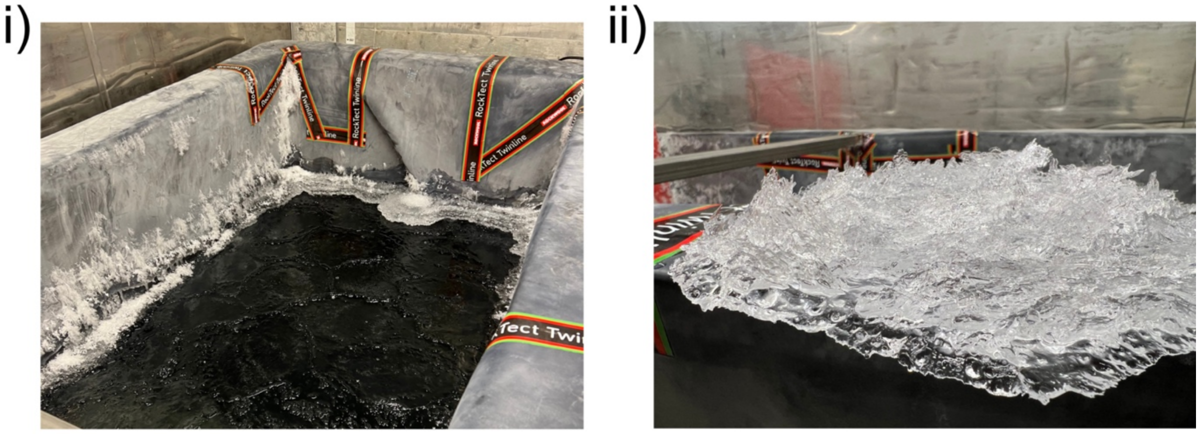

Figure 33 i) *Wave tank with an approximately 5 cm thick ice cover. The ice cover is not completely consolidated, as floes (shown in ii)) can be taken out of the tank.*

Figure 33 shows how ice grown in the wave tank looks like. It is apparent that the chosen turbulence mechanism is suitable to grow artificial ice because different floes (Figure 33 ii)) can be taken out of the water.

4.2.3 Frazil ice growth

To understand the frazil ice mechanics respectively its rheological properties, frazil ice itself must be understood. Therefore, experiments around the freezing point are essential to investigate the effect of turbulence and salinity on seeding and ice growth. To do so, an experiment, derived from Reimnitz et al. [80] and Schneck et al. [90] was performed.

To enable frazil ice growth, a modified setup from Reimnitz et al. [80] was used. The setup can be seen in Figure 34. A magnet stirrer, where the rotation speed could be set in steps of ten rotations per minute (RPM), was placed inside the cold laboratory. A beaker filled with water was placed on top of the magnet stirrer. The beaker used for these experiments is smaller than the container used by Reimnitz et al. [80], it has a diameter of 9 cm and a height of 15 cm. Compared to a diameter of 12 cm and a height of 191 cm by Reimnitz et al. [80]. A thermometer Pt100 was placed inside the beaker to measure the temperature every 2.5 s. A camera was used to record the crystal growth, as presented by Schneck et al. [90]. As frazil ice crystals are difficult to distinguish inside the water, polarization sheets were used to make them visible. A lightbulb was mounted behind the beaker, the first polarization sheet was placed inside the beaker close to the wall, and the second sheet was placed on the outside in front of the camera. The polarization sheet inside the beaker as well as the thermometer were held by a laboratory stand. The setup allowed to record the crystals in between the two polarization sheets. A schematic drawing of the test setup is displayed in Figure 34.

The recording of the videos started before the water temperature fell below the freezing point and stopped about 300 s after the first crystals formed. Afterwards, the recorded video was cut into multiple pictures every 2.5 s and analyzed with the software “ImageJ”. The software counts the number of crystals and measures the size of each crystal. In the end, the temperature measurements were related to the number of formed crystals.

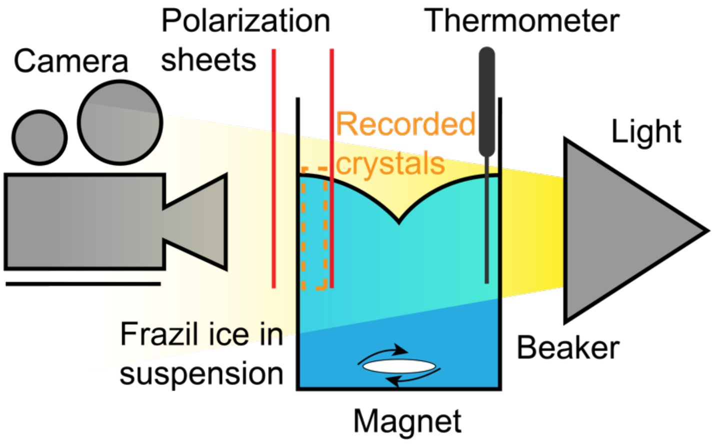

Figure 34 *Setup for artificial frazil ice growth.*

4.2.4 Controlled ice growth

To get a better understanding of ice growth, experiments on the temperature profiles inside samples were performed. Hence, a test setup consisting of a cooling unit, a polymer pipe, and temperature sensors are developed. The idea of the test was to monitor the freezing process of water under calm conditions. The test could be performed in two different directions: freezing of the sample from the top and freezing from the bottom.

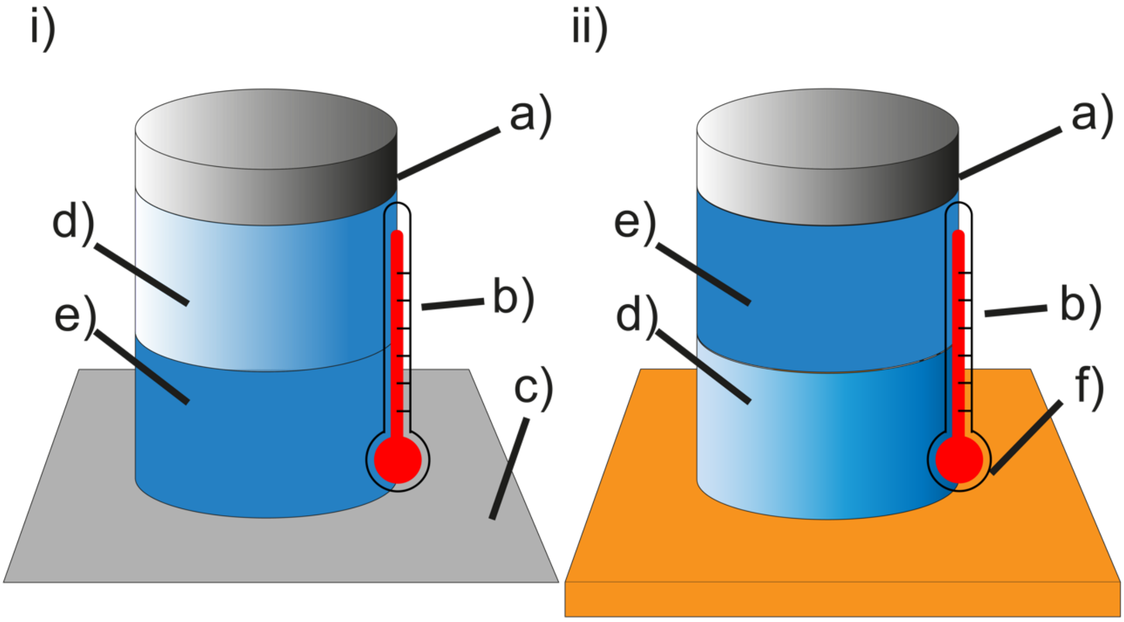

Figure 35 *Bottom-to-top growth in i) and top-to-bottom growth in ii). For i) the bottom aluminum plate is cooled, and the cylinder is insulated. For ii) the cylinder is cooled from the top and the bottom plate consists of insulating material. a) polymer cylinder; b) temperature probe; c) cold aluminum plate; d) water respectively brine; e) ice; f) insulating plate.*

The setup for both experiments is similar: Holes were drilled into a polymer pipe with 3 cm distance between each hole, beginning from the bottom of the pipe. Temperature sensors were put into the drilled holes along the height of the pipe. The pipe was wrapped in soft insulation material, only allowing heat flux from one direction. An aluminum plate was glued to the bottom for freezing experiments from bottom to top and insulation material is glued to the bottom for freezing experiments from top to the bottom. The cooling for the bottom-to-top growth was provided by a cooling unit. The metal plate with the attached cylinder is placed onto a polymer hose attached to a cooling unit. The temperature of the cooling unit can be set between -45 °C to 200 °C. For the top-to-bottom growth, no external cooling unit except for the cold laboratory is necessary. The temperature is controlled by changing the laboratory temperature. A picture of the bottom-to-top growth setup is displayed in Figure 36.

In this study only results for the bottom-to-top growth are presented, because the cooling unit broke after some experiments and the unit could not be repaired. Nevertheless, both setups are presented briefly to show the different ways to grow artificial sea ice under controlled conditions.

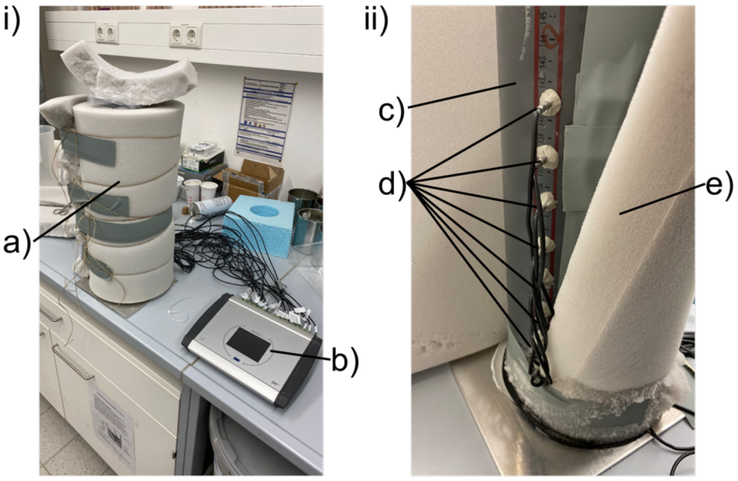

Figure 36 *Device for controlled ice growth from bottom-to-top. i) Polymer cylinder is wrapped with insulating material. ii) If the insulation material is removed, the temperature sensors are visible. a) Insulated polymer cylinder; b) temperature logger; c) polymer cylinder without insulation; d) temperature sensors; e) insulating material.*

5 Results

The results section is separated into the tests performed on the cruises and the results obtained in the laboratory. First, the compression test results and rheological results are presented, followed by frazil ice and consolidated ice growth in the laboratory.

Figure 37 *People working in front of the SA Agulhas II.*

5.1 Compression test

Sea ice compressive strength was tested during three cruises with two different compression tests. In this section the results from each cruise will be presented separately, followed by a comparison between the three cruises as well as the GCTS (see Section 4.1.1.3) and custom-designed uniaxial compression device (see Section 4.1.1.4). The data are analyzed regarding the compressive strength, Young's modulus over the sea ice depth, brine content, and porosity. Besides that, the results are compared to literature values for first-year sea ice.

In total 49 sea ice cores were collected during the three cruises. The 49 sea ice cores resulted in 115 compression samples.

Figure 38 *A pancake ice floe for testing is lifted out of the water.*

5.1.1 Compressive strength: SCALE Winter Cruise 2019

During the SCALE winter cruise 2019, 15 cores were collected, of which 12 cores originated from pancake ice floes and 3 cores originated from consolidated ice. For the SCALE Winter Cruise 2019, the GCTS compression device (Section 4.1.1.3) was used. The data collected with the GCTS compression device are displayed in Figure 39. Figure 39 i) shows a load vs time curve and Figure 39 ii) a load vs displacement curve. Data preparation is shown using sample 19WIN-M01-DE-01-B-C as an example, but the procedure was performed for all samples tested with the GCTS device. The labeling of the x-axis for Figure 39 ii) is wrong due to a bug in the program, instead of “Deformation” it says “Time”. The wrong labeling of the axis is another example for problems with the GCTS device. The correct name of the graph is only displayed in the small title above the graph (“Load vs. Deformation”). The top part of Figure 39 i) and ii) gives information about the current load in kN (“Load, kN”) and displacement in mm (“Deformation, mm”). At the bottom part of Figure 39 i) and ii) the maximum load (“Pk. Load”) of the sample is displayed.

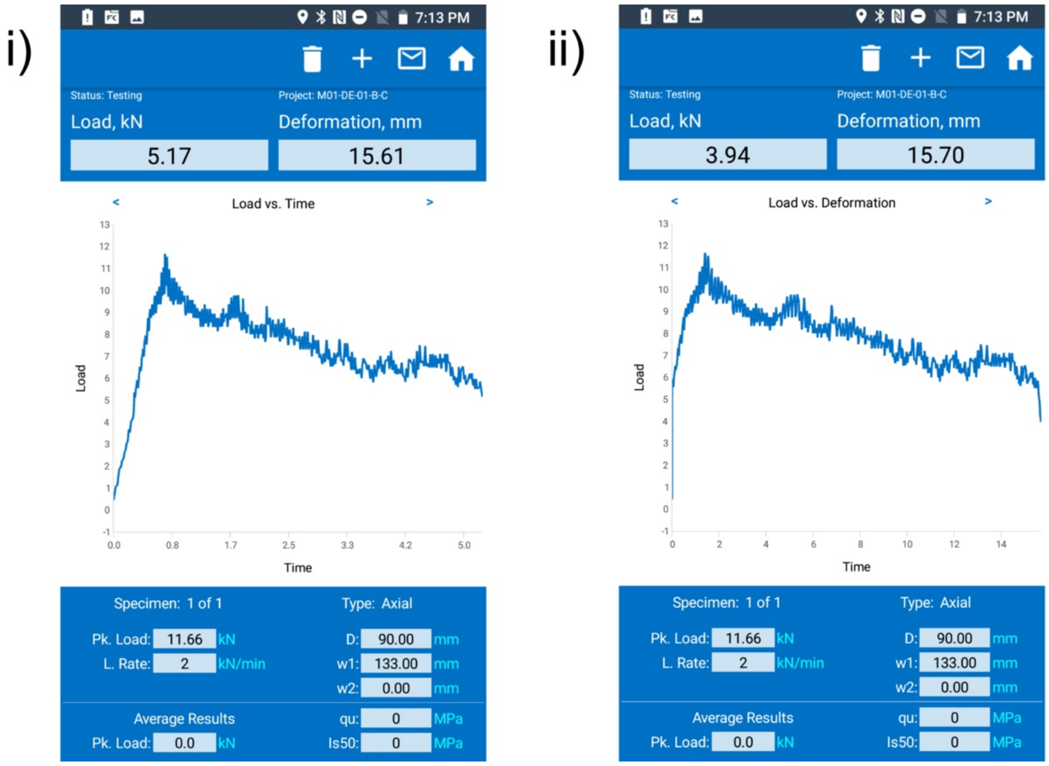

i)

Status: Testing
Project: M01-DE-01-B-C
Load, kN: 5.17
Deformation, mm: 15.61
Specimen: 1 of 1
Type: Axial
Pk. Load: 11.66 kN
L. Rate: 2 kN/min
D: 90.00 mm
w1: 133.00 mm
w2: 0.00 mm
Average Results
Pk. Load: 0.0 kN
qu: 0 MPa
Is50: 0 MPa

ii)

Status: Testing
Project: M01-DE-01-B-C
Load, kN: 3.94
Deformation, mm: 15.70
Specimen: 1 of 1
Type: Axial
Pk. Load: 11.66 kN
L. Rate: 2 kN/min
D: 90.00 mm
w1: 133.00 mm
w2: 0.00 mm
Average Results
Pk. Load: 0.0 kN
qu: 0 MPa
Is50: 0 MPa

Figure 39 *Screenshots of results obtained from the GCTS compression device for 19WIN-M01-DE-01-B-C. i) Load vs. Time graph; ii) Load vs. Displacement graph (labeling of the x-axis is wrong).*

As the data of the GCTS compression device could not be saved in any kind of digital table, the data of each test was saved by two screenshots as displayed in Figure 39 i) and ii). As can be seen in Figure 39 ii) saving data with the help of screenshots lead to loss of data. It appears as if the load increased up to 6 kN without any deformation. The graph is congruent with the y-axis, which is not possible. As it is unclear why the graph is congruent with the y-axis.

Two different reasons are given:

1. Unprecise displacement sensor

   The built-in displacement sensor could be too imprecise to measure very small displacements. Additionally, the displacement sensor may have snagged and failed to record any data.

2. Measured values are too small

The measured values of the displacement sensor are too small to display in the graph. The relatively large displacement after the peak load compressed the small values below 5 kN and they appear as a zero displacement.

It is assumed that both reasons play a role in the unprecise measurement of displacement. However, it is not clear what is the main reason for the inaccuracy.

To get the data from the graphs converted into a table, each screenshot was loaded into a CAD program. For this study, AutoCAD was used. By redrawing the graphs with polylines, the data was captured from the screenshots.

This procedure was applied to every sample tested with the GCTS compression device. The resulting graphs from sample 19WIN-M01-DE-01-B-C respectively Figure 39 are displayed in Figure 40.

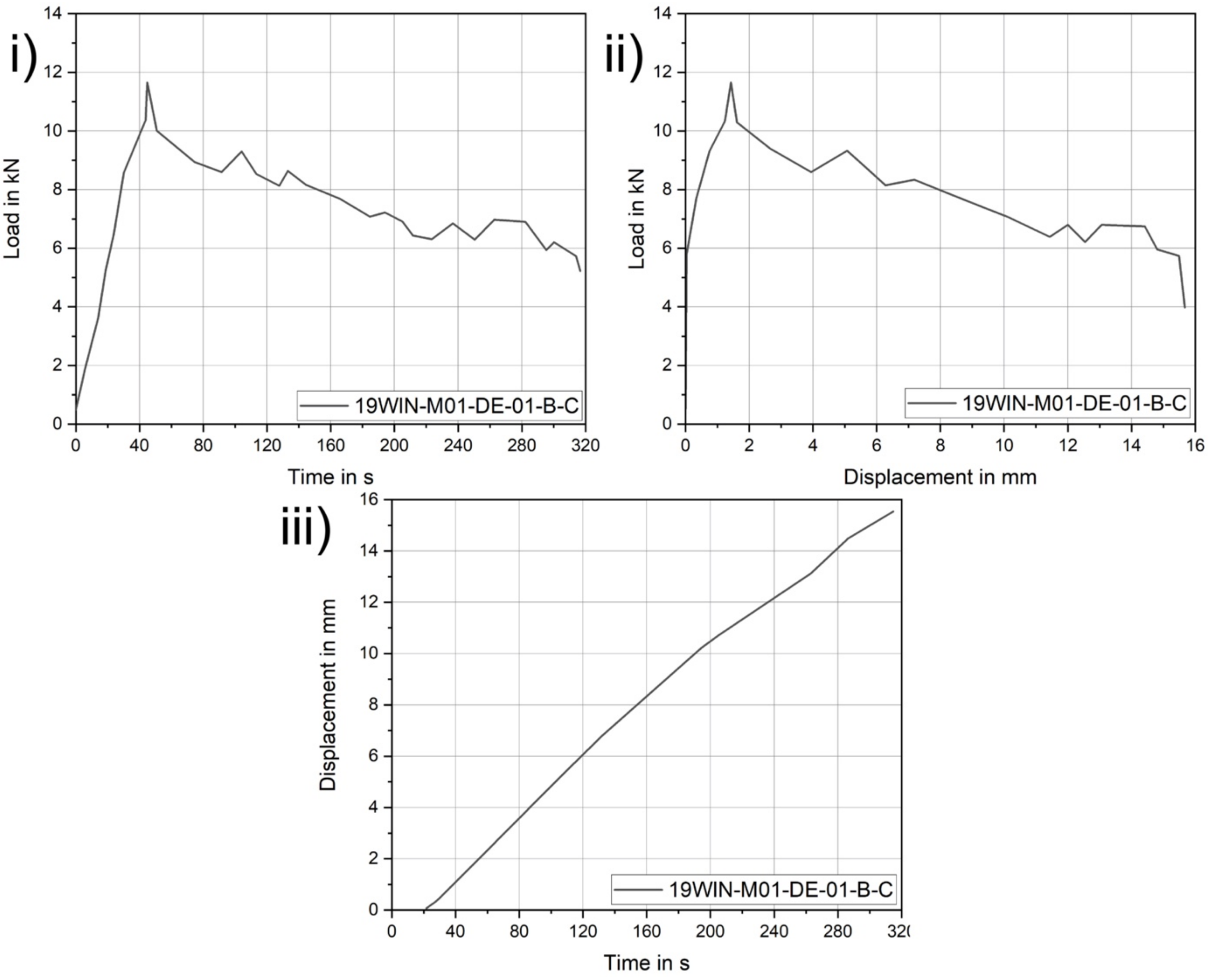

Figure 40 *Data from the screenshots in Figure 39 after transformation for further analysis. i) load vs. time plot as in Figure 39 i); ii) load vs. displacement as in Figure 39 ii); iii) displacement vs. time by combining both screenshots from Figure 39.*

Figure 40 i) displays the load against time plot from Figure 39 i) after transforming the data into a table and plotting it. The plotted line is placed through the center of the line in Figure 39 i). This can be seen, because the graph in Figure 40 i) and ii) is thinner and has fewer highs and lows compared to Figure 39 i) and ii). The load vs displacement plot displayed in Figure 40 ii) shows a displacement from 6 kN on, comparable to Figure 39 ii). A load of 6 kN is already more than half of the maximum load (11.7 kN), the sample could withstand. Therefore, it seems to be inaccurate that no elastic deformation took place before reaching 6 kN. It is assumed that no deformation was measured due to the limitations of the GCTS testing device. Figure 40 iii) shows a combination of the x-axes from Figure 40 i) and Figure 40 ii) resulting in a displacement against the time plot. The graph shows a linear increase in displacement over time. A displacement against time plot can be used to check whether the load increased linearly or not.

The data from the screenshots were not only converted into tables to plot the same data as shown in the screenshot but to get additional information from the data. To do so stress and strain were derived from the results. Stress σ_c and strain ϵ were calculated by Equation 38 and 39.

$$\sigma_c = \frac{F_c}{A} = \frac{F_c}{\pi \times r^2} \qquad \text{MPa} \qquad 38$$

$$\epsilon = \frac{\Delta l}{l} \qquad - \qquad 39$$

Where F_c is the compression load in N, r the radius of the sample in mm, Δl the displacement and l the sample length in mm. The error for σ_c is calculated in Equation 42, regarding the inaccuracies of the device. One then obtains stress-time, stress-strain and strain-time plots, as displayed in Figure 41. A stress-time plot is displayed in Figure 41 i). Young's modulus can be derived from the stress-strain graph in Figure 41 ii). In order to determine Young's modulus, the slope of the graph before the stress maximum is reached must be calculated.

$E = \frac{\Delta \sigma_c}{\Delta \epsilon}$	MPa	40

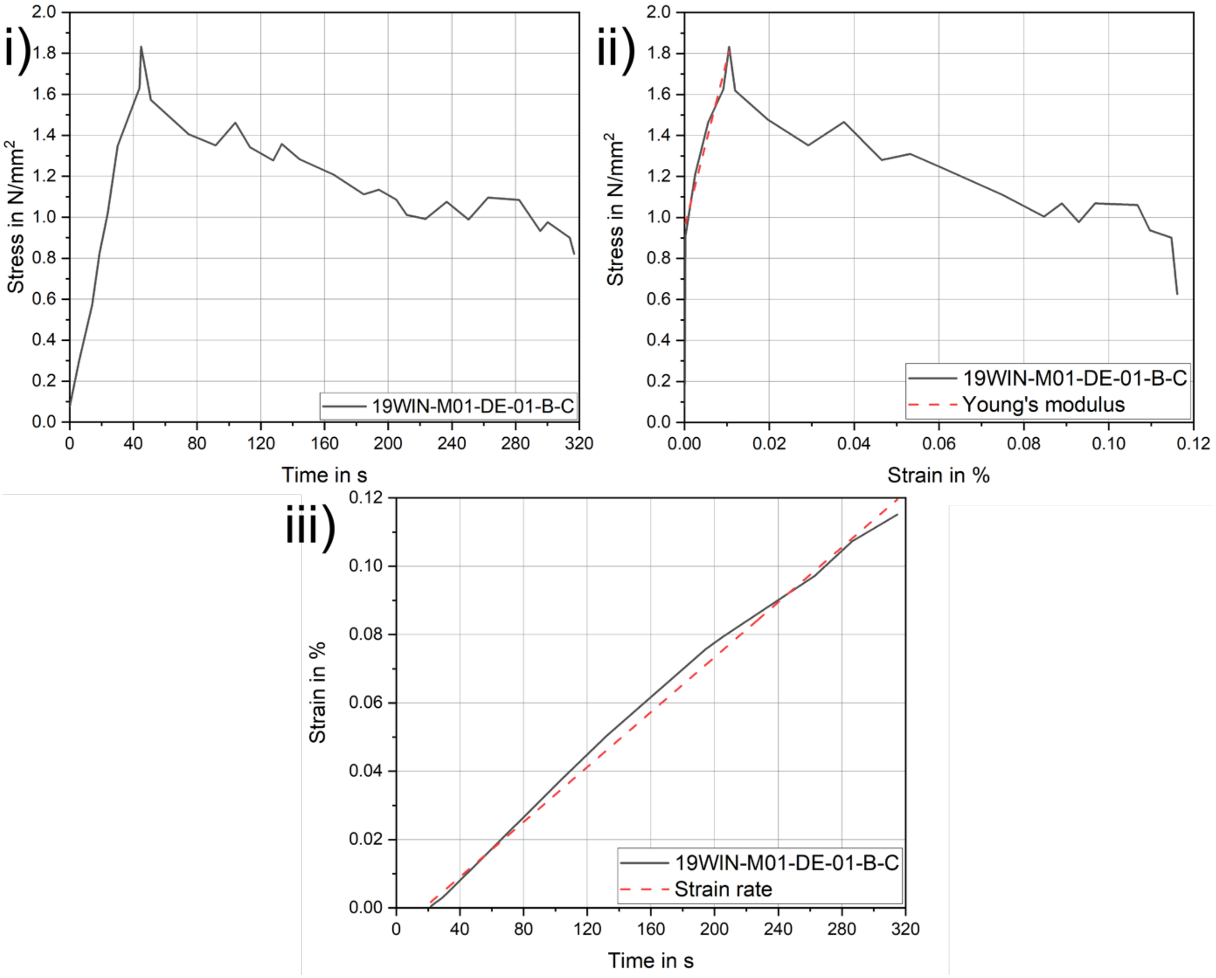

Figure 41 *For sample 19WIN-M01-DE-01-B-C. i) stress-time graph; ii) stress-strain graph; iii) strain-time graph.*

The slope of the graph, or Young's modulus in Figure 41 ii) is calculated to be $E = 82\ \mathrm{N/mm^2}$ by the slope of the dashed line. The dashed line is a linear fit for the stress-strain curve between $\sigma_\mathrm{c} = 0.9\ \mathrm{N/mm^2}$ and $\sigma_\mathrm{c} = 1.8\ \mathrm{N/mm^2}$. The problem with the calculation is, that it is unclear what is happening for a compression stress lower than $0.9\ \mathrm{N/mm^2}$, as the compression device did not record a displacement beforehand. By defining Young's modulus of the sample to $82\ \mathrm{N/mm^2}$ one assumes that the behavior below $0.9\ \mathrm{N/mm^2}$ is identical to the behavior above this value. This assumption might be incorrect, but it is the only way to receive information about the elastic behavior of the ice.

The strain rate of the test is also of interest, as the mechanical behavior of ice strongly depends on the strain rate of the test, as described in Section 3.3. The strain rate can be calculated by calculating the slope of the linear curve in a strain-time curve, as shown in Figure 41 iii).

$$\dot{\epsilon} = \frac{\Delta\epsilon}{\Delta \mathrm{t}} \qquad \frac{1}{s} \qquad 41$$

As the original curve is not perfectly linear, a linear fit of the curve is calculated (dashed line). The slope of this curve is calculated to $\dot{\epsilon} = 4.0 \times 10^{-4} \frac{1}{\mathrm{s}}$. The strain rate and Young's modulus were calculated for all samples. The results are presented in Table 6. In the first column information about the core name is listed, and the second column shows the core length. In the third column, the unique name of the sample is listed, followed by the sample length l in the fourth column. The "Position (top)" value represents the distance from the center of the sample to the top of the core. The maximum compression force F_{c} a sample could withstand is indicated in column six ("Max. force"). The strength σ_c, calculated by Equation 38, appears in column seven ("Strength"). The Young's modulus calculated by Equation 40 and the strain rate calculated by Equation 41 are presented in column eight ("Young's modulus"), and nine ("Strain rate").

Figure 42 *Two persons are lifted onto the ice for sea ice coring with help of the basket.*

Sea ice was collected at two different stations during the SCALE Winter Cruise 2019. The first station ("M01") was a pancake ice station where four different pancakes were lifted onto the ship (Figure 38). The second station ("M03") was a consolidated ice station, where people were lifted onto the ice to collect sea ice cores (Figure 42). Data from the SCALE Winter Cruise 2019 is also presented in Skatulla et al. [140].

Figure 43 *A sea ice sample inside the GCTS compression device after testing.*

***Table 6** Summary of samples tested on the SCALE Winter Cruise 2019.*

SCALE Winter Cruise 2019								
Name core	Length Core	Name sample	Length sample	Position (top)	Max. force	Strength	Young's Modulus	Strain Rate
			l	d	F_c	σ_c	E	$\dot{\epsilon}$
	m		**m**	**m**	**kN**	**MPa**	**GPa**	**s^{-1}**
M01-DE-01-A	0.210	M01-DE-01-A-C	0.135	0.13	19	2.97	-	-
M01-DE-02-A	0.290	M01-DE-02-A-C	0.135	0.13	13	2.02	0.2	5.0E-04
M01-DE-03-A	0.240	M01-DE-03-A-C	0.135	0.13	13	2.06	-	2.9E-04
M01-DE-01-B	0.355	M01-DE-01-B-C	0.135	0.13	12	1.83	-	4.0E-04
	0.355	M01-DE-01-B-D	0.135	0.26	17	2.70	-	4.5E-04
M01-DE-02-B	0.345	M01-DE-02-B-A	0.135	0.06	10	1.59	0.1	4.2E-04
M01-DE-02-B	0.345	M01-DE-02-B-B	0.135	0.19	16	2.59	0.3	3.3E-04
M01-DE-03-B	0.370	M01-DE-03-B-A	0.12	0.06	9	1.47	0.0	4.0E-04
	0.370	M01-DE-03-B-B	0.135	0.19	11	1.74	0.1	2.4E-04
M01-DE-01-C	0.420	M01-DE-01-C-C	0.135	0.17	12	1.96	0.2	5.2E-04
	0.420	M01-DE-01-C-D	0.135	0.30	16	2.48	0.2	3.7E-04
M01-DE-02-C	0.480	M01-DE-02-C-A	0.135	0.19	11	1.70	0.3	5.7E-04
	0.480	M01-DE-02-C-B	0.135	0.32	18	2.81	0.2	3.8E-04
M01-DE-03-C	0.430	M01-DE-03-C-A	0.135	0.17	15	2.33	0.1	6.0E-04
	0.430	M01-DE-03-C-B	0.135	0.30	17	2.68	0.1	5.2E-04
M01-DE-01-D	0.360	M01-DE-01-D-A	0.135	0.10	17	2.69	0.2	4.5E-04
	0.360	M01-DE-01-D-B	0.135	0.23	20	3.14	0.1	3.9E-04
M01-DE-02-D	0.285	M01-DE-02-D-A	0.135	0.10	20	3.12	0.2	4.1E-04
M01-DE-03-D	0.320	M01-DE-03-D-A	0.135	0.10	16	2.49	0.2	5.1E-04
M03-DE-01	0.770	M03-DE-01-C	0.135	0.11	28	4.38	0.3	8.1E-04
	0.770	M03-DE-01-D	0.135	0.24	22	3.49	0.3	8.1E-04
	0.770	M03-DE-01-G	0.135	0.45	23	3.56	0.4	7.5E-04
	0.770	M03-DE-01-H	0.135	0.61	27	4.19	0.4	6.7E-04
M03-DE-02	0.320	M03-DE-02-E	0.135	0.17	35	5.43	0.3	6.6E-04
M03-DE-03	0.610	M03-DE-03-C	0.135	0.13	33	5.26	-	7.1E-04
	0.610	M03-DE-03-H	0.135	0.40	23	3.59	0.2	4.8E-04
	0.610	M03-DE-03-I	0.135	0.53	19	3.03	-	4.6E-04

The strain rate results are in the range of $\dot{\epsilon} = 2.4 \times 10^{-4} \frac{1}{s}$ to $\dot{\epsilon} = 8.1 \times 10^{-4} \frac{1}{s}$. The strain rate is not constant across the samples, as the strain rate is influenced by the manual stroke of the hydraulic pump. Despite the fact that the test is conducted manually, the results are very similar. The average strain rate from Table 6 is $\dot{\epsilon} = 5 \times 10^{-4} \frac{1}{s}$, which is in the ductile-to-brittle transition zone of sea ice. Ice has its highest strength in the ductile-to-brittle transition zone as described in Section 3.6.2. Therefore, the results can be compared to most literature values. Figure 43 shows a sea ice sample after testing inside the GCTS compression device.

Figure 44 displays the strength against sample depth for the samples from the SCALE Winter Cruise 2019. In order to accomplish this, columns five and seven of Table 6 are plotted. The indicated error bars are valid for all samples in their vicinity. The error bar in depth/y-direction are half the sample length and represents the sample length. This was chosen, as the point on the y-axis indicates the center of the sample, by using the error bars the whole length of the sample is represented.

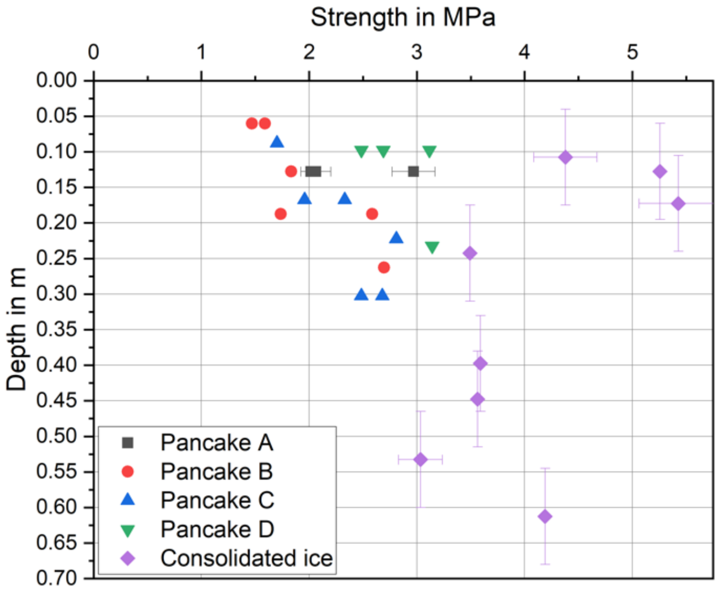

Figure 44 *Strength against depth of sea ice from the SCALE Spring Cruise 2019. Error bars in y-direction correspond to the sample length and in x-direction to an error of 8.3 %. Error bars are valid for all samples in its vicinity. The error bar in depth/y-direction are half the sample length and represents the sample length.*

The error bars in the x-direction were calculated depending on an estimated error for the force of about $\Delta F = 5\% \times F_c$ and $\Delta r = 1.5\,mm$ for the radius. The error is calculated by Equation 42

$$\Delta\sigma_c = \left(\left(\frac{\partial\sigma}{\partial F} \times \Delta F\right)^2 + \left(\frac{\partial\sigma}{\partial r} \times \Delta \mathrm{r}\right)^2\right)^{0.5} \qquad \mathrm{MPa} \qquad 42$$

resulting in an error in the strength of $\Delta\sigma_{\mathrm{c}} = 8.3\ \% \ \times \sigma_{\mathrm{c}}$, which is indicated in Figure 44. Figure 44 illustrates different trends. The size of consolidated ice cores is significantly larger than that of pancake ice cores and pancake ice is weaker than consolidated ice. A higher brine content and a higher temperature of the ice may be responsible for the weaker pancake ice, which will be investigated further. The strength of pancake ice increases with increasing depth, while consolidated ice is strongest at the top and decreases into depth. The trend is even more pronounced when combining data points from the same pancake at the same depth as done for Figure 45. The trend line indicated in Figure 45 shows the trend for the strength of pancake ice $\sigma_{\mathrm{c,pancake}}$ from the SCALE Winter Cruise 2019.

$$\sigma_{\mathrm{c,pancake}}(d) = 1.6 + 4.4 \times d \qquad \mathrm{MPa} \qquad 43$$

The equation depends on the depth d in m and gives strength σ_{c} in MPa. A simple equation based on the depth was chosen, as the sample depth can be easily determined by any researcher. Salinity and temperature measurements, which are necessary to determine the brine content of ice, which influence strength, are more difficult to determine. In addition, salinity and temperature vary depending on the time between sampling and measuring. Brine drainage depends on the core storage, temperature, and other factors. The depth on the other side will not change, even if the ice is stored in a freezer before testing the ice.

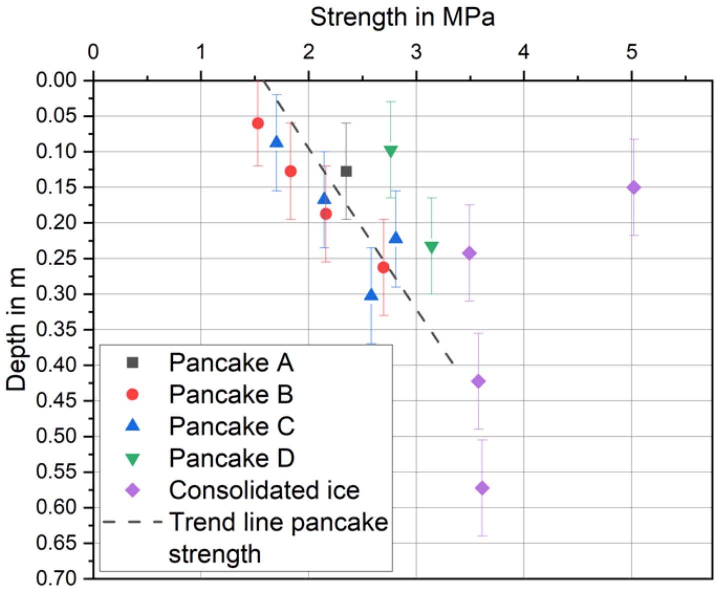

Figure 45 *Samples from the same station and similar depth are combined to one data point. Trend line for pancake ice of the SCALE Winter Cruise 2019. The error bar in depth/y-direction are half the sample length and represents the sample length.*

Temperature and salinity measurements were performed. The physical data is available via a publicly accessible data repository [141]. The data is displayed in Figure 46. The colored data points connected with a line represent the average salinity and temperature of the pancake or consolidated ice. The white-filled symbols with small lines inside represent the individual measurements. Data points with the same shape belong to the same pancake or consolidated ice, and data points with the same shape and same filling belong to the same sea ice core.

The temperature plot (Figure 46 i)) contains three types of graphs. Consolidated ice has the lowest temperature at the surface as it is not in contact with the water and only in contact with the atmosphere. The temperature profiles from Pancakes A, B, and D show a lower temperature at the top than at the bottom. However, the difference is not as large as for the consolidated ice. Pancake C has a nearly constant temperature over the whole thickness, which can be explained by a turnover of the floe recently before sampling. All samples show nearly the same temperature at the bottom, where the ice is always in contact with the ocean. [140]

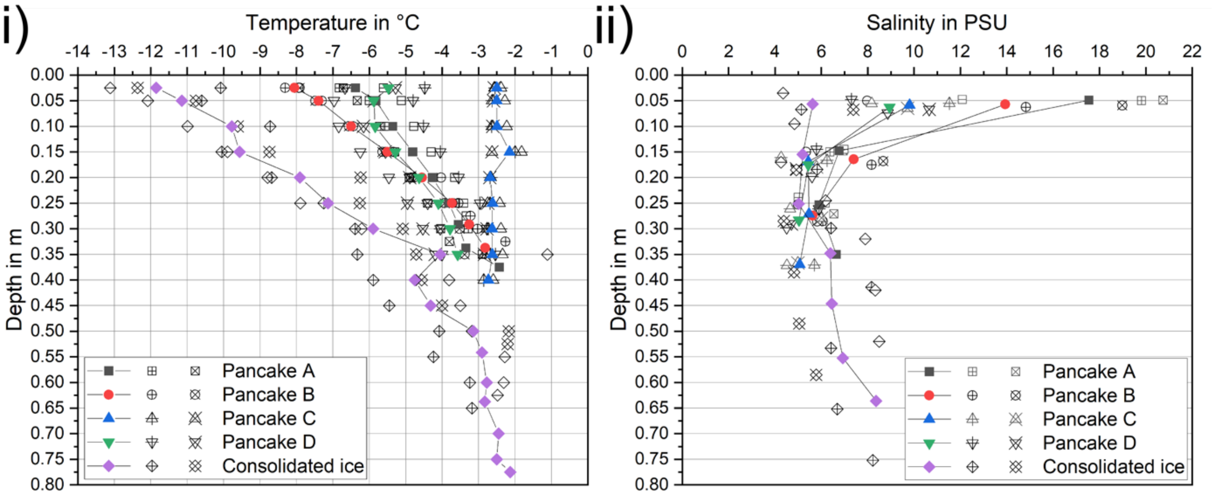

Figure 46 *Results of the physical measurements. i) Temperature against depth; ii) Salinity against depth. The colored points connected with a line display the average salinity/ temperature. The white filled data points display the individual measurements. The physical data is available via a publicly accessible data repository* [141].

The brine volume can be derived from the temperature and salinity plots in Figure 46, with the help of Equation 14 (Section 3.4.1). The temperature and salinity values need to be related to each other, as they were not measured at the same point. First of all, the temperature measured during sampling (Figure 46 i)) is fitted to a linear equation for each pancake and the consolidated ice separately. This results in Equations 44, 45, 46, 47, and 48 of temperature over depth. Then, with the help of the five equations, the temperature is determined for each salinity measurement. Knowing the temperature and salinity of the ice, the brine volume during sampling can be calculated, it is displayed in Figure 47 i).

$$\mathrm{T}_{\text{Pancake A,Winter}} = -6.5 + 10.3 \times d \qquad °\mathrm{C} \qquad 44$$

$$\mathrm{T}_{\text{Pancake B,Winter}} = -8.3 + 17.3 \times d \qquad °\mathrm{C} \qquad 45$$

$$\mathrm{T}_{\text{Pancake C,Winter}} = -2.1 - 2.3 \times d \qquad °\mathrm{C} \qquad 46$$

$$\mathrm{T}_{\text{Pancake D,Winter}} = -6.3 + 8.2 \times d \qquad °\mathrm{C} \qquad 47$$

$$\mathrm{T}_{\text{Consolidated,Winter}} = -11.1 + 14.8 \times d \qquad °\mathrm{C} \qquad 48$$

Besides that, the brine volume is also calculated for the testing temperature of -10 °C instead of the sampling temperature. The brine content for a temperature of -10 °C is displayed in Figure 47 ii).

Comparing Figure 47 i) and ii) it becomes apparent that the temperature has a major influence on the brine content of sea ice. The data points scatter more if the sampling temperature is used to calculate the brine content. If the temperature is constant, the brine volume graph has a similar shape as the salinity graph (Figure 46 ii)).

For the comparison of strength, the brine volume at -10 °C is used, as this is the temperature at which the sea ice is stored and tested on the SA Agulhas II and thus represents the conditions inside the ice more accurately during the test.

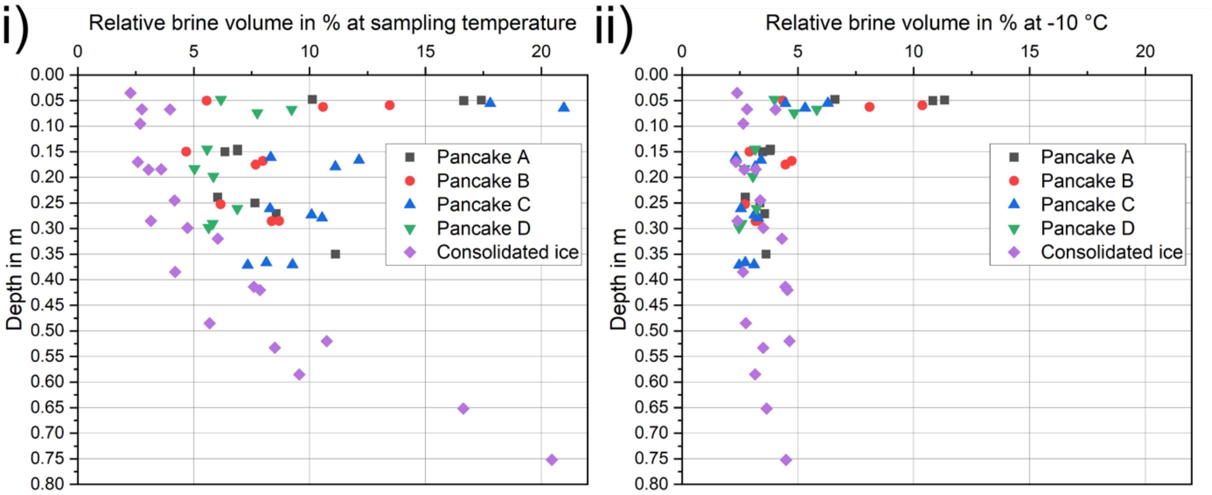

Figure 47 *Brine volume of the ice i) at sampling temperature and ii) at testing temperature -10 °C.*

A linear equation is derived for the brine and depth data presented in Figure 47 ii), separately for pancake ice ($\frac{V_b}{V}_{Pancake}$) and consolidated ice ($\frac{V_b}{V}_{Consolidated}$). The equation gives the relative brine volume dependent on the depth and allows the calculation of the brine volume for the strength samples in Table 6. As a result, the “Position (top)” d in m is used and the brine volume is calculated

$$\frac{V_b}{V}_{Pancake,Winter} = 6.9 - 14.2 \times d \qquad \% \qquad 49$$

$$\frac{V_b}{V}_{Consolidated,Winter} = 2.3 + 3.3 \times d \qquad \%. \qquad 50$$

Figure 48 displays the compressive strength of pancake ice and consolidated ice against the relative brine volume from the SCALE Winter Cruise 2019. It also displays the estimated compressive strength for a strain rate of $\dot{\epsilon} = 5 \times 10^{-4}\,\frac{1}{s}$ after Kovacs [142]. The equation by Kovacs is developed to predict the unconfined uniaxial compressive strength of sea ice floes depending on the strain rate and brine volume. The equation by Kovacs [142] was developed by data fitting.

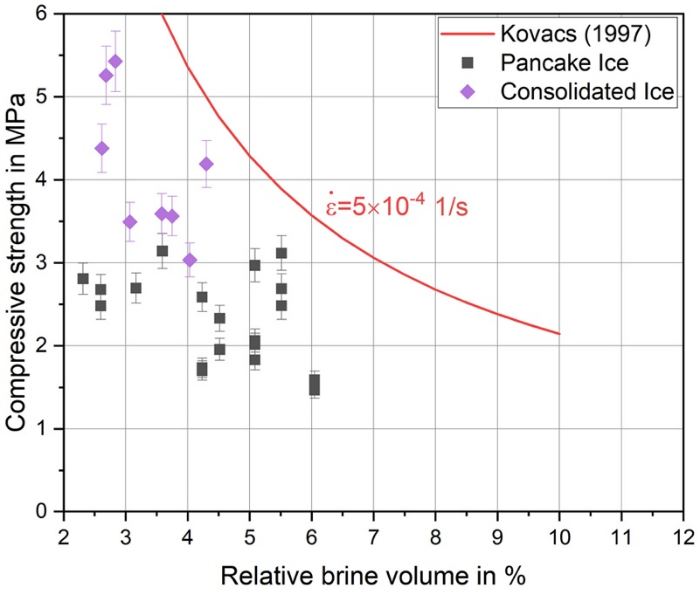

Figure 48 *Compressive strength depending on the brine volume. The red line displays the equation by Kovacs* [142] *to determine the strength depending on the brine volume. Error bars are valid for all data points in their vicinity.*

The calculated compressive strength after Kovacs [142] is higher than the measured compressive strength for pancake ice and consolidated ice. Nevertheless, the measured sea ice compressive strength shows a decrease in strength, like the equation by Kovacs [142].

5.1.2 Compressive strength: SCALE Spring Cruise 2019

Compressive strength tests on the SCALE Spring Cruise 2019 were conducted comparable to the tests on the SCALE Winter Cruise 2019 presented in Section 5.1.1. The GCTS compression device (Section 4.1.1.3) was used for mechanical sea ice testing. In total 62 samples from 20 sea ice cores were used for strength testing. The results of the tests are listed in Table S 1. Cores at MIZ2, MIZ3, MIZ6, and MIZ7 were collected from consolidated ice, while MIZ8 and MIZ9 were collected from sea ice floes. Sea ice floes during the SCALE Spring Cruise 2019 differ fundamentally from the floes collected during the SCALE Winter Cruise 2019, as the floes collected during the spring cruise most probably originated from melting consolidated ice fields. On the other side, ice floes from the winter cruise are assumed to originate from growing smaller pancake ice floes. Young's modulus is missing for most sea ice samples, as the GCTS compression device did not measure any displacement before the maximum stress of the sample was reached. Therefore, it was not possible to calculate the slope of the stress-strain curve. Young's modulus values for samples where a stress-strain curve could be analyzed are much lower than 5.8 GPa [143] and 4 GPa to 6 GPa [144] from literature. Results presented for the SCALE Spring Cruise 2019 are published by Paul et al. [145].

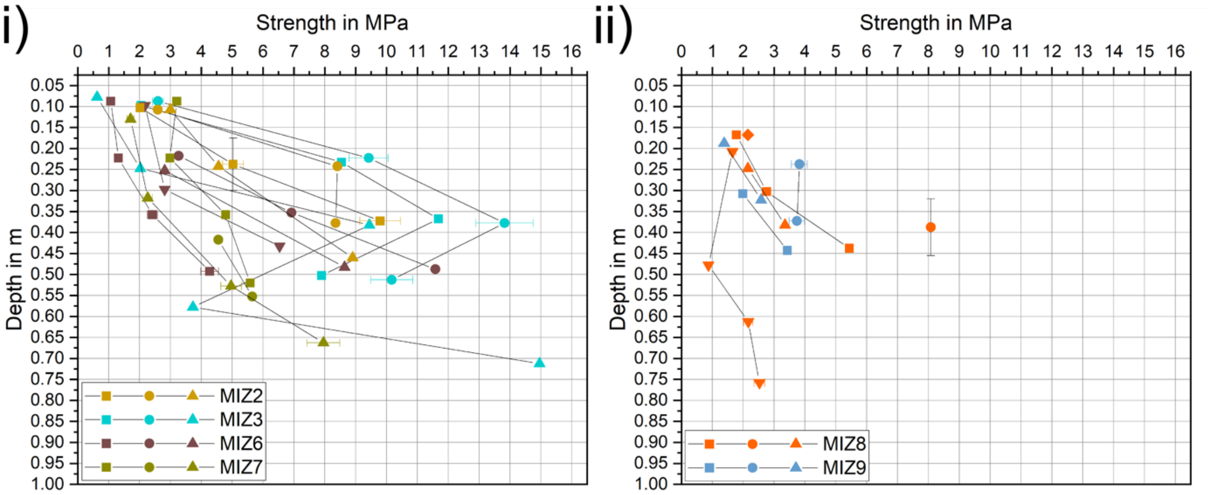

Figure 49 *Strength of sea ice samples over depth. Connected dots represent results within one ice core at different depths. i) Consolidated ice samples; ii) Ice floe samples. Error bars are valid for all data points in their vicinity. The error bar in depth/y-direction are half the sample length and represents the sample length.*

Figure 49 shows the compressive strength results separately for i) consolidated ice and ii) ice floes. Samples from MIZ2, MIZ6, and MIZ7 show an increase in strength over the core length.

On the other side, the ice cores from MIZ3 show an increase until $d = 0.4\ \mathrm{m}$, similar to MIZ2, MIZ6, and MIZ7, but followed by a decrease in strength until 0.6 m. One sample from MIZ3 originated from a depth below 0.6 m and showed an increase in strength further down. Samples originating from ice floes presented in Figure 49 ii) show very different behavior. The uppermost sample per core from ice floes, which could be tested, is from a deeper depth compared to the samples from consolidated ice. This is because the ice cores were already perforated with large holes at the top layer. Besides that, the overall strength for samples from ice floes is lower compared to consolidated ice. The cores do not show a distinctive strength increase as the cores from consolidated ice. Even though, the strength was significantly lower for ice floes, they could still have a high length, as, for example, MIZ8-DE-01-B is 0.84 m.

The average strength at each station is displayed in Figure 50. Compressive strength from the same station and same height is combined into one measurement point to highlight the strength development at each station. The compressive strength at the top was the same for all stations. It is not possible to predict the ice strength in a lower layer just by knowing the strength at the top. A trendline for the consolidated ice from the SCALE Spring Cruise 2019 is shown in Figure 50 and Equation 51 (d in m).

$$\sigma_{\mathrm{c,consolidated,spring}} = 0.8 + 15.4 \times d \qquad \mathrm{MPa} \qquad 51$$

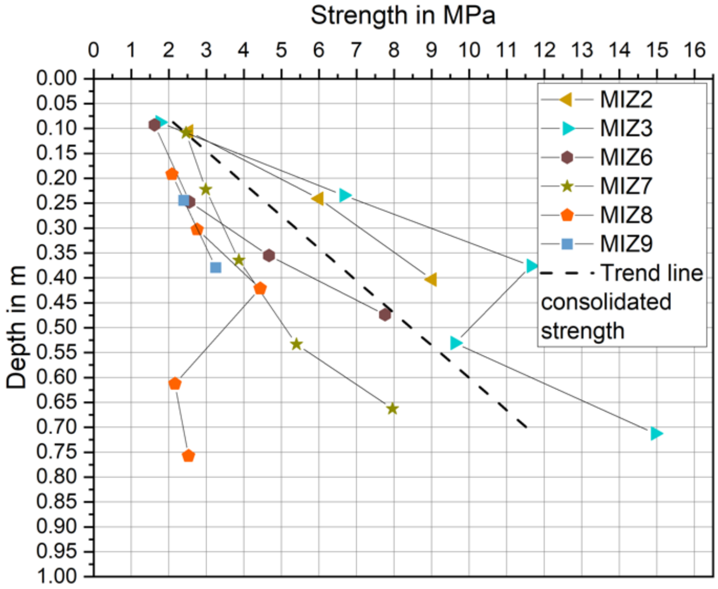

Figure 50 *Average strength over depth per station. Samples from the same depth are combined to one point. The trend line indicates the strength of consolidated ice.*

Physical data for the SCALE Spring Cruise 2019 is available via a publicly accessible data repository [146]. The average temperature and salinity of the different stations are displayed in Figure 51. The temperature decreases linearly from below – 3 °C for MIZ2 and MIZ3, while the temperature at the top is one degree warmer at MIZ6 and MIZ7 and decreases linearly until approximately – 1.9 °C which is the freezing point for sea water with 35 PSU (Equation 27). The temperature for the cores from ice floes (MIZ8 and MIZ9) was constant over the cores at around – 1.5°C. The floes did not melt entirely beforehand as the salinity of the ice floes is constant at about 4 PSU, resulting in a freezing point temperature of – 0.22 °C (Equation 27). Therefore, the ice could be warmer than the sea water and still not melt. The salinity for MIZ2, MIZ3, and MIZ6 is high at the top and decreases until the ice touches the sea water. The cores from MIZ7 show a c-shaped curve for the salinity profile.

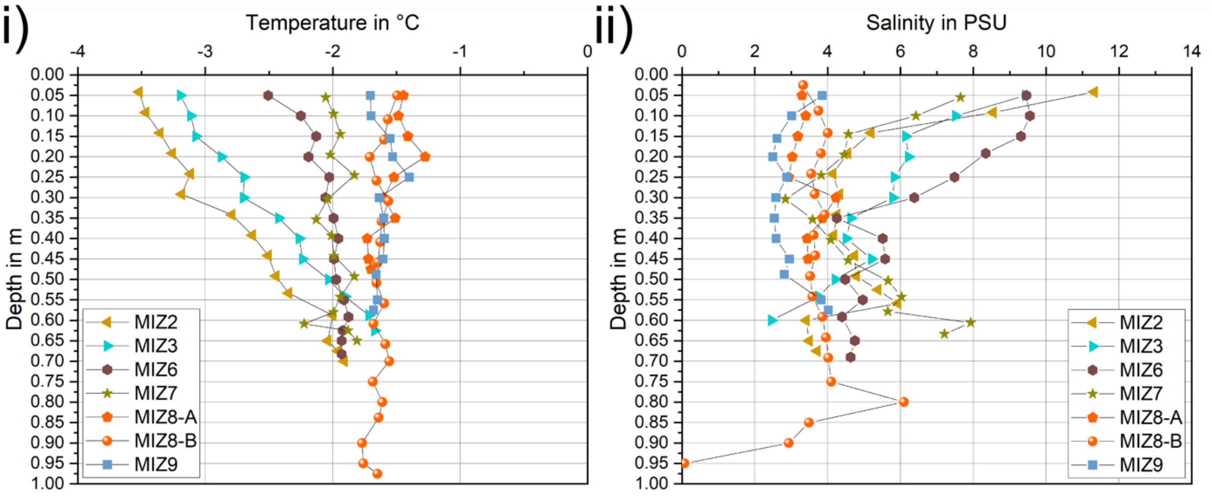

Figure 51 *Physical data from the SCALE Spring Cruise 2019. Average i) temperature and ii) salinity for the different stations. The physical data is available via a publicly accessible data repository* [146].

Combining the physical data from [146], displayed in Figure 51, result in the relative brine content displayed in Figure 52. Figure 52 i) shows the relative brine content in % over sea ice depth at sampling temperature, and Figure 52 ii) gives the relative brine content in % over sea ice depth at -10 °C. The brine content is calculated with the help of Equation 14. Parameters influencing the brine content are temperature and salinity. If the temperature is lowered from sampling to testing, the brine content decreases because more brine solidifies. Because the testing temperature of the ice is constant at -10 °C, the brine content presented in Figure 52

ii) is used to calculate a linear equation to predict the brine content for the compressive strength samples.

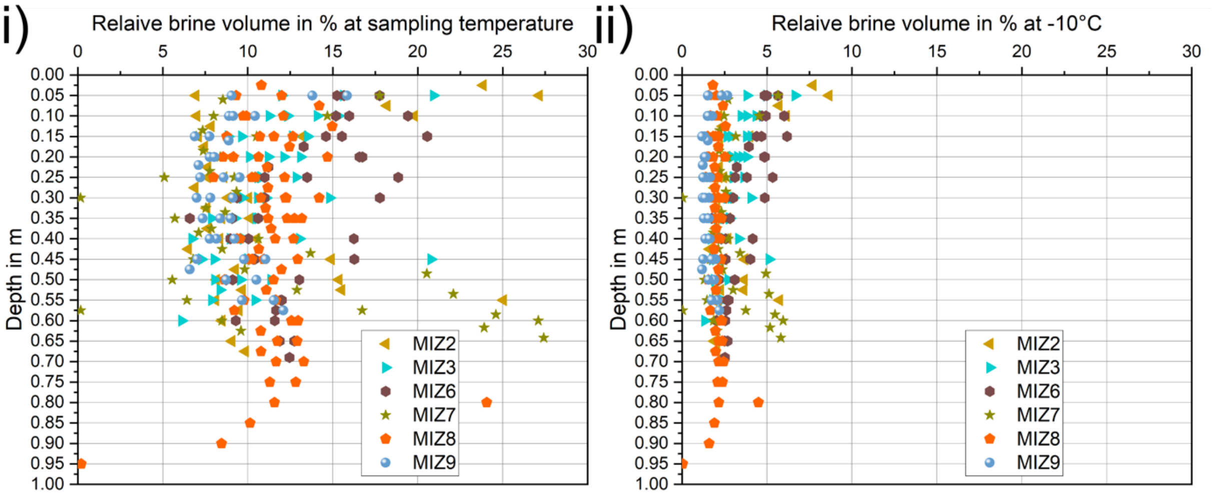

Figure 52 *Relative brine content at i) sampling temperature and at ii) -10 °C.*

The equation for the brine content in consolidated ice is shown in Equation 52 and for ice floe stations in Equation 53. The corresponding brine content (d in m) is calculated for the strength results

$$\frac{V_b}{V}_{Consolidated,Spring} = 4.1 - 3.1 \times d \qquad \% \qquad 52$$

$$\frac{V_b}{V}_{Floes,Spring} = 1.7 + 0.3 \times d \qquad \%. \qquad 53$$

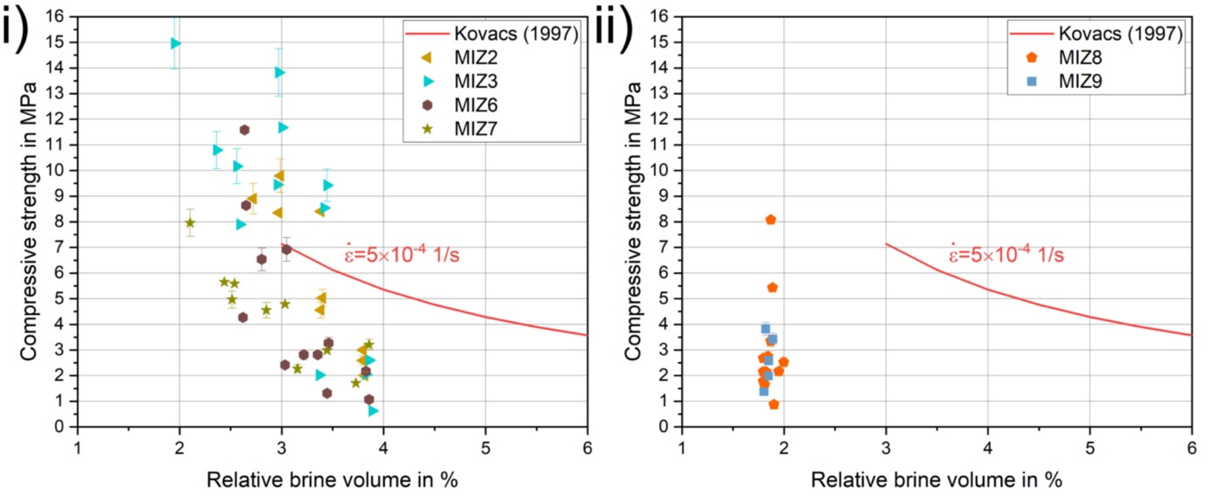

Figure 53 *Compressive strength in dependence of the relative brine volume at -10 °C for i) consolidated and ii) ice floes. The red line displays the equation by Kovacs* [142] *to determine the strength depending on the brine volume. Error bars are valid for all data points in their vicinity.*

Figure 53 shows the compressive strength and brine content for i) consolidated ice and ii) ice floes. The red line shows the equation developed by Kovacs [142] for first-year sea ice floes. The equation by Kovacs [142] is valid for $2.5\ \% \leq \frac{V_\mathrm{b}}{V} \leq 8.0\ \%$. But some brine volumes for the consolidated ice and all brine volumes for the ice floes were lower than 2.5 %, caused by the low testing temperature of the sample.

The uniaxial compressive strength for consolidated ice (Figure 53 i)) decreases with increasing porosity as indicated by the Kovacs equation [142], but the compressive strength is higher for low brine volumes and lower for higher brine volumes than suggested by the Kovacs equation [142]. The strength differences could be explained by different densities in the Arctic and Antarctic as well as by a different sea ice texture. Density and texture were not investigated for the SCALE Spring Cruise 2019. The brine volume for sea ice floes at -10 °C is nearly constant between 1.8 % and 2.0 %, which is below the domain of the Kovacs equation [142]. The low variance of the brine values does not allow any conclusion to be drawn from the impact of brine on the compressive strength of ice floes.

5.1.3 Compressive strength: SCALE Winter Cruise 2022

Different from the SCALE Winter Cruise and Spring Cruise 2019 where no changes were made in the testing procedure in between the cruises, the test setup and procedure were changed drastically for the SCALE Winter Cruise 2022. The only reason, why no changes were made between the cruises in 2019 was because time was very limited. For the SCALE Winter Cruise 2019, a custom-designed uniaxial compression device (Section 4.1.1.4) was used to overcome the disadvantages of the GCTS compression device (Section 4.1.1.3). The most significant advantage, as mentioned previously, is that the custom-designed compression device allows the data to be saved immediately to file rather than having to be screenshotted. Besides changing the device, the testing procedure was changed to larger samples, and the weight of each sample was measured as explained in Section 4.1.1.2. In total 14 cores resulting in 25 compression samples were collected for the uniaxial compression test on the SCALE Winter Cruise 2022. The results are reported in Table S 2.

A stress-strain graph obtained from the custom-designed uniaxial compression device is displayed in Figure 54. The figure shows three different data sets. The black and white data sets originate from the two displacement sensors on the compression device. The red and green data points are the average displacement of displacement sensor one and displacement sensor two, respectively. Due to the fact that the device is manually operated by a hand pump, the data sets do not show a steady increase but rather a oscillating pattern. The stress increases when the hand pump is moved down and decreases when the hand pump is moved up due to stress/ strain release within the sample. In order to reduce fluctuations in the data, five data points are combined into one prior to plotting the data and conducting further analysis.

Young’s modulus was calculated within the middle third of stress, marked by two black horizontal lines. Every stress increase lying in between the two black horizontal lines is marked with green data points. Young’s modulus is determined for these stress increases. For Figure 54 three different values (E_1=1.5 GPa; E_2=1.7 GPa; E_3=1.3 GPa) are calculated. The average of these values (E_{avg}=1.5 GPa) is used as Young's modulus of the sample. Young’s modulus is calculated for the middle third as at the beginning and end of the test nonlinear behavior of the ice could occur. The strain rate is also calculated for the middle third of the stress increase. Although the compression test was manually driven, the strain rate of $5 \times 10^{-4} \frac{1}{\mathrm{s}}$ was kept constant over all samples.

It must be noted, that (sea) ice behavior under compression depends on the strain rate, as the ice creeps under load (Section 3.3.1). The lower the strain rate, the more creep takes place during the test and vice versa. Therefore, the term Young’s modulus may be misleading in this context, as it is not a fixed value independent of the loading history, but depends on the strain rate of the test. The Young’s modulus noted in Table S 2 and further analyzed in this section is only valid for the corresponding strain rate of the test.

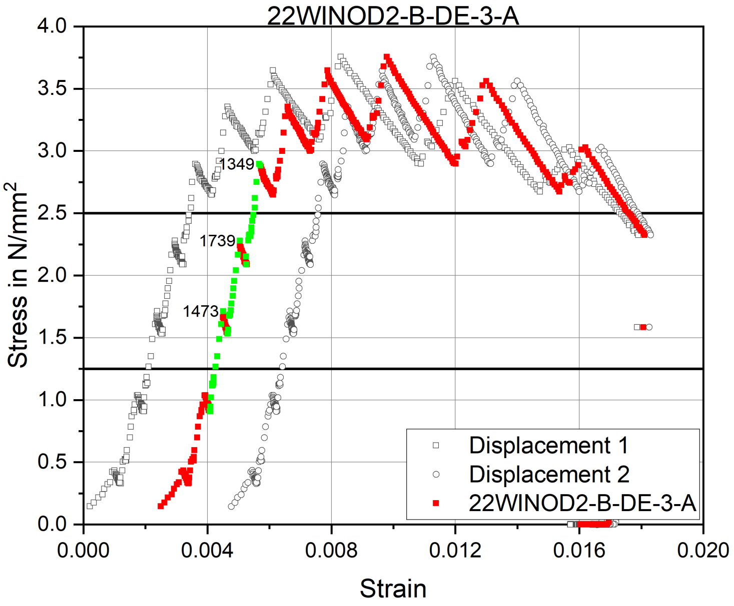

Figure 54 *The plot shows the recorded data for displacement sensor 1, displacement sensor 2, and the average displacement of both from the custom-designed compression device. The two black horizontal lines mark 1/3 and 2/3 of the maximum stress of 3.75 N/mm2. Young's modulus was calculated for the data in the middle third (green data points).*

The resultant maximum strength and Young's moduli for all samples tested on the SCALE Winter Cruise 2022 depending on the sample depth are displayed in Figure 55. Data points from the same core are connected via a line. The error in maximum strength (Equation 42) of 6.7 % is calculated by assuming a 1.5 mm error in the sample radius and 0.5 % in the load cell reading, which is better than the error calculation for the GCTS compression device.

No trend is apparent in whether the strength increases or decreases with increasing sample depth. The strength appears relatively constant over the depth. Only OD4-DE-2 varies more than 2 MPa over the core depth. No trend for Young's modulus over sea ice depth is apparent in Figure 55 ii). Only OD3-D-DE-2 and OD4-DE-2 vary more than 0.5 GPa over the core length. For the other cores presented in Figure 55 ii) Young's modulus is constant.

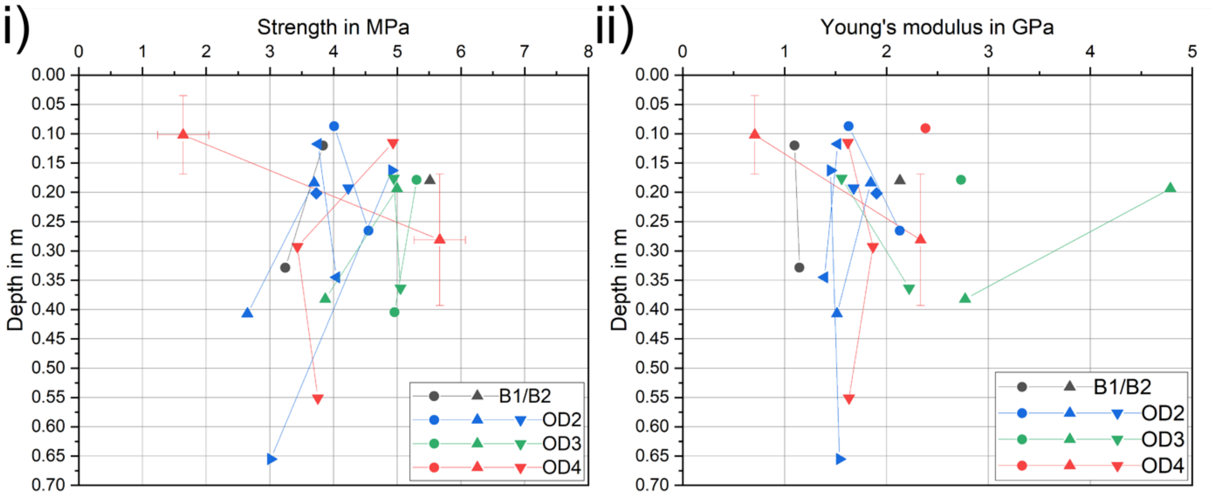

Figure 55 *i) Strength and ii) Young's modulus of sea ice samples over depth. Connected dots represent results within one ice core at different depths. Error bars are displayed for one large and one small sample from OD4. The error bar in depth/y-direction are half the sample length and represents the sample length.*

Different from the cruises in 2019, the weight of each compression sample was measured, and the corresponding density was calculated. Figure 56 displays i) strength and ii) Young's modulus depending on the density. The figure shows that the strength increases with increasing density. The maximum strength is 5.7 MPa and the minimum is 1.6 MPa, the average strength is calculated to be 4.2 MPa. A trend line was calculated for OD2, OD3, and OD4 and is plotted in Figure 56 i). The trend line $\sigma(\rho)$ in MPa (Equation 54) gives the compressive strength depending on the density ρ in $\frac{\mathrm{kg}}{\mathrm{m}^3}$.

$$\sigma(\rho) = -8 + 0.015 \times \rho \qquad \mathrm{MPa} \qquad 54$$

A linear increase in strength with decreasing porosity has already been reported by Han [122] for Arctic summer ice. A logarithmic decrease of the vertical compressive strength of Arctic sea ice with increasing density was found by Moslet [49].

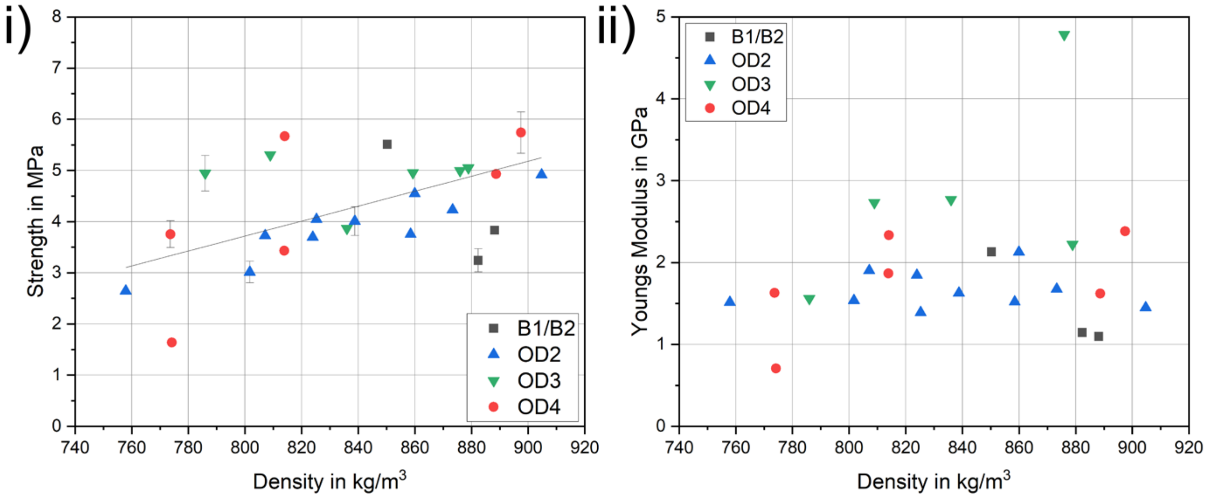

Figure 56 *i) Strength and ii) Young's modulus of sea ice samples against density. The indicated error bars are valid for all samples in its vicinity.*

Young's modulus against density is displayed in Figure 56 ii). The data points lie between 0.7 GPa and 4.8 GPa. The average Young's modulus is 1.8 GPa. Young's modulus appears constant with varying density.

Density allows to draw conclusions on the total porosity of samples, while salinity and temperature only give information about the brine content of the ice. Nevertheless, the brine volume is also calculated for the samples to better compare the results to the 2019 cruises. Figure 57 displays i) temperature and ii) salinity of the samples from the SCALE Winter Cruise 2022. The bottom temperature for all samples is around – 2 °C, comparable to the results of previous SCALE cruises. Salinity results (Figure 57 ii)) for B1/B2, OD3, and OD4 show a "c" – curved shape until a depth of 0.3 m. Below 0.3 m, the curves for OD2 and OD4 overlap.

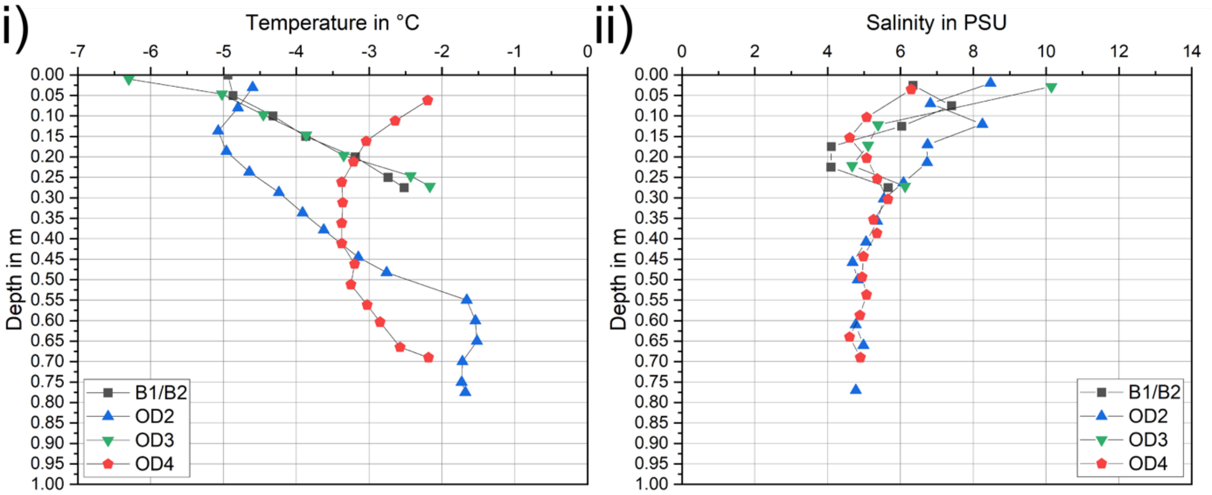

Figure 57 *Physical data from the SCALE Winter Cruise 2022. Average i) temperature and ii) salinity for the different stations. The physical data will be made available via a publicly accessible data repository.*

The brine content of the ice is presented in Figure 58 for the brine content i) during sampling and ii) during the test at – 10 °C. For the analysis of the strength, the brine content during the test is used.

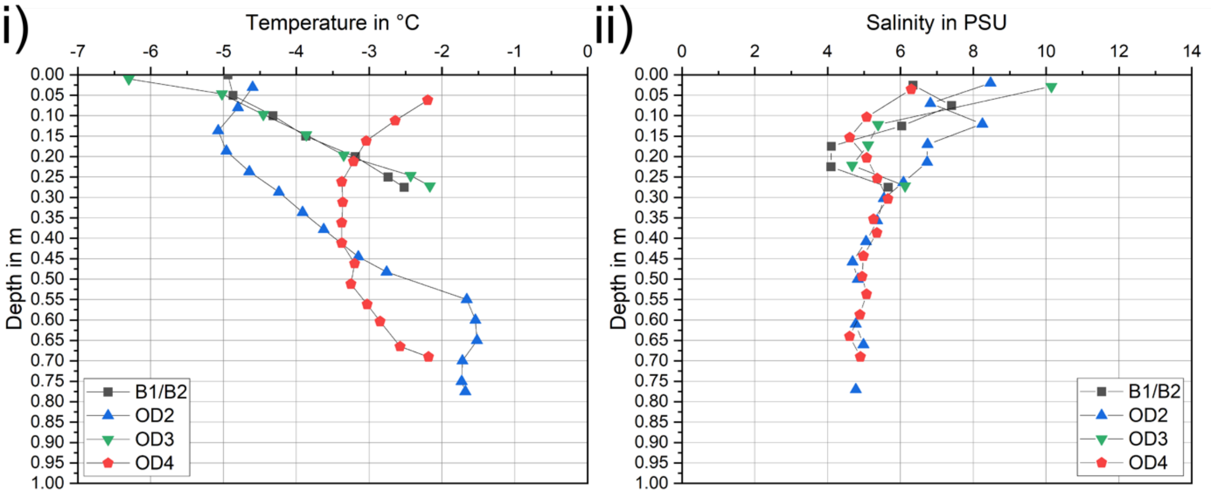

Figure 58 *Relative brine content at i) sampling temperature and at ii) - 10 °C for the SCALE Winter Cruise 2022.*

Equation 55 predicts the relative brine content of the ice at – 10 °C depending on the ice depth. The equation is calculated by fitting a linear curve through the data points in Figure 58.

$$\frac{V_b}{V}_{Winter22} = 3.7 - 1.8 \times d \qquad \% \qquad 55$$

The compressive strength against relative brine volume for the SCALE Winter Cruise 2022 is displayed in Figure 59. The relative brine content is similar at all four stations, so it is not possible to describe a trend for compressive strength based on brine content.

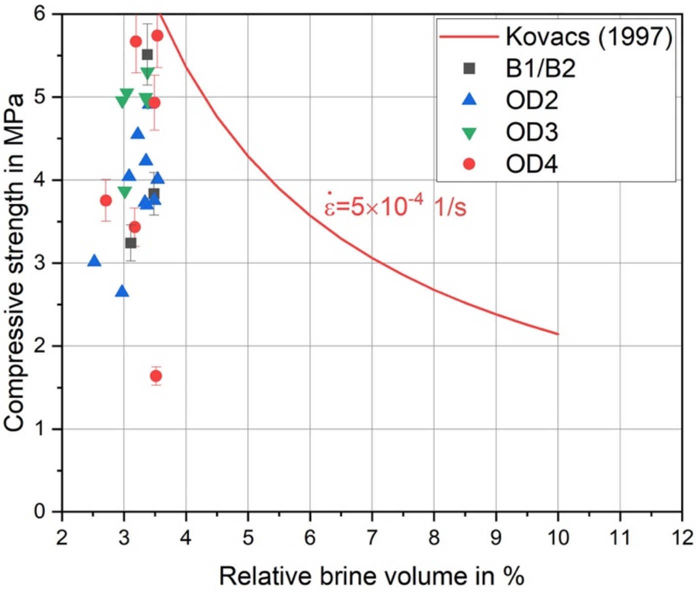

Figure 59 *Compressive strength in dependence of the relative brine volume at - 10 °C for samples from the SCALE 2022 Winter Cruise. The red line displays the equation by Kovacs* [142] *to determine the strength depending on the brine volume. Error bars are valid for all data points in their vicinity.*

When comparing Figure 56 and Figure 59, one comes to the conclusion that the density might be a better parameter to evaluate the strength than the brine content. The differences in the density are much more pronounced than in the brine content. However, since the density was not determined during all three cruises, the brine content will be used to compare the results of the different cruises with each other.

5.1.4 Differences and similarities between SCALE Cruises in 2019 and 2022

115 sea ice samples were tested under compression during the SCALE Winter and Spring Cruise 2019 as well as the SCALE Winter Cruise 2022. Two different compression devices were used to accomplish this. To compare the samples among each other, the depth from the top of the ice of each sample was recorded and the brine content at the testing temperature of -10 °C was calculated. The density was only measured for samples from the SCALE Winter Cruise 2022, and thus cannot be compared across cruises. While comparing the three cruises it has to be pointed out that the sample length increased for samples tested on the SCALE Winter Cruise 2022.

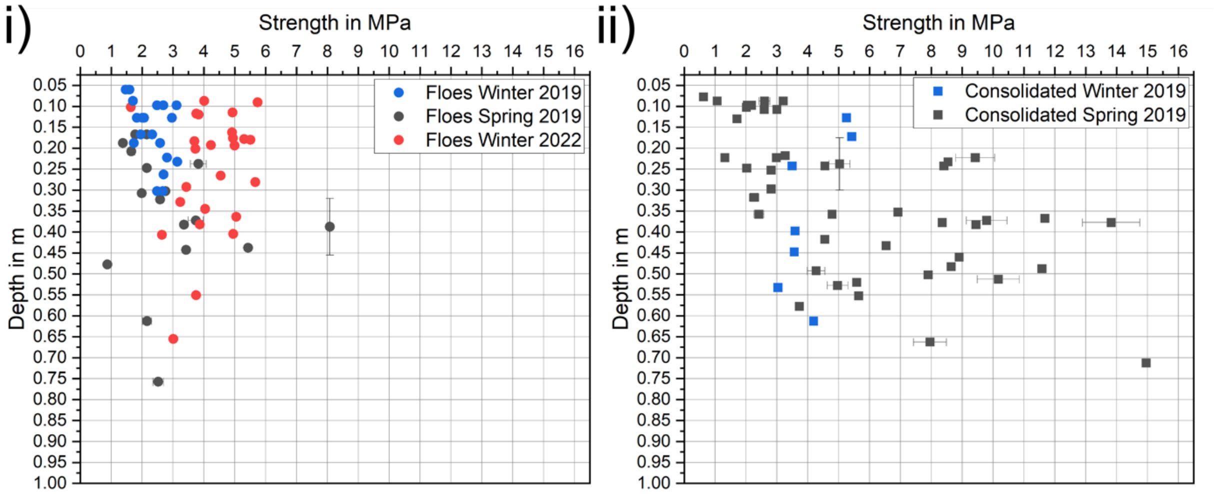

Figure 60 *Strength of all sea ice samples over depth for i) ice floes and ii) consolidated ice. Error bars are valid for all data points in their vicinity. The error bar in depth/y-direction are half the sample length and represents the sample length.*

Strength over depth results of all three cruises are presented in Figure 60 separately for i) ice floes and ii) consolidated ice. Floes tested during the SCALE Winter Cruise 2019 originate from a lower depth ($d \leq 0.3\ m$) compared to the other two cruises, where samples also originate from a larger depth of up to 0.75 m. Samples from the SCALE Winter Cruise 2019 are also the weakest samples. Most samples, except for two samples, from the SCALE Winter Cruise 2022 are stronger than the strongest sample from the SCALE Winter Cruise 2019. Nevertheless, the overall strongest sample was measured on the SCALE Spring Cruise 2019. Except for one sample, all other samples showed a strength below 6 MPa. The average compressive strength for winter floes from 2019 is $\sigma_c = 2.3 \pm 0.5\ \mathrm{MPa}$, from 2022 is $\sigma_c = 4.1 \pm 1.2\ \mathrm{MPa}$, and from spring 2019 is $\sigma_c = 2.9 \pm 1.6$ MPa. It is assumed that ice floes obtained during winter were actually pancake ice floes growing according to the pancake ice cycle (Figure 11), while the ice floes obtained during spring were broken pieces of previously consolidated ice fields. This assumption is supported by the physical data presented in Figure 51 for the ice floes. The temperature is higher, and the salinity is lower compared to floes collected in the winter. Very young ice has the highest salinity and older ice has a lower salinity. The high temperature within the spring cores indicates the melting process within the ice, besides the lower strength compared to consolidated ice from the SCALE Spring cruise 2019 ($\sigma_c = 5.8 \pm 3.7$ MPa).

Results of the compression strength of consolidated ice (Figure 60 ii)) show a broader distribution than the ice floe results. The lowest strength for consolidated ice is lower than the lowest strength for pancake ice and the highest consolidated strength is nearly two times higher than the highest ice floe strength.

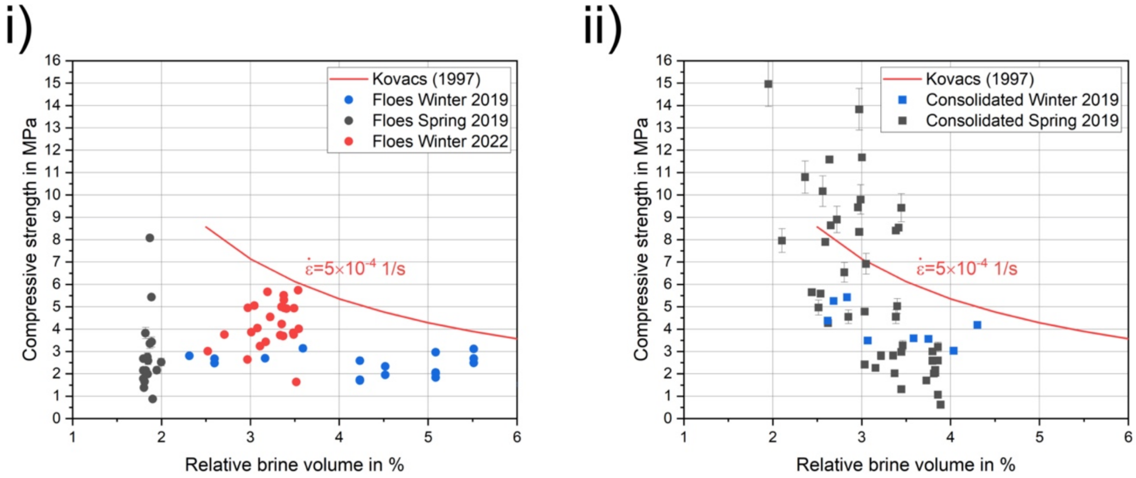

***Figure 61** Relative brine content of sea ice from all three cruises against the compressive strength for i) ice floes and ii) consolidated ice.*

The relative brine content of sea ice samples against strength are displayed in Figure 61 for i) ice floes and ii) consolidated ice together with the Kovacs equation [142]. All strength results measured during the three cruises are lower than indicated by the Kovacs equation [142], even though this equation is derived for first-year ice floes. The ice collected in winter has a higher brine content than the ice collected in spring. This supports the assumption that the ice floes obtained in spring originate from broken consolidated ice fields, because older ice has a lower salinity than newly formed ice.

Compressive strength results for consolidated ice show higher and lower results than the Kovacs equation [142], but the results do not follow the trend by the Kovacs equation. Due to sampling limitations in winter, most consolidated ice was collected in winter for this study. Concluding, the compressive strength of consolidated ice has a broader distribution than ice floes and consolidated ice is in general stronger ($\sigma_\mathrm{c} = 5.4\ \mathrm{MPa}$) than ice floes ($\sigma_\mathrm{c}\ =\ 3.2\ \mathrm{MPa}$). The higher strength of consolidated ice is caused by a lower brine content in the ice and a different ice texture. Consolidated ice has a columnar texture at the bottom of the ice, which is in general stronger under compression compared to granular ice texture [140]. Granular ice texture is dominant in pancake ice floes. Consolidated ice can have a strength up to two times the strength of ice floes. The strength of Antarctic ice floes is lower than Arctic ice floes. For ice from the Winter Cruise 2022 it is shown that the strength of sea ice decreases with decreasing density, but the Young's modulus is unaffected by the density.

5.2 Rheological tests

Rheological tests of new ice were performed during the SCALE Winter Cruise 2019 and SCALE Winter Cruise 2022. It was also tried to perform tests during the SCALE Spring Cruise 2019, but due to the absence of new ice, sampling was not possible.

According to the World Meteorological Organization [147] young ice can be separated into frazil ice, grease ice, slush, and shuga. Frazil ice is, as explained in Section 3.5.1, the first ice crystals forming in the Antarctic marginal ice zone. Grease ice appears if the environmental conditions are calm and the frazil ice crystals agglomerate at the ocean's surface. If snow falls on top of the grey grease ice layer it is termed slush. Sub-zero temperatures, waves, and wind action lead to the growth of small pancake ice floes called shuga. The aim of this study was to focus on the rheological properties of frazil ice, but it was found to be difficult to distinguish between the different forms of new ice. As all kinds of new ice originate from frazil ice and frazil ice crystals are present at each stage of the new ice, the term frazil ice will be used in this study for all kinds of new ice.

In total 27 samples of frazil ice were tested during the SCALE Winter Cruise 2019 and 2022 following the procedure described in Section 4.1.2. First, the results from the two cruises are presented separately followed by a comparison between them.

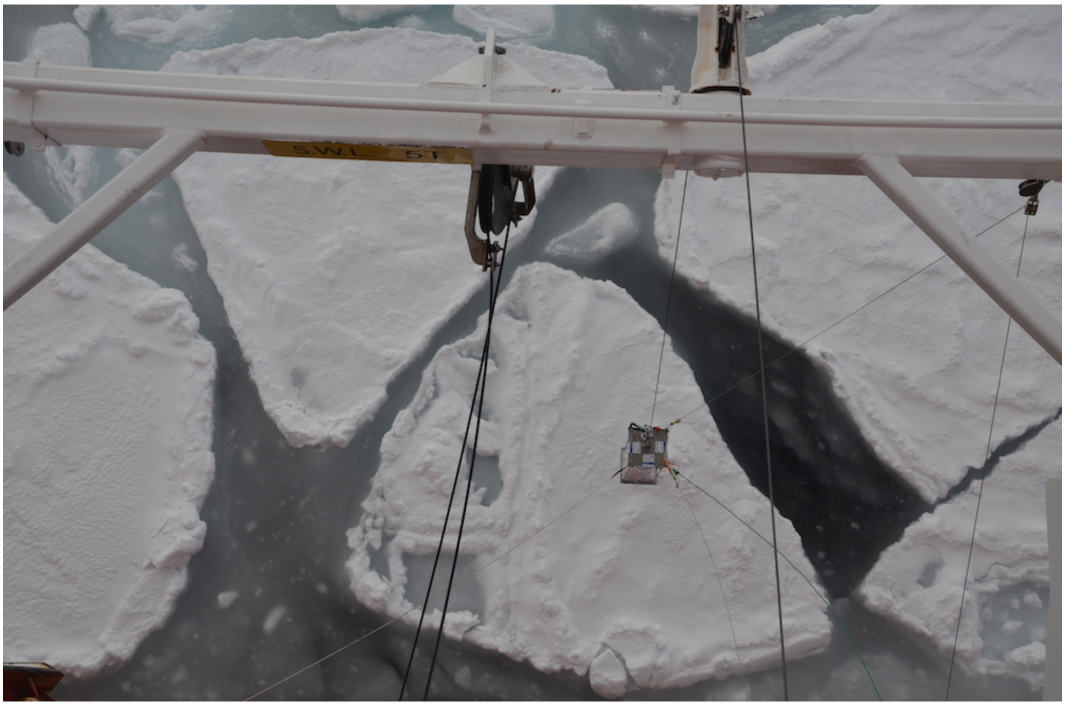

Figure 62 *The frazil ice sampler is maneuvered to a position between pancake ice floes with frazil ice inside.*

5.2.1 Rheological properties: SCALE Winter Cruise 2019

Twelve frazil ice samples were collected at three different stations (MIZ1n, MIZ2, MIZ1n) during the SCALE Winter Cruise 2019. A summary of the collected samples is shown in Table 7. The collected samples had varying volumes between 11.2 dm^3 and 16 dm^3 and frazil ice concentrations were between 17 % and 43 %. Both, the highest and lowest frazil ice concentration was obtained at MIZ2, showing that the frazil ice was not distributed equally between the pancake ice floes, reflecting continuous spatial and temporal changes. In difference to Figure 29, no net was used to separate frazil ice crystals from the sea water, but a cotton sheet. The ice volume can be calculated with the temperature-dependent density of pure ice. Rheological results for the SCALE Winter Cruise 2019 are also published by Paul et al. [148]. The pure ice density ρ_{ice} [50] can be used because it is known that no salt is incorporated into the ice lattice.

$$\rho_{\mathrm{i}}(T_{\mathrm{sample}}) = 917 - 0.1403 \times T_{\mathrm{sample}} \qquad \frac{\mathrm{kg}}{\mathrm{m}^3} \qquad 56$$

Where the sample temperature T_{sample} is given in °C. The ice content/frazil $V_{\mathrm{ice,rel}}$ ice concentration is calculated with help of Equation 57

$$V_{\mathrm{ice,rel}} = \frac{\frac{m_{\mathrm{i}} \times 10^3}{\rho_{\mathrm{i}}(T_{\mathrm{sample}})}}{V_{\mathrm{sam,abs}}} \qquad \% \qquad 57$$

where, $V_{\mathrm{sam,abs}}$ is the absolute sample volume, $\rho_{\mathrm{i}}(T_{\mathrm{sample}})$ the ice density depending on the temperature and m_{i} the ice mass. In difference to the frazil ice concentration, the sample temperature T_{sample} was constant at -1.9 °C, with three exceptions. The air temperature at the stations varied between -4.4 °C and -18.9 °C. The wind speed at the stations is lower than the literature value of 10 m/s, for a grease ice layer of 30 cm thickness to grow, reported by Smedsrud [149].

__Table 7__ Frazil ice samples from the SCALE Winter Cruise 2019.

SCALE Winter Cruise 2019							
Station	Air temperature	Wind speed	Sample name	Sample volume	Sample temperature	Ice weight	Ice content
				$V_{sam,abs}$	T_{sample}	m_{ice}	$\mathrm{V}_{\text{ice,rel}}$
	°C	**m/s**		**dm³**	**°C**	**kg**	**%**
MIZ1s	-4.4	6.3	MIZ1s-FR-01	14.0	-1.9	3.7	29%
			MIZ1s-FR-02	16.0	-1.9	3.7	25%
			MIZ1s-FR-03	12.9	-1.9	4.7	39%
MIZ2	-18.9	3.2	MIZ2-FR-01	14.3	-1.9	2.3	17%
			MIZ2-FR-02	13.5	-2.0	2.3	18%
			MIZ2-FR-03	14.5	-1.9	3.6	27%
			MIZ2-FR-04	11.2	-2.0	4.4	43%
			MIZ2-FR-05	14.6	-2.1	-	-
			MIZ2-FR-06	14.6	-1.9	-	-
MIZ1n	-6.4	8.3	MIZ1n-FR-01	13.2	-1.9	3.9	33%
			MIZ1n-FR-02	14.9	-1.9	4.4	32%
			MIZ1n-FR-03	15.3	-1.9	5.0	36%

As described in Section 4.1.2.2 the eBT-V Rheometer records the duration of the measurement in seconds, target speed in revolutions per second, speed in revolutions per second, and torque in Newton meter. An example of the data from the rheometer is presented in Figure 63 for sample MIZ2-FR-05. As described in Section 4.1.2.4 the rotation speed ramps up from $1\,\frac{revolution}{minute} = 0.017\ \frac{revolution}{second}$ to $10\,\frac{revolution}{minute} = 0.17\ \frac{revolution}{second}$ within 60 seconds. The torque profile shows an increase within the first five seconds of the measurement, followed by a decrease until 30 s and a slight increase for the rest of the measurement. The vane geometry completes 1/6 of a full turn, which is equivalent to a rotation of 60 °, within 6.66 s meaning that all vanes are one position further than at the initial starting point.

For a rheological analysis of the flow behavior of frazil ice, the shear rate $\dot{\gamma}$ and shear stress τ were calculated with help the of Equations 36 and 37. A shear-thinning behavior of the frazil ice suspension is expected, because many suspensions show a shear-thinning flow behavior. Therefore, the flow index n is set to $n = 0.5$ in a first assumption (compare Section 4.1.2.3 Table 5). The estimated flow index displays a non-Newtonian behavior of the suspension and must be confirmed by the data. The apparent viscosity is calculated by dividing the shear stress τ and the shear rate $\dot{\gamma}$.

$$\eta_{apparent} = \frac{\tau}{\dot{\gamma}} \qquad \text{Pas} \tag{58}$$

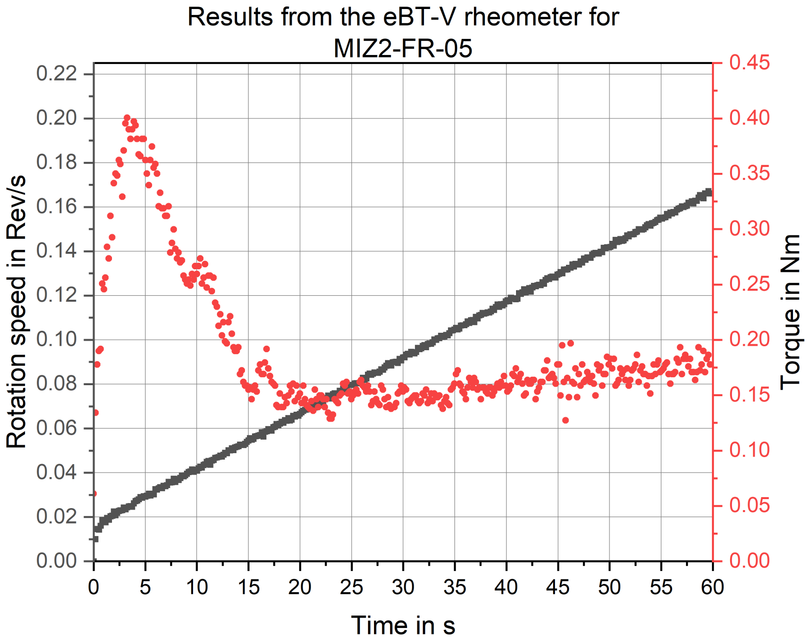

Figure 63 *Results from the rheometer for sample MIZ2-FR-05. The x-axis shows the time in seconds, the left-hand side y-axis gives the rotation speed in revolution per seconds and the right-hand side y-axis shows the torque in Newton meter.*

Shear stress and apparent viscosity for sample MIZ2-FR-05, derived from the results displayed in Figure 63, are shown in Figure 64. The errors $\Delta\dot{\gamma}$, $\Delta\tau$, $\Delta\eta_{apparent}$ are calculated by estimated maximum deviations of $\Delta R_V = 0.5\,mm$, $\Delta R_S = 0.5\,mm$, $\Delta H = 1.0\,mm$, $\Delta M = \frac{1}{150}M + 0.0073\,Nm$ and $\Delta\omega = 0.005 \times \omega\,rev/s$, $\Delta n = 0$ using quadratic error propagation.

$$\Delta\dot{\gamma} = \sqrt{\left(\frac{\partial\dot{\gamma}}{\partial R_V} \times \Delta \mathrm{R_V}\right)^2 + \left(\frac{\partial\dot{\gamma}}{\partial R_S} \times \Delta \mathrm{R}_S\right)^2 + \left(\frac{\partial\dot{\gamma}}{\partial n} \times \Delta \mathrm{n}\right)^2} \qquad 59$$

$$\Delta\eta_{apparent} = [\left(\frac{\partial\eta_{apparent}}{\partial R_V} \times \Delta \mathrm{R_V}\right)^2 + \left(\frac{\partial\eta_{apparent}}{\partial R_S} \times \Delta \mathrm{R}_S\right)^2 + \left(\frac{\partial\eta_{apparent}}{\partial n} \times \Delta \mathrm{n}\right)^2 + \left(\frac{\partial\eta_{apparent}}{\partial M} \times \Delta \mathrm{M}\right)^2 + \left(\frac{\partial\eta_{apparent}}{\partial H} \times \Delta \mathrm{H}\right)^2 + \left(\frac{\partial\eta_{apparent}}{\partial \omega} \times \Delta \omega\right)^2]^{0.5} \qquad 60$$

$$\Delta\tau = \sqrt{\left(\frac{\partial\tau}{\partial M} \times \Delta \mathrm{M}\right)^2 + \left(\frac{\partial\tau}{\partial H} \times \Delta \mathrm{H}\right)^2 + \left(\frac{\partial\tau}{\partial R_V} \times \Delta \mathrm{R_V}\right)^2} \qquad 61$$

The graph can be separated into three different parts: shear rate increase, shear rate decrease and again a slow shear rate increase. The three phases are displayed in Figure 64.

Mutual hooking of the crystals leading to increasing shear stress characterizes the first phase. The first phase ends roughly after 1/6 rotation ($\triangleq 0.96\frac{1}{\mathrm{s}}$) of the vane geometry. The first phase is followed by a decrease of shear stress when the crystals are disentangled, and larger frazil ice crystals are loosened. The third phase is marked by a slow stress increase. In this phase mostly water is shearing in the shear zone and the torque on the rheometer origins from friction between the crystals, leading to shear stresses between 20 Pa and 25 Pa. The Herschel–Bulkley model (Equation 33) is fitted for stress development in the third phase (Equation 62). It shows that a flow index of 0.5 is suitable for this shearing scenario [148]

$$\tau = 8.6 + 7.8\dot{\gamma}^{0.5} \quad \mathrm{Pa} \qquad 62$$

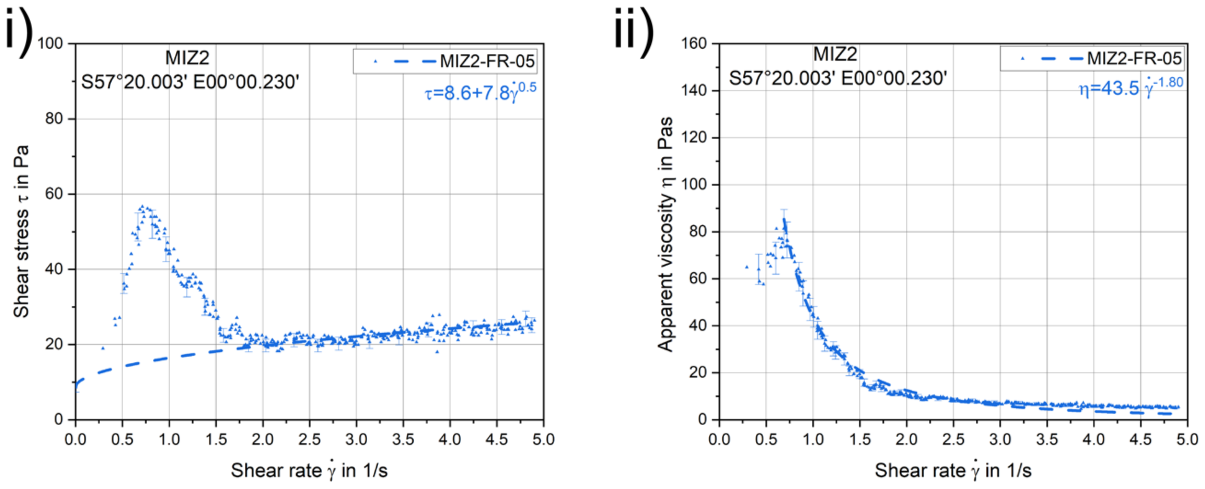

Figure 64 *i) Shear stress and ii) apparent viscosity depending on the shear rate for sample MIZ2-FR-05. The dashed line in i) shows the Herschel-Bulkley fit for the shear stress, in ii) it represents a fit of the apparent viscosity. The indicated error bars are valid for all samples in its vicinity. The sampling location is written in the headline of the figure.*

Figure 64 ii) shows the apparent viscosity (Equation 58) for sample MIZ2-FR-05. The plotted equation follows the scheme from Equation 34, but the exponent n chosen for this scenario, does not fit the boundaries of 0 < m < 1 (Table 5). This is because it does not describe the classic viscosity of the liquid but describes the unmixing of the crystals in the shearing zone.

$$\eta_{apparent} = 43.5\dot{\gamma}^{-1.80} \qquad \text{Pas} \qquad 63$$

From twelve collected samples during the SCALE Winter Cruise 2019, ten samples were used for the rheological analysis. The first two samples from MIZ2 (MIZ2-FR-01; MIZ2-FR-02) did not show noteworthy shear stress caused by a wrong handling of the frazil ice sampler. The shear stress curves in Figure 65 i) to iii) can be separated into three phases, as described for sample MIZ2-FR-05. The Herschel-Bulkley fits for the apparent viscosity do not fit the boundaries of 0 < m < 1, but describe the unmixing in the shearing zone. The apparent viscosity (Figure 65 iv) to vi)) descends towards zero for increasing shear rates, independent of the frazil ice concentration.

The frazil ice concentrations at MIZ1s are similar. Sample MIZ1s-FR-03 had the highest frazil ice content at this station (Figure 65 i)) and showed the highest apparent viscosity as well as the highest shear stress. The fitted curve of the shear stress for MIZ1s-FR-01 ($\mathrm{V_{ice,rel}} = 29\%$)

lies above the fitted curve for MIZ1s-FR-02 ($\mathrm{V}_{\mathrm{ice,rel}} = 25\ \%$) for shear rates greater than $2.0\,\frac{1}{s}$. MIZ2 samples confirm the trend that higher frazil ice content results in higher shear stress. Unfortunately, the frazil ice content was only reported for two samples from the station, but the two samples show increasing shear stress with increasing frazil ice content. MIZ2-FR-04 ($V_{\mathrm{ice,rel}} = 40\ \%$) shows a higher shear stress than MIZ2-FR-03 ($V_{\mathrm{ice,rel}} = 27\ \%$). The samples from station MIZ1n show the same behavior as that of the samples from MIZ1s. The average percentage of frazil ice in the sample is very similar for all three, therefore the shear rate only barely differs. It is noteworthy that the sample with the highest frazil ice content displays the lowest shear rate (MIZ1n-FR-02).

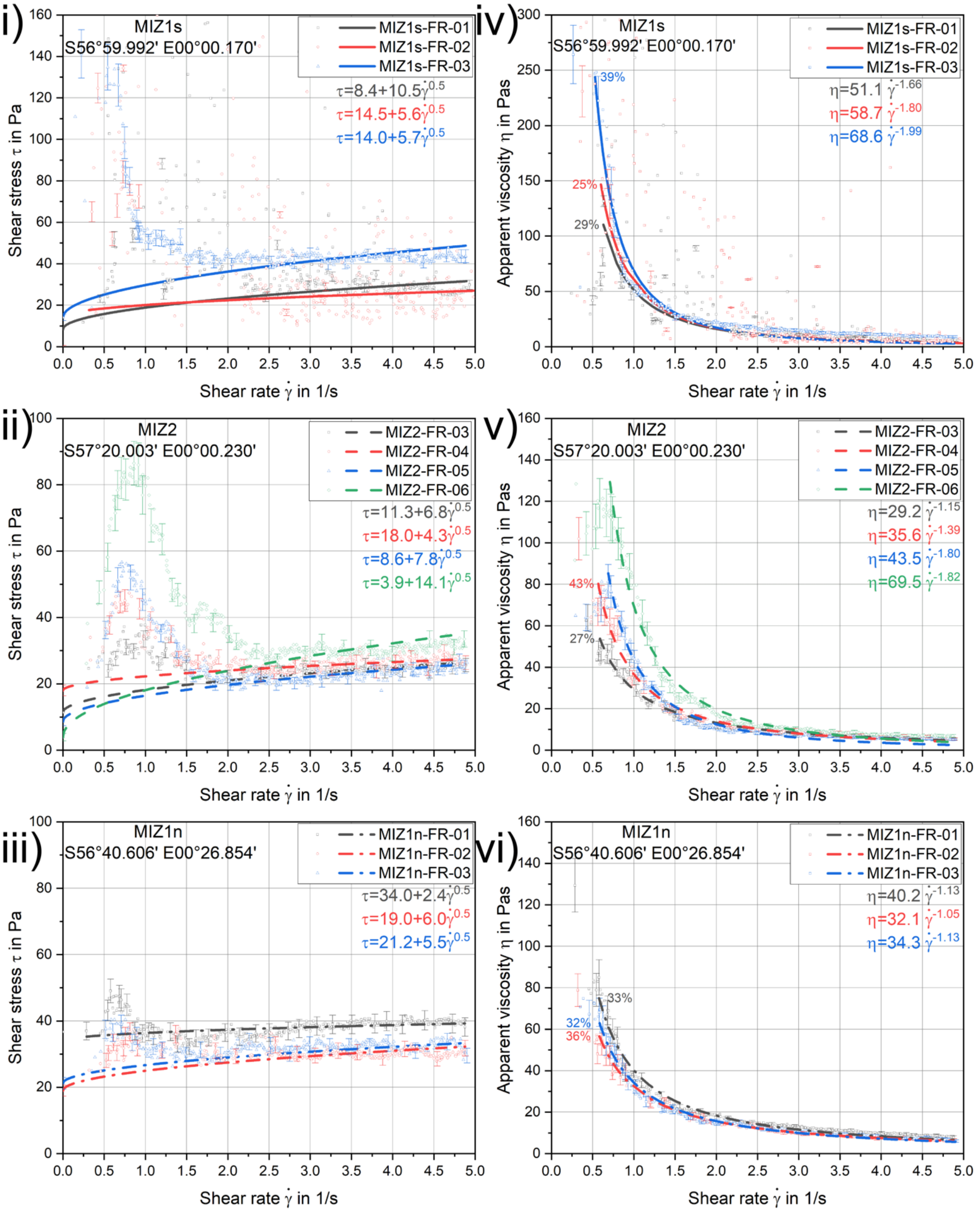

Figure 65 *i) to iii) displays the shear stress, and iv) to vi) displays apparent viscosity at MIZ1s, MIZ2, and MIZ1n. The percentage of frazil ice in the samples is given. The equations displayed in the figures describe the fit functions. The displayed error bars are valid for all data points in their vicinity.*

The flow index n was set to $n = 0.5$ to display the estimated shear thinning behavior of frazil ice. Figure 64 i) shows that $n = 0.5$ well describes the third phase of the rheological measurement. According to Macosko [150] the flow index n is determined with help of Equation 64

$$n = \frac{\mathrm{d}\ln\left(\frac{M}{M_0}\right)}{\mathrm{d}\ln\left(\frac{\omega}{\omega_0}\right)} \qquad -. \qquad 64$$

$M_0 = 1\ \mathrm{Nm}$ and $\omega_0 = 1\ \mathrm{rad/s}$ are introduced for unit consistency. Figure 66 displays all data points from sample MIZ2-FR-05, which is the same sample as in Figure 64. The transparent triangles represent the data points for the first 20 s, the blue triangles show the data points from 20 s ($\dot{\gamma} = 1.83\,\frac{1}{\mathrm{s}}$) until the end of the measurement. A linear fit is calculated for the blue data points, its slope is the flow index $n = 0.26$. A flow index of $n = 0.3$ is in the region of shear thinning flow behavior.

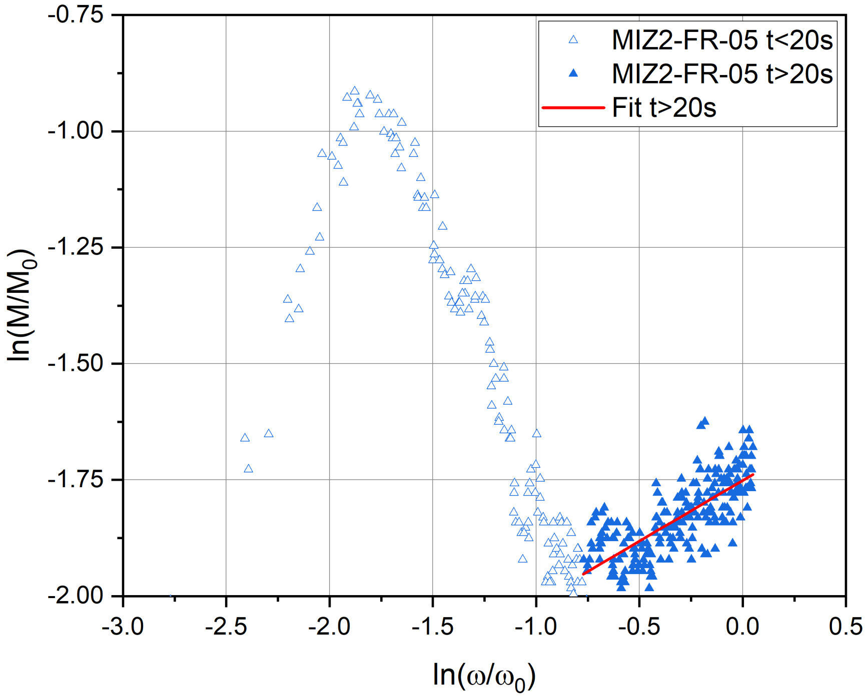

__Figure 66__ Calculation of n for MIZ2-FR-05.

The flow index n was calculated for all samples, except for MIZ1s-FR-01 and MIZ1s-FR-02 but gave widely varying results from to $n = 0.01$ up to $n = 0.26$.

Table 8 *Flow index n for samples from the SCALE Winter Cruise 2019.*

Sample name	Flow index
	n
MIZ1s-FR-01	-
MIZ1s-FR-02	-
MIZ1s-FR-03	0.02
MIZ2-FR-03	0.08
MIZ2-FR-04	0.22
MIZ2-FR-05	0.26
MIZ2-FR-06	0.12
MIZ1n-FR-01	0.01
MIZ1n-FR-02	0.08
MIZ1n-FR-03	0.07

Thus, the results of the flow index in Table 8 differ widely, but all are in the shear thinning region, the flow index is kept at $n = 0.5$ for the data analysis. Further investigations on the flow index are necessary to get a statistically proven number, because the calculated flow index from the experiment varies widely.

5.2.2 Rheological properties: SCALE Winter Cruise 2022

During the SCALE Winter Cruise 2019, 15 frazil ice samples were collected at five different stations. Four samples had a volume of $V_{\mathrm{sam,abs}} \leq 10\ dm^3$ which did not allow to perform a proper rheological measurement of the sample, therefore two samples from OD1 and two samples from ICE22 were not analyzed further. For samples with less volume than $V_{\mathrm{sam,abs}} = 10\ \mathrm{dm}^3$ the vane geometry was not immersed sufficiently into the sample. The frazil ice content of the remaining samples (Equation 57) varied between $8\ \% \leq \mathrm{V_{ice,rel}} \leq 62\ \%$. The relative frazil ice concentration was low for OD1, ICE22 and OD2, where the highest frazil ice concentration was 20 %., and $30\ \% \leq \mathrm{V_{ice,rel}} \leq 65\ \%$ for stations SB061 and SB062.

Table 9 *Frazil ice samples from the SCALE Winter Cruise 2022.*

SCALE Winter Cruise 2022							
Station	Air temperature	Wind speed	Sample name	Sample volume	Sample temperature	Ice weight	Ice content
				$V_{\mathrm{sam,abs}}$	T_{sample}	m_{ice}	$\mathrm{V}_{\mathrm{ice,rel}}$
	°C	**m/s**		**dm³**	**°C**	**kg**	**%**
OD1	-6.9	7.2	OD1-FR-01	9.0	-1.9	2.2	26%
			OD1-FR-02	10.0	-1.8	1.0	11%
			OD1-FR-03	13.2	-1.9	1.8	15%
ICE22	-8.9	3.3	ICE22-FR-01	14.1	-1.9	2.5	20%
			ICE22-FR-02	6.9	-2.0	2.7	42%
			ICE22-FR-03	4.3	-2.0	2.1	53%
OD2	-5.2	1.4	OD2-FR-01	14.9	-1.8	1.1	8%
			OD2-FR-02	12.0	-1.9	1.8	16%
			OD2-FR-03	11.5	-1.9	1.9	18%
SB061	-1.4	5.9	SB061-FR-01	11.5	-1.9	6.8	65%
			SB061-FR-02	12.0	-1.9	4.8	44%
			SB061-FR-03	11.5	-1.9	3.2	30%
SB062	-2.1	7.8	SB062-FR-01	12.6	-1.7	7.1	62%
			SB062-FR-02	16.0	-1.8	8.6	58%
			SB062-FR-03	12.6	-1.9	3.5	31%

Because a correlation between frazil ice concentration and shear stress or viscosity is expected [132], stations with a low frazil ice content ($\mathrm{V}_{\mathrm{ice,rel}} \leq 20\ \%$) and stations with a high frazil ice content ($\mathrm{V}_{\mathrm{ice,rel}} \geq 20\ \%$) are plotted together in Figure 67. The shear rate $\dot{\gamma}$, shear stress τ and apparent viscosity η_{apparent} were calculated with help of Equations 36, 37 and 58 and a flow index of $n = 0.5$.

The data from all six stations show the same shear stress profiles: First of all the stress increases due to hooking of the crystals, followed by a decrease in shear stress in the second phase and a slow increase of the shear strength in the third phase.

The general trend of the curve can be disturbed for samples OD1-FR-03 and OD2-FR-02 in Figure 67 i) and iii). Data points show an arbitrary shear strength increase after the first phase of crystal hooking. This behavior can either be explained by large ice chunks blocking the vane geometry or by a short period of shear thickening. The shear thickening can be caused by a strong interaction between the frazil ice crystals due to the local pile-up of ice crystals in certain volumes in between the vane blades. This leads to a higher shear stress before the shear thinning behavior sets in [150].

The highest shear stresses and viscosities were measured for the samples with the highest frazil ice concentration displayed in Figure 67 ii) and iv). Due to the large shear stress differences between OD1, ICE22, OD2, and SB061, SB062 the scales of the y-axes are different.

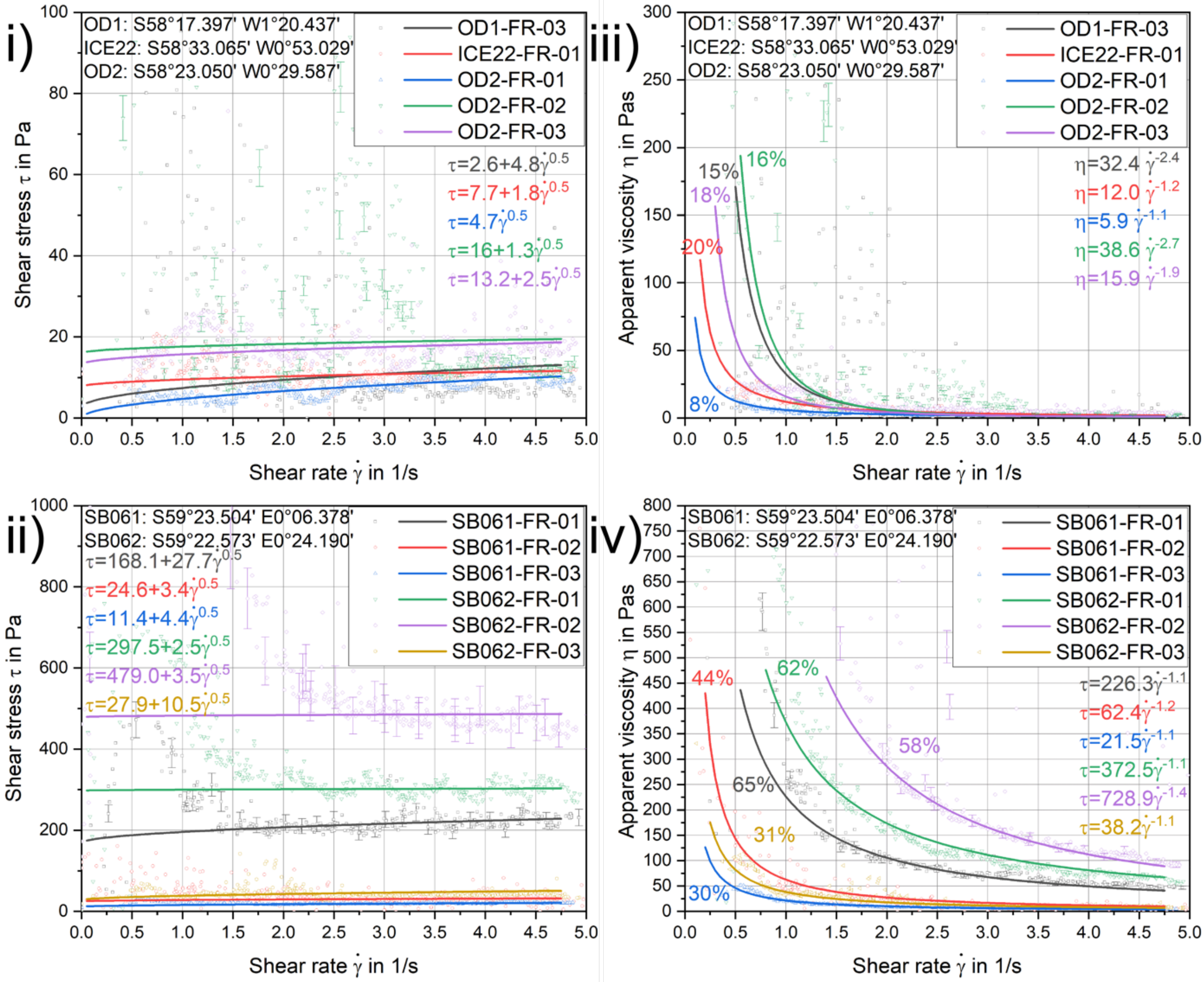

Figure 67 *Shear stress i) and ii) and apparent viscosity in iii) iv). The percentage of frazil ice in the samples is given. The equations displayed in the figures describe the fit functions. Error bars are valid for all samples in its vicinity.*

The flow index n was calculated with the help of Equation 64 and ranges from 0.1 up to 0.6. The results for the samples where a determination of the flow index was possible are presented in Table S 3. The flow index ranges from $0.1 \leq n \leq 0.6$ and shows a large inaccuracy. Nevertheless, all samples are in the shear thinning range for the third phase of the measurement, therefore the flow index n is kept at $n = 0.5$.

Figure 68 shows the sea ice conditions at the same relative position during deployment i) and retrieval ii) of the very same orange buoy. It is apparent that during deployment on the 20th of July, the ice was consolidated. No frazil or grease ice was visible. The outlines of the floes can be distinguished, and snow is equally distributed on the sea ice, without showing dark areas where the snow could be wet. The picture taken on the 23rd (Figure 68 ii)) shows the same relative position as in Figure 68 i), but the consolidated ice developed into floes again. Large areas of frazil ice are present between the floes. Frazil ice sampled at this station (SB062) is presented in Figure 67 ii) and iv). The pictures imply that the sea ice cycle is not a linear development but also allows it to develop back. This finding is especially interesting as the maximum sea ice concentration is only reached in September. Suggesting forming processes like this are not a melting phenomenon at the end of winter but common for the freezing period. Having in mind that consolidated ice can merge back to floes and grease ice like slush, it is difficult to determine whether it is newly formed frazil ice or slush.

This development from consolidated ice to ice floes is also the reason why the term frazil ice is used throughout the whole section. It proves that it is difficult to distinguish between newly formed frazil ice crystals and other forms of slush ice.

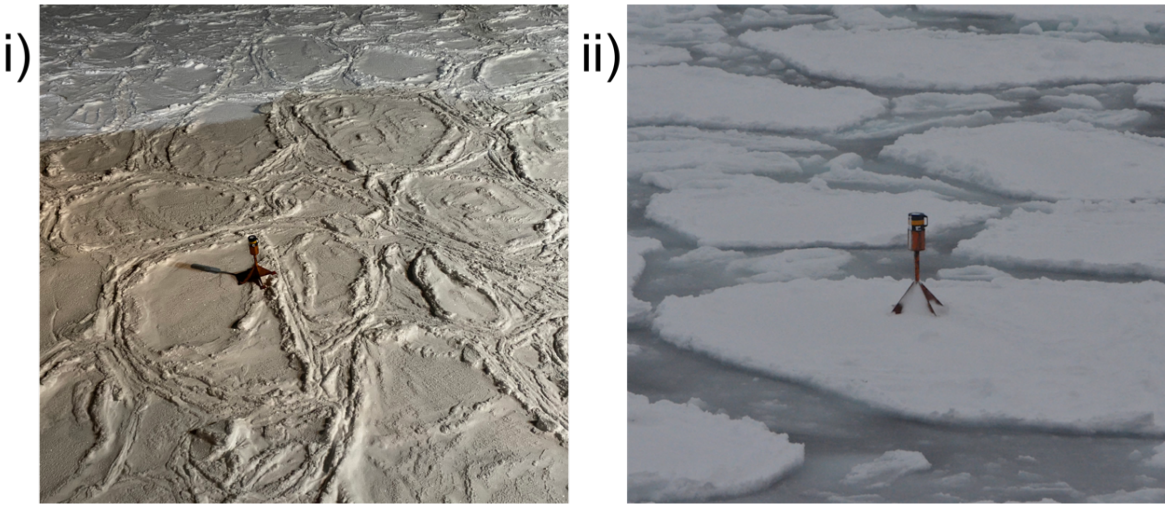

Figure 68 *i) Buoy deployment 20.07.2022 at 19:08 UTC ii) Sea ice conditions around the same buoy on the 23.07.2022 at 9:47 UTC at station SB062.*

5.2.3 Comparison and Discussion of Frazil ice rheology

Frazil ice was sampled during the SCALE Winter Cruise 2019 and 2022. In total 27 samples were collected of which 21 samples were analyzed. Six samples could not be used, because the rheometer failed to provide a reliable reading, or the sample volume was too small. The relative frazil ice content in the samples varied between $8\ \% \leq \mathrm{V}_{\mathrm{ice,rel}} \leq 62\ \%$. During the SCALE Winter Cruise 2019, the frazil ice content and the shear stress were more similar than during the SCALE Winter Cruise 2022. On the other side, the recorded outside temperatures varied stronger during the SCALE Winter Cruise 2019 than 2022.

A shear thinning flow behavior with a flow index of $n = 0.5$ was assumed to describe the flow behavior of frazil ice. It is shown that the flow curve of frazil ice can be separated into three sections: The first section is marked by a shear stress increase due to the hooking of the crystals, followed by a shear stress decrease in the second phase when the crystals are entangled, and larger frazil ice crystals are loosened. The third phase is marked by a slow increase in the shear stress and can be described by the flow index $n = 0.5$. The flow index was tried to be calculated for the analyzed samples and varied between $0.01 \leq n \leq 0.6$. It is not clear why the flow index varies in such a wide range. Reasons for the highly variable flow index could be a different morphology, crystals size and shape between the different samples or the accuracy of the rheometer is not good enough. Nevertheless, all values for the flow index are in the shear-thinning region. Therefore, the flow index is kept at $n = 0.5$.

Figure 69 shows the shear stress of the analyzed samples with a known frazil ice content. The y-axis is displayed logarithmically, the data points are colored depending on the relative frazil ice content $\mathrm{V}_{\mathrm{ice,rel}}$ of the sample. The samples are grouped into three ranges of relative frazil ice content 1. $0\ \% \leq \mathrm{V}_{\mathrm{ice,rel}} \leq 20\ \%$ (blue); 2. $20\ \% < \mathrm{V}_{\mathrm{ice,rel}} < 50\ \%$ (green) and 3. $50\ \% < \mathrm{V}_{\mathrm{ice,rel}} < 100\ \%$ (yellow). The highest shear stress is measured for the samples with the highest frazil ice content and the lowest shear stress for samples with the lowest relative frazil ice content. Data points from samples with $20\ \% < \mathrm{V}_{\mathrm{ice,rel}} < 50\ \%$ are in between the highest and lowest shear stress samples.

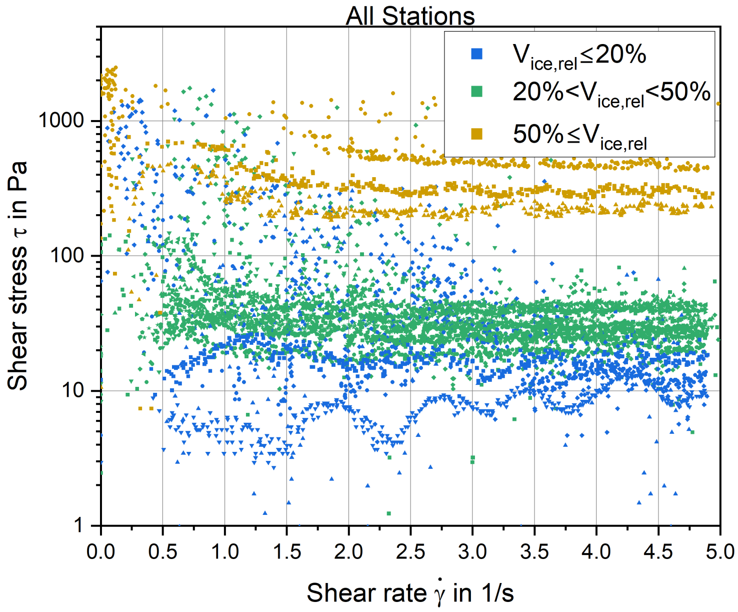

***Figure 69** Shear stress of all analyzed samples with a known frazil ice content (19 from 21 samples). Five samples had less than 20 % frazil ice, 11 samples between 20 %, and 50 % and three samples more than 50 % of frazil ice.*

When calculating the average shear stress of each sample, the trend from Figure 69 becomes more apparent. The average shear stress over brine volume is displayed in Figure 70. The average shear stress increases with increasing relative frazil ice content. A trend line is plotted, allowing to calculate the relative shear stress depending on the relative frazil ice content $V_{ice,rel}$ in %.

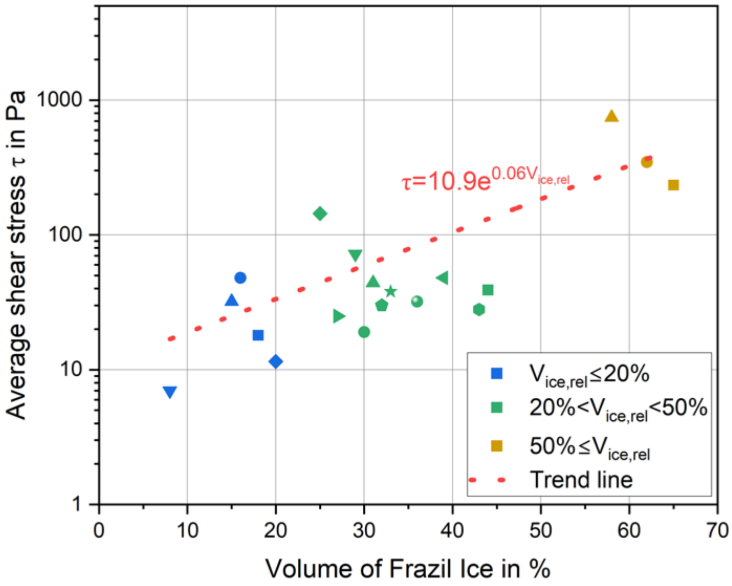

Figure 70 *Average shear stress against frazil ice volume.*

A linear behavior between the viscosity and frazil ice thickness on a log-log scale is expected in literature [151]. In this study, a linear behavior between the viscosity and the relative frazil ice content on a log-linear scale is shown. When knowing the correlation between frazil ice content and viscosity respectively shear stress, models to predict the sea ice behavior can be improved [151]. A varying frazil ice content over the year could be implemented into models to better display the different processes in the pancake ice cycle.

It is shown that sea ice viscosity depends on the shear rate. For small shear rates, the viscosity can increase up to $\eta_{apparent} = 1000\ Pas$, while for higher shear rates $2.5 \leq \dot{\gamma} \leq 5\frac{1}{s}$ lower viscosities $\eta_{apparent} \leq 50\ Pas$ are measured for most of the samples, with an exception for samples with a high relative frazil ice content. This data agrees with the literature values $14\ Pas \leq \eta_{apparent} \leq 60\ Pas$ presented in Section 3.5.2. Even though the data in the literature were measured by the indirect test they agree with the direct measurements with a rheometer. But the literature does not give viscosity results depending on the shear rate which is an essential parameter for sea ice modeling and presented in this study.

5.3 Frazil growth test

For a better understanding of the rheological properties of frazil ice one must understand the freezing process of frazil ice. The setup presented in Section 4.2.3 was used to describe the number and size of crystals and the water temperature depending on the rotation speed/turbulence and salinity of the water. Laboratory frazil ice growth is well described in literature [152], but a setup to grow frazil ice with specific properties is necessary to understand the effects on frazil ice rheology.

In total over 160 measurements with varying rotation speeds and salinity were performed. Table 10 gives an overview of the conducted tests (green: test performed; orange: test not performed). One can see that for low salinities and low rotation speeds no tests were performed. At this combination, no frazil ice crystals were formed, or the rotation was too low so that the crystals did not stay in the suspension but floated at the top. When floating at the top, the crystals could not be photographed and counted.

Table 10 *Settings for the frazil ice growth measurements. The vertical column shows the rotation speed in RPM, the horizontal row the Salinity in PSU. If the combination of row and column is green, the test was performed, if the field is orange the test was not performed.*

PSU RPM	50	100	150	200	250	300	350	400	450
0	🟧	🟧	🟧	🟩	🟩	🟩	🟩	🟩	🟩
10	🟧	🟧	🟧	🟩	🟩	🟩	🟩	🟩	🟩
20	🟧	🟧	🟧	🟩	🟩	🟩	🟩	🟩	🟩
30	🟧	🟧	🟧	🟩	🟩	🟩	🟩	🟩	🟩
35	🟧	🟧	🟧	🟩	🟩	🟩	🟩	🟩	🟩
40	🟩	🟩	🟩	🟩	🟩	🟩	🟩	🟩	🟩
50	🟩	🟩	🟩	🟩	🟩	🟩	🟩	🟩	🟩

Pictures of the floating ice crystals inside the beaker during the experiments are presented in Figure 71. The dark background is caused by the filters, which are used to make the crystals visible. It is apparent that most of the crystals have a very unregular shape only a few crystals show a dendritic structure with six arms. The largest ice crystals do not exceed a diameter of 5 mm in diameter, consistent with literature, described in Section 3.5.1.4. It is hardly possible to estimate the thickness of the frazil ice crystals due to the dynamic environment and the low thickness. Since the thickness appears much smaller compared to the diameter it is estimated to lie in the range of 1 - 100 µm, similar to reports provided in literature (Section 3.5.1.4).

Dendritic structures with six arms are mostly present in Figure 71 i) where the crystals are the smallest. The six-star shape, marked by red circles in Figure 71, only occurs at the smallest crystals. Larger crystals appear not to have a repeating shape, except that they are all irregular.

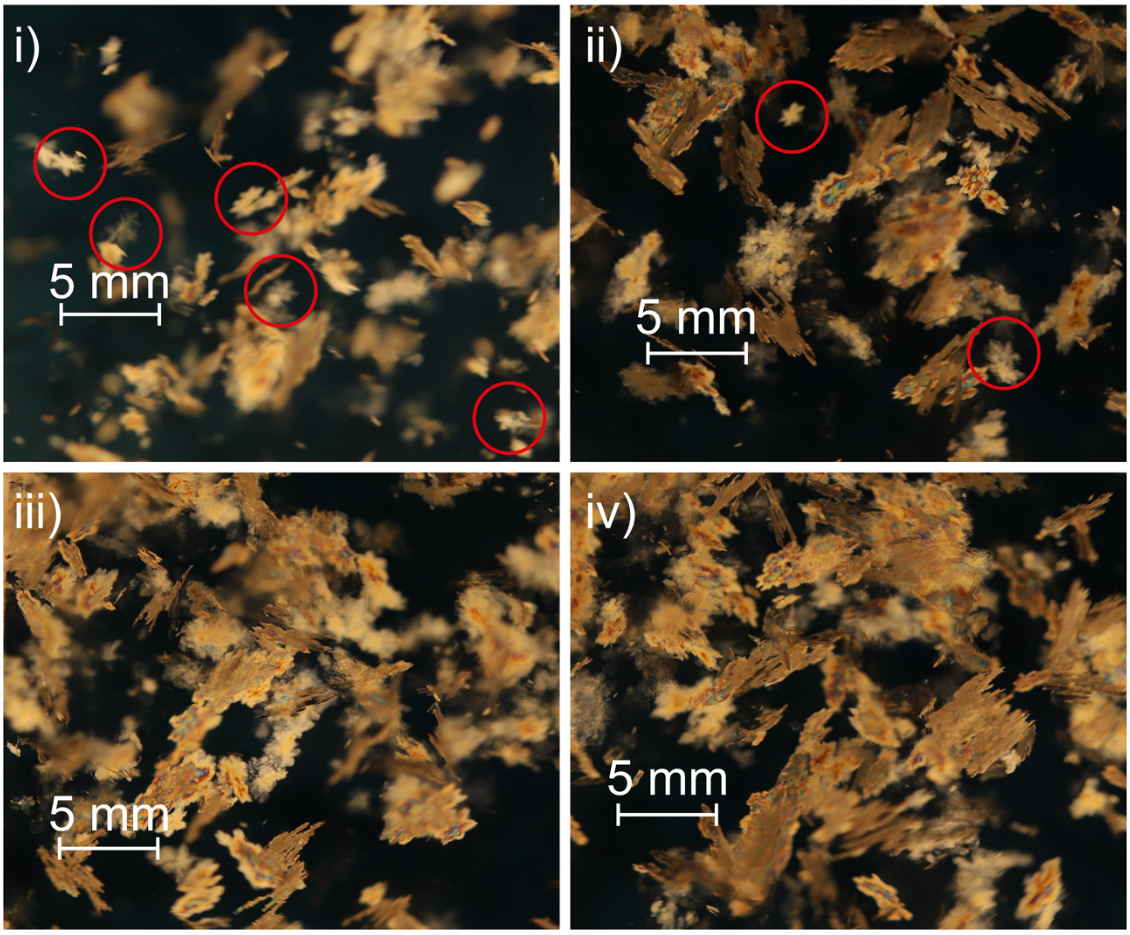

Figure 71 *Pictures of frazil ice crystals floating in the water taken with the setup presented in Figure 34. Six-star crystals are marked with red circles.*

Typical results from the experimental set-up look like the results depicted in Figure 72. The results are presented for water with a salinity of 35 PSU, a rotation speed of 450 RPM and a air temperature of -15 °C. A temperature of -15 °C was chosen for the experiments because it simulates the temperature range measured during the SCALE cruises. At higher temperatures, seeding of the water did not happen reliable, and resulted in supercooled water without frazil ice crystals. The x-axis gives the time in seconds of the measurement. The left-hand y-axis gives the number of crystals per cm^2. The unit number of crystals per cm^2 was chosen as the crystals in front of the polarization foil are counted. The immersed depth of the foil in the water changed during the experiments and the area where crystals were counted varied between 12 cm^2 to 15 cm^2. Therefore, the counted numbers were divided by the size of the area where the crystals were counted. The right-hand y-axis gives the temperature of the water in °C. The red horizontal line indicates the freezing temperature of water with a salinity of 35 PSU.

The water temperature in Figure 72 drops linearly until -2.27 °C after 75 s of the experiment. Approximately 50 s before the minimum temperature of the water is reached, the first crystals are detected inside the water. The crystallization leads to a release of energy, which slows down the temperature decrease of the water and eventually leads to an increase of the water temperature up to -2.18 °C. 150 s after the start of the experiment, a moderate increase of the crystal number is recorded and the increase of the water temperature has stopped. The residual supercooling of 0.26 °C enables further frazil ice growth.

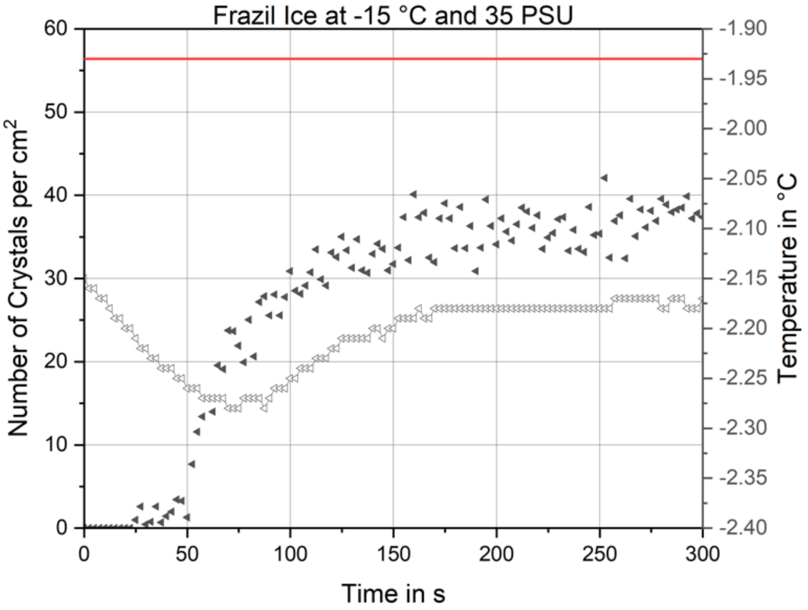

Figure 72 *Frazil ice growth at -15 °C in water with a salinity of 35 PSU. The transparent diamond shaped symbols are the water temperature, the grey filled data points the number of crystals. The red line is the freezing temperature of water with a salinity of 35 PSU.*

5.3.1 Frazil ice growth: Turbulence

The turbulence inside the beaker is adjusted by increasing or decreasing the rotation speed of the magnet stirrer. The speed intervals range from 200 RPM up to 450 RPM (Table 10). The salinity was constant at 35 PSU, which is the salinity of sea water for all turbulence-related measurements.

Figure 73 i) displays the number of crystals per cm^2, time in second of the experiment, and temperature in °C. At 100 seconds, a minimum of 10 crystals per cm^2 are measured for the first time on all graphs. Displayed are six different measurements, one measurement is presented per rotation speed. The supercooling reached the lowest value for 200 RPM with a temperature of -2.40 °C. The 200 RPM graph also shows the slowest increase of the crystal number compared to the other five measurements. For the other rotation speeds the lowest temperature was in the range of -2.27 °C to -2.30 °C, before the temperature eventually increased. While the maximum supercooling varies, the residual supercooling is similar for 200 RPM and the other measurements (-2.18 °C to -2.23 °C)

Figure 73 ii) only displays the measurements at 200 RPM, 300 RPM, and 450 RPM to reduce the number of data points and enable to see a trend of the data. The trend from Figure 73 i) that at 200 RPM the number of crystals increases the slowest is confirmed by Figure 73 ii). Comparing 300 RPM and 450 RPM, the test at 450 RPM shows the fastest frazil ice growth and the most crystals until a time of 200 s. After 200 s the number of crystals for the three tests becomes similar.

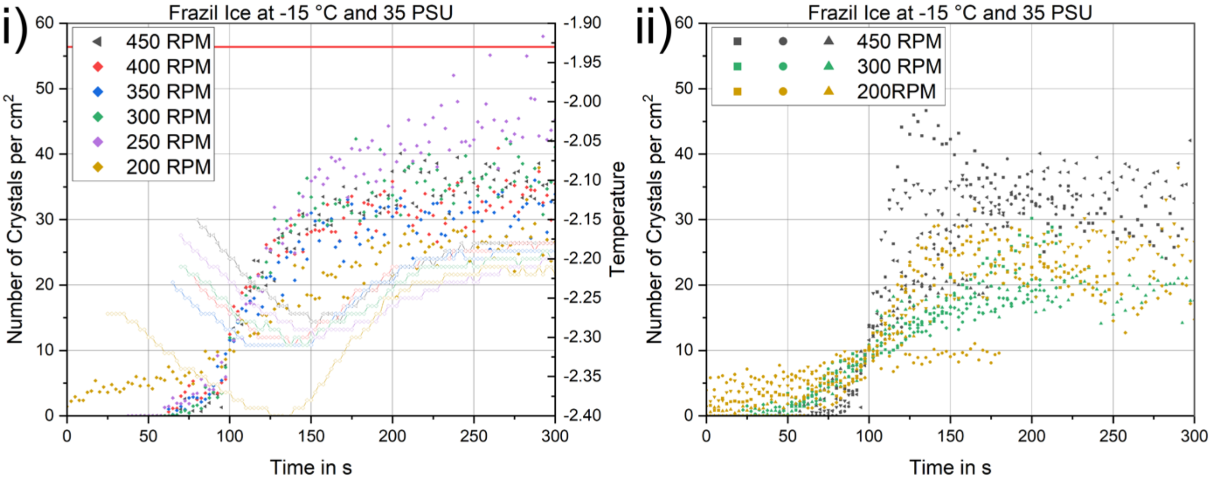

Figure 73 *Influence of rotation speed on frazil ice growth. All graphs are shifted so that at 100 s 10 or more crystals per cm^2 are measured for the first time. i) One measurement per rotation speed. The red line indicates the freezing temperature. On the right y-axis the temperature of the water is shown. ii) 16 measurements from three different rotation speeds.*

The average number of frazil ice crystals per cm^2 for all six rotation speeds, derived from 31 measurements are displayed in Figure 74 i). The curves show a similar behavior except for the 200 RPM plot, which shows a much lower slope compared to the other curves. To quantify the speed of the frazil ice growth, the time is determined from the first recorded crystal to the 10th and 20th recorded crystal (Figure 74 ii)). The time was measured after one full crystal was recorded by the camera because no active seeding of the water was used. Otherwise, the time from the seeding of the first crystal in the water could have been measured, but the seeding happened randomly for this experiment. Subsequently, the time in seconds was plotted against the rotation speed (Figure 74 ii).

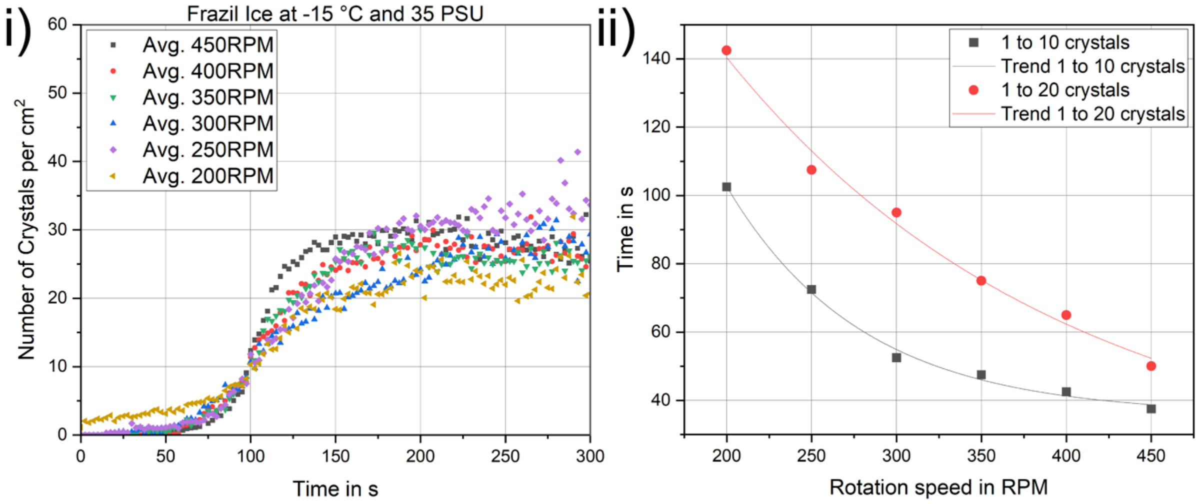

Figure 74 *i) Average number of frazil ice crystals per cm^2 for rotation speeds from 200 RPM to 450 RPM. ii) Time in s from the first crystal per cm^2 to the 10th and 20th recorded crystal.*

It is apparent that the rotation speed of the magnet stirrer influences the speed of frazil ice growth. The data points are fitted with trend lines ($200 \leq \omega_{\text{magnet}} \leq 450$). Both lines show an exponential decrease described by Equation 65 from the 1st to 10th crystal and by Equation 66 from the 1st to 20th crystal.

$$t_{1-10} = 36 + 821e^{-\frac{\omega_{\text{magnet}}}{80}} \quad \text{s} \qquad 65$$

$$t_{1-20} = 17 + 336e^{-\frac{\omega_{\text{magnet}}}{199}} \quad \text{s} \qquad 66$$

The size of each recorded crystal is measured, logged and grouped into 9 different size groups. The smallest size group is for a crystal size of $0\ \mathrm{cm}^2 < A_{\mathrm{crystal}} \leq 1 \times 10^{-5}\ \mathrm{cm}^2$, followed by $1 \times 10^{-5}\ \mathrm{cm}^2 < A_{\mathrm{crystal}} \leq 4 \times 10^{-5}\ \mathrm{cm}^2$ and quadruples each time up to the largest group $0.16\ \mathrm{cm}^2 < A_{\mathrm{crystal}} \leq 0.66\ \mathrm{cm}^2$. Afterwards, the average relative number of crystals per size group for each rotation speed is calculated. For this calculation the same 31 measurements as for Figure 74 are used. The average number of frazil ice crystals in % for the different crystal size $A_{crystal}$ groups is displayed in Figure 75.

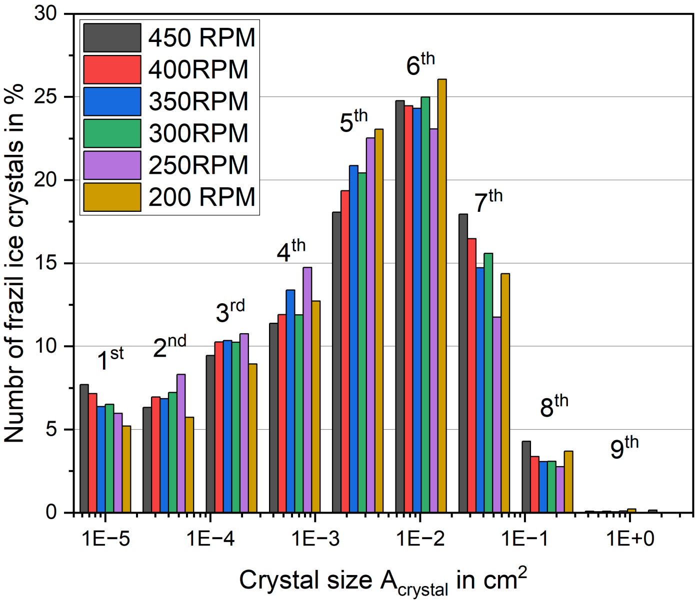

Figure 75 *Average relative amount of frazil ice crystals for different crystal sizes on a logarithmic scale for 35 PSU grouped into nine different groups to better distinguish them.*

It is apparent that independent of rotation speed, most crystals have a size between $2.6 \times 10^{-3}\ \mathrm{cm}^2$ and $1.0 \times 10^{-2}\ \mathrm{cm}^2$. For the group of the smallest crystals, a higher rotation speed leads to more small ice crystals and vice versa. At 450 RPM 7.7 % of the crystals are in between $0\ \mathrm{cm}^2 < A_{\mathrm{crystal}} \leq 1 \times 10^{-5}\ \mathrm{cm}^2$, while only 5.2 % at 200 RPM are grouped in the very same size group. The trend changes to the opposite in the 5th crystal size group ($6.4 \times 10^{-4}\ \mathrm{cm}^2 < A_{\mathrm{crystal}} \leq 2.6 \times 10^{-3}\ \mathrm{cm}^2$). At 450 RPM 18.1 % are in the 5th crystal size group, whereas there are 23.1 % for 200 RPM. For the groups in between the 1st and 5th group, one can see that the trend changes step by step. In the 6th group the relative amount is similar for all rotation speeds, whereas for the 7th group most crystals are visible for 450 RPM and decreases with decreasing rotation speed.

Summarizing one could say that most crystals have a size between $2.6 \times 10^{-3}\ \mathrm{cm}^2$ and $1.0 \times 10^{-2}\ cm^2$ independent of rotation speed. A fast rotation speed leads to smaller crystals, while a slower rotation speed develops medium frazil ice crystals. In contrast to that, fast rotation speeds produce the highest amount of large frazil ice crystals visible in the last three groups.

5.3.2 Frazil ice growth: Salinity

The salinity in the ocean is constant at 35 PSU, nevertheless, is it interesting to know how a change in salinity affects the growth process, shape, and size of frazil ice crystals. This information can later be used to grow a specific kind of frazil ice crystals for rheological testing. Therefore, experiments at different salinities were performed with the setup from Section 4.2.3.

Figure 76 shows the average number of crystals over multiple experiments for salinities of 30 PSU, 35 PSU, 40 PSU, and 50 PSU at 200 RPM and 450 RPM. The data is synchronized so that at 100 s 10 crystals per cm^2 are measured for the first time. Figure 76 i) shows results for a rotation speed of 200 RPM. All graphs in this figure show a slow crystal increase comparable to the findings in Section 5.3.1. Figure 76 ii) displays results for a rotation speed of 450 RPM, resulting in a much steeper slope of the crystal increase, also comparable to Section 5.3.1. Both figures (Figure 76 i) and ii)) do not show a trend, whether the salinity increases or decreases the number of crystals in the water. In Figure 76 i) the curves are similar, the lowest number of crystals is recorded for a rotation speed of 40 PSU. The highest number of crystals at 150 s is recorded for 50 PSU, at 200 PSU for 35 PSU and 300 s for 30 PSU. In Figure 76 ii) displaying a rotation speed of 450 RPM, the most crystals after 150 s are recorded for 50 PSU and the lowest number of crystals for 40 PSU. The results for 30 PSU and 35 PSU are in between the number of crystals for 40 PSU and 50 PSU. Results for the rotation speeds from 250 RPM up to 400 RPM are displayed in Figure A 5. No trend for the number of crystals on the salinity could be drawn from the experiment.

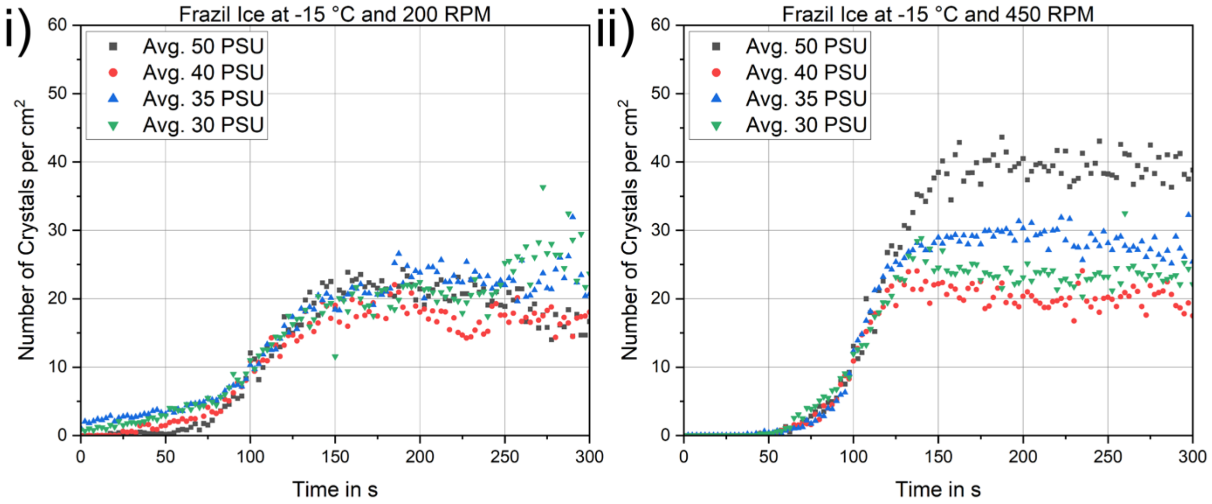

Figure 76 *Average number of crystals per cm^2 for i) 200 RPM and ii) 450 RPM at different water salinities.*

The average size distribution of the frazil ice flocs for 30 PSU, 35 PSU, 40 PSU and 50 PSU at 200 RPM and 450 RPM is displayed in Figure 77 i) and ii). The crystal area on the x-axis quadruples with every data set similar to Section 5.3.1. A trend for an increase or decrease of the crystal area is not as clear as the effect of an increasing rotation speed displayed in Figure 75.

For Figure 77 i), it appears that a higher salinity in the water leads to more smaller crystals. For the 2nd and 3rd data group ($4 \times 10^{-5}\ \mathrm{cm}^2 < A_{crystal} \leq 6.4 \times 10^{-4}\ \mathrm{cm}^2$) the most crystals are present for 40 PSU and 50 PSU. While in the 6th data group ($2.6 \times 10^{-3}\ \mathrm{cm}^2 < A_{crystal} \leq 1.0 \times 10^{-2}\ \mathrm{cm}^2$) water with a salinity of 30 PSU and 35 PSU has the most crystals.

Figure 77 ii) shows the same water salinities as in Figure 77 i) but with a rotation speed of 450 RPM instead of 200 RPM. The slight trend from Figure 77 i), that a higher salinity gives smaller crystals is not found for a rotation speed of 450 RPM. In the first five data groups ($2.6 \times 10^{-3}\ cm^2 < A_{crystal} \leq 6.4 \times 10^{-4}\ cm^2$) most crystals were recorded for a salinity of 50 PSU and 35 PSU, while 40 PSU showed fewer small crystals. The trend turns for the last three groups, where most crystals are present at a salinity of 30 PSU and 40 PSU.

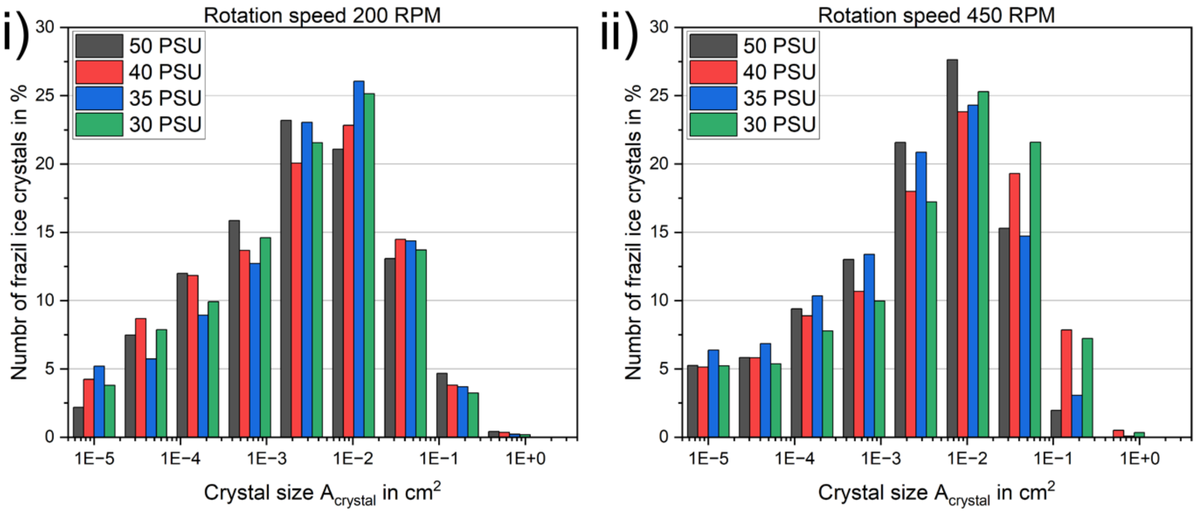

Figure 77 *Water with varying salinity at -15 °C at i) 200 RPM and ii) 450 RPM.*

The results for the rotation speeds from 250 RPM to 400 RPM are displayed in Figure A 6. No trend can be derived from that data either, how salinity affects the average crystal size during a frazil growth experiment.

Summarizing the results, the velocity of frazil ice growth is not affected in this experiment by the salt content in the water. A slower frazil growth takes place at low rotation speeds and a fast ice growth at higher rotation speeds. The frazil ice crystal size distribution seems also not to be affected by the salinity as no trend can be seen between 30 PSU, 35 PSU, 40 PSU and 50 PSU.

5.3.3 Discussion: Frazil growth test

Laboratory experiments were conducted to obtain a better understanding of the behavior of frazil ice and the possibilities to grow frazil ice in the laboratory. It has to be noted, that for the experiments presented in this study, only very young ice during the formation of the first crystals was analyzed.

Four pictures of frazil ice crystals are shown in Figure 71. The smallest crystals have a star shape with six arms, while the larger crystals are irregular in shape. In Section 3.5.1.4 different observed shapes are described, but the statements about the different shapes are vague. Frazil ice crystals are for example described as “fine spicules, plates or discoids of ice” [78] but no further findings about when the different shapes appear are given. From the pictures analyzed for this study, it seems, that when crystal start forming they first develop a star shape with six arms and later develop into larger irregular frazil ice crystals or flocs. The setup of the experiment is derived from Reimnitz et al. [80]. The original setup is much taller compared to the beaker used in this experiment and was used to study the rising rate of frazil ice and the impact of sediments on frazil ice. By applying the polarization filter as done by Schneck et al. [90], it was possible to observe single crystals and define their shape and the number of crystals. No previous study mentioned that smaller crystals tend to have a six-arm star shape and larger crystals are irregular in shape [58].

Different studies investigated the effect of turbulence on frazil ice growth [58], [68], [75], [80]. On the one hand, studies argue that increasing turbulence leads to larger and fewer crystals, while other studies demonstrate that increasing turbulence leads to more and smaller crystals [58]. As different setups were used by the investigators, the setup might have had a large influence on the emerging frazil ice crystal type. No research about the amount and size distribution of frazil ice flocs was performed by Reimnitz et al. [80]. To overcome this gap of knowledge tests were performed with water of 35 PSU, like the ocean salinity, - 15 °C air temperature, and varying turbulence induced by a rotation magnet stirrer from 200 RPM up to 450 RPM.

This study shows that increasing turbulence leads to faster frazil ice growth. This is proven by determining the time from the first recorded crystal to the tenth respectively 20th recorded crystal. Both curves presented in Figure 74 show that the time from the first recorded crystal to the tenth and 20th crystal decreases with increasing rotation speed. Reasons for a faster frazil ice growth during higher turbulence are given in literature [66], [75]. For example, higher turbulence leads to more and stronger collisions between the existing crystals, resulting in broken-off crystal pieces [66]. The broken-off crystal pieces then serve as a nucli for new frazil ice growth.

The size of frazil ice crystals is also affected by turbulence. To prove the impact of turbulence on frazil ice growth, the average relative number of frazil ice crystals is plotted in Figure 75 depending on the size of the crystals. A higher rotation speed yields more crystals in the smallest measured size group and less crystals in larger groups. Whereas a lower rotation speed has fewer crystals in the smallest crystal group and more crystals in larger crystal groups. However, the trend is not valid for the 7th group in Figure 75. In this group, most crystals are counted for the highest rotation speed.

Frazil ice growth in water with varying salinity (30 PSU, 35 PSU, 40 PSU, 50 PSU) was studied to find a trend in how the salinity affects the frazil ice growth in the presented setup. Studies showed that an increasing salinity leads to smaller and fewer crystals [90]. No trend is observed for the experiments conducted in this study. The number of crystals presented in Figure 76 and Figure A 5 are independent of the water salinity. The crystal size in Figure 77 and Figure A 6 does not show an impact of the salinity on the average size of the crystals.

The testing method itself has advantages and disadvantages. The small sample volume of 400 ml and 500 ml allows to grow frazil ice quickly in a cold laboratory. If using a smaller rheometer, the sample volume can be used instantly for rheological tests. The speed of the magnet stirrer can be easily adjusted from the outside. If compared to a propeller, which is often used to insert turbulence into water, the magnet stirrer is blunter and probably does not harm the crystals as much as a sharp propeller. The crystals are well visible through the polarization foil, but it is unclear how the immersed foil affects the crystals. A problem in this setup could be the counting of the individual crystals. As can be seen in Figure 71 iii) and iv) the crystals are close together and they are not in one plane, but before and behind each other. The software could have had problems to separate each crystal precisely, but as every image was analyzed with the same procedure the effect would influence all tests in the same manner.

5.4 Controlled ice growth test

The setup presented in Section 4.2.4 was used to grow ice under controlled conditions in the cold laboratory (Section 4.2.1). The aim of the tests was to develop a method to grow ice unidirectionally under controlled temperature conditions. Tests were performed with fresh water only and need to be further developed for testing of sea water ice. The setup was cooled from the bottom to – 15 °C. Results from the beginning until 600 min are displayed in Figure 78, and results from the beginning until 6000 min in Figure 79.

One can see that the experiment started with a water temperature of $T = 19\,°\mathrm{C}$, because all curves start at that temperature. The temperature drops fastest for the sensor closest to the cold plate (30 mm), followed by the sensors at higher points. The last sensor reaching a temperature of 3 °C is the sensor at a height of 240 mm. A temperature of 3 °C is critical in the experiment, as water has its highest density between $T = 3\,°C$ and $4\,°C$. For higher and lower temperatures, the density of water decreases. Therefore, water with the highest density at $T = 3\,°C$ sinks to the ground. If the water cools down further it rises to the top, consequently the water at the higher sensors successively measures temperatures at 3 °C. As soon as the temperature reached $T = 3\,°C$ in the whole setup, the temperature decreased further until the freezing point of $T = 0\,°C$ is reached. Nevertheless, even the 240 mm sensor measures a temperature of 3 °C for approximately 30 min. This is because the water is filled a little bit higher than 240 mm into the setup and the water above 240 mm needs to cool as well. The first ice occurs at 440 min, indicated by a decrease of the measured temperature below 0 °C.

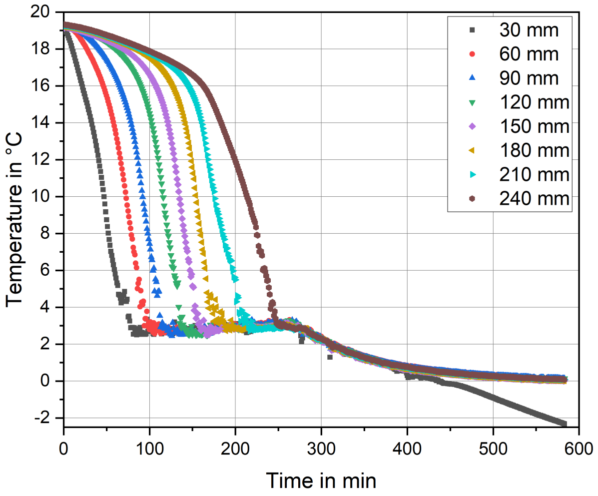

Figure 78 *Temperature of the sensors at different heights from the bottom. The line "30 mm" corresponds to the sensor closest to the cold plate, the sensor "240 mm" is furthest away from the cold plate. Time from 0 min to 600 min.*

The further temperature development of the test is displayed in Figure 79. The temperature curve below 0 °C for 30 mm appeared linear in Figure 78, but one can see that the curve is strongly non-linear in Figure 79. The water freezes from bottom to top, indicated by the sensors recording temperatures below 0 °C. After 3800 minutes the whole setup is frozen and the temperature in the setup decreases much faster, because no energy is needed anymore to form ice, but the energy is only used to cool the ice. This explains the much higher cooling rate after 3800 min compared to the temperature change beforehand. Again, the rapid temperature drop occurs sometime after the 240 mm sensor records sub-zero temperature because the water above the 240 mm sensor needs to freeze also. Once the water is frozen completely, the temperature in the setup drops to the set temperature of - 15 °C. Depending on how far the sensors are away from the cold plate, the temperature is a bit higher than the set temperature as the setup is not insulated perfectly.

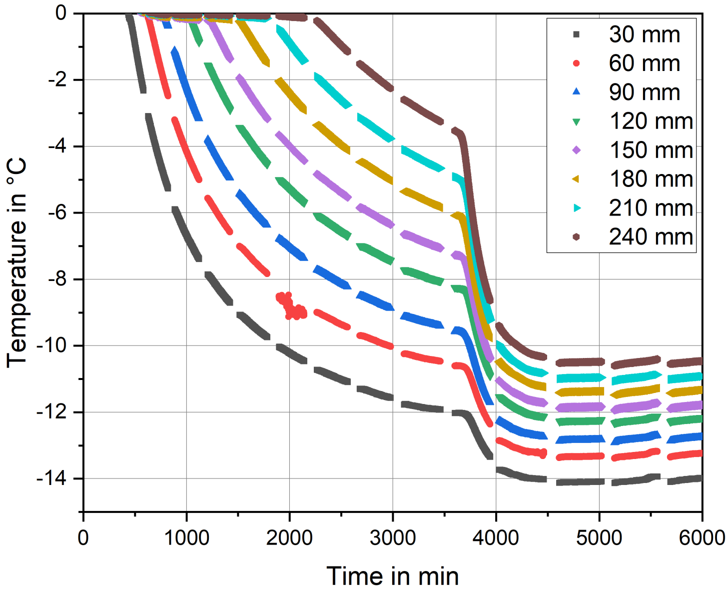

Figure 79 *Temperature of the sensors at different heights from the bottom. The line "30 mm" corresponds to the sensor closest to the cold plate, the sensor "240 mm" is furthest away from the cold plate. Time from 0 min to 6000 min.*

5.4.1 Discussion: Controlled ice growth

The mechanical properties of sea ice are affected by many parameters such as texture, brine content, porosity, growth structure and temperature. The idea of controlled sea ice growth is to receive uniform samples for mechanical tests. Under controlled conditions, the different parameters can be changed separately, and the effect of the parameter change can be analyzed. Therefore, sea ice grown under controlled conditions is the best way to understand changes in the mechanical properties between different stations and different seasons.

A setup to grow ice unidirectional from bottom to top is presented. One-dimensional growth is important, as this is the dominant growth in the MIZ. The water is only cooled from the surface, resulting in a unidirectional sea ice growth. Temperature over time curves for controlled sea ice growth is presented. A reversed (bottom to top) growth is chosen, because if samples would be grown the other way around, the increasing pressure from the ice forming at the bottom would either destroy the sample or the growth setup.

A benefit of growing ice in this setup is, that the resulting ice just needs to get cut at the ends and can be used for further testing instantly without further processing. The setup can be used with different salinities. The sensors used for these experiments are frozen into the ice, but they can also be replaced by external sensors glued to the setup so that the same sample can be monitored and tested afterwards. By filling artificial frazil ice into the setup, different textures of the ice can be produced. Turbulence can be induced into the setup by a stirrer at the top of the setup.

Disadvantages of the setup are the relatively long growth time for the samples of more than four days and the limited capacity of the cooling device underneath the setup. To produce more samples, the artificial sea ice tank from Section 4.2.2 could be used. Unfortunately, the sea ice containers did not work because of problems at the cooling unit, so no further experiments with the wave tank could be performed.

To summarize, the bottom-to-top growth is suited to monitor ice growth. Samples have the perfect size for mechanical testing, but the growth capacities are limited. More research must be performed to grow multiple uniform samples in the future.

6 Conclusion and outlook

Sea ice in the Marginal Ice Zone of the Antarctic undergoes spatial and temporal changes all year long. Sea ice, its thickness, concentration, and mechanical properties affect the global climate and vice versa. A better understanding of the mechanical properties of Antarctic sea ice is necessary to evaluate the processes influencing the Antarctic sea ice precisely.

Fundamentals of the ice structure and flaws in the ice structure affecting the mechanical properties of ice are given. The freezing process of sea ice in the MIZ of the Antarctic is explained. Frazil ice is the first ice forming, damping the ocean, and later develops into large pancake ice floes. Salt is rejected from the ice lattice while freezing, leading to brine pockets and brine channels of sea ice, which is the biggest difference between fresh water ice and sea ice.

Figure 80 *Mearuement of the rheological properties of frazil ice uring the SCALE Winter Cruise 2022.*

Different techniques are used to investigate the rheological properties of frazil ice and the strength of pancake ice and consolidated ice. A custom-designed setup to collect frazil ice from the ocean and a modified vane rheometer including sampling and measuring protocols are presented. Procedures to collect ice samples from pancake and consolidated ice are explained. Two different testing devices were used to investigate the strength and Young's modulus of sea ice. The industrial-manufactured GCTS compression device had several disadvantages. Therefore, a new compression device was manufactured. Different laboratory tests for the growth of artificial sea ice are presented. The idea of laboratory tests is to investigate the influence of the varying parameters affecting sea ice growth separately.

For future testing, improvements are necessary for the field and in the laboratory to get better and more meaningful results from the Antarctic sea ice. The compression test should be performed as soon as possible after sampling, to avoid structural changes in the ice. If not possible, the compression test could be performed at a temperature of -5 °C, because it is closer to the temperature of most of the ice while floating in the ocean. A temperature of -10 °C is only reached close to the top, where the ice is in contact with the atmosphere. By testing at -5 °C the brine content in the ice would increase and be closer to the brine content in the ocean. The density of each sample needs to be measured before testing, because this gives information about the air content in the ice and gives the most meaningful results in this study. A method to determine the salinity of the tested compression samples would improve the brine readings for later analysis. Besides that, samples with the same brine volume show different strength results, which might be caused by the morphology of the ice. To better understand different strength results, the morphology of the compression samples should be investigated.

The rheology of frazil ice was tested a short time after sampling the frazil ice. Nevertheless, the composition of the sample (ice-water-ratio) might be disturbed by sampling the ice from the ocean. Instead, the rheometer could be lowered between pancake ice floes to do the rheological measurement in the ocean in between the pancake ice floes. Additionally, the shape of frazil ice crystals from the ocean should be studied with cross-polarization technique. This would give an insight into the size distribution and volume of frazil ice crystals.

Besides analyzing frazil ice in the laboratory through visual methods, a direct method to determine the frazil ice content could be developed. Using visual methods has the disadvantage of only being able to guess the volume of ice in the water by assuming that the individual crystals are of the same thickness. By growing frazil ice crystals in an airtight sealed container, with one outlet in the form of a thin vertical glass pipe, one could take advantage of the lower density of ice compared to water. If the crystals form, the water level in the thin glass pipe will rise. By knowing the volume of water in the pipe one can calculate the volume of ice in the beaker.

To better understand the mechanisms influencing the strength of sea ice, methods to grow ice under controlled conditions in the laboratory must be improved. The sample‘s temperature can be monitored while growing the ice. Besides that, the salinity should be recorded while freezing the ice. The wave tank can be used to grow artificial ice under realistic outdoor conditions and to test equipment and procedures for upcoming cruises.

7 References

[1] P. R. Shukla *et al.*, *Climate Change 2022: Mitigation of Climate Change. Contribution of Working Group III to the Sixth Assessment Report of the Intergovernmental Panel on Climate Change*, no. 1. 2022.

[2] L. Al-Ghussain, “Global warming: review on driving forces and mitigation,” *Environ. Prog. Sustain. Energy*, vol. 38, no. 1, pp. 13–21, Jan. 2019.

[3] M. M. *et al.*, “Polar Regions,” in *IPCC Special Report on the Ocean and Cryosphere in a Changing Climate*, Cambridge University Press, 2022, pp. 203–320.

[4] T. Thompson, “Antarctic sea ice hits lowest minimum on record,” *Nature*, no. March, Mar. 2022.

[5] A. Macalady and R. Katie Thomas, “Antarctic Sea Ice Variability in the Southern Ocean-Climate System,” in *Antarctic Sea Ice Variability in the Southern Ocean-Climate System*, 2017.

[6] J. E. Stopa, P. Sutherland, and F. Ardhuin, “Strong and highly variable push of ocean waves on Southern Ocean sea ice,” *Proc. Natl. Acad. Sci. U. S. A.*, vol. 115, no. 23, pp. 5861–5865, 2018.

[7] S. Kivimaa and P. Kosloff, “Compressive Strength And Structure Of Sea Ice In The Weddell Sea, Antarctica,” *Built Environ.*, vol. 5, p. 12, 1994.

[8] L. A. Roach, I. Eisenman, T. J. W. Wagner, E. Blanchard-Wrigglesworth, and C. M. Bitz, “Asymmetry in the seasonal cycle of Antarctic sea ice driven by insolation,” *Nat. Geosci.*, vol. 15, no. 4, pp. 277–281, Apr. 2022.

[9] S. Stammerjohn and T. Maksym, “Gaining (and losing) Antarctic sea ice: variability, trends and mechanisms,” in *Sea Ice*, Chichester, UK: John Wiley & Sons, Ltd, 2016, pp. 261–289.

[10] C. Eayrs, D. Faller, and D. M. Holland, “Mechanisms driving the asymmetric seasonal cycle of Antarctic Sea Ice in the CESM Large Ensemble,” *Ann. Glaciol.*, vol. 61, no. 82, pp. 171–180, Sep. 2020.

[11] T. Maksym, “Arctic and Antarctic Sea Ice Change: Contrasts, Commonalities, and Causes,” *Ann. Rev. Mar. Sci.*, vol. 11, no. 1, pp. 187–213, 2019.

[12] U. Farooq, W. Rack, A. McDonald, and S. Howell, “Representation of sea ice regimes in the Western Ross Sea, Antarctica, based on satellite imagery and AMPS wind data,” *Clim. Dyn.*, May 2022.

[13] P. Wadhams, M. A. Lange, and S. F. Ackley, “The ice thickness distribution across the Atlantic sector of the Antarctic Ocean in midwinter,” *J. Geophys. Res.*, vol. 92, no. C13, p. 14535, 1987.

[14] C. Strong and I. G. Rigor, “Arctic marginal ice zone trending wider in summer and narrower in winter,” *Geophys. Res. Lett.*, vol. 40, no. 18, pp. 4864–4868, Sep. 2013.

[15] G. S. Dieckmann and H. H. Hellmer, “The Importance of Sea Ice: An Overview,” in *Sea Ice*, Oxford, UK: Blackwell Science Ltd, pp. 1–21.

[16] V. A. Squire, “Past, present and impendent hydroelastic challenges in the polar and subpolar seas,” *Philos. Trans. R. Soc. A Math. Phys. Eng. Sci.*, vol. 369, no. 1947, pp. 2813–2831, Jul. 2011.

[17] M. A. Lange, S. F. Ackley, P. Wadhams, G. S. Dieckmann, and H. Eicken, “Development of Sea Ice in the Weddell Sea,” *Ann. Glaciol.*, vol. 12, pp. 92–96, Jan. 1989.

[18] W. D. Hibler, “A Dynamic Thermodynamic Sea Ice Model,” *J. Phys. Oceanogr.*, vol. 9, no. 4, pp. 815–846, Jul. 1979.

[19] C. Mehlmann and T. Richter, “A modified global Newton solver for viscous-plastic sea

ice models," *Ocean Model.*, vol. 116, pp. 96–107, 2017.
[20] N. Urabe and M. Inoue, "Mechanical Properties of Antarctic Sea Ice," *J. Offshore Mech. Arct. Eng.*, vol. 110, no. 4, pp. 403–408, Nov. 1988.
[21] T. C. Hansen, "The everlasting hunt for new ice phases," *Nat. Commun.*, vol. 12, no. 1, p. 3161, May 2021.
[22] J. D. Bernal and R. H. Fowler, "A Theory of Water and Ionic Solution, with Particular Reference to Hydrogen and Hydroxyl Ions," *J. Chem. Phys.*, vol. 1, no. 8, pp. 515–548, Aug. 1933.
[23] A. Metrekine, "Arctic Engineering: Ice Physics," 2016.
[24] T. Bartels-Rausch *et al.*, "Ice structures, patterns, and processes: A view across the icefields," *Rev. Mod. Phys.*, vol. 84, no. 2, pp. 885–944, 2012.
[25] W. F. Weeks, "Growth conditions and the structure and properties of sea ice," *Phys. ice-covered seas*, vol. 1, pp. 25–104, 1998.
[26] P. V. Hobbs, *Ice Physics*. 1974.
[27] E. M. Schulson and P. Duval, *Creep and Fracture of Ice*. Cambridge: Cambridge University Press, 2009.
[28] D. Gross and T. Seelig, *Bruchmechanik*. Berlin, Heidelberg: Springer Berlin Heidelberg, 2011.
[29] H. W. Zoch, *Materialwissenschaft und Werkstofftechnik: Foreword*, vol. 40, no. 5–6. 2009.
[30] W. F. Weeks and S. F. Ackley, "The Growth, Structure, and Properties of Sea Ice," in *The Geophysics of Sea Ice*, Boston, MA: Springer US, 1986, pp. 9–164.
[31] R. J. D. Tilley, *Defects in Solids*, vol. 258, no. 5532. Hoboken, NJ, USA: John Wiley & Sons, Inc., 2008.
[32] W. F. Hosford, "Crystal Defects," in *Materials Science*, Cambridge: Cambridge University Press, pp. 33–42.
[33] T. Hondoh, "Nature and behavior of dislocations in ice," *Phys. Ice Core Rec.*, pp. 3–24, 2000.
[34] C. E. Hayes and W. W. Webb, "Dislocations in Ice," *Science (80-.).*, vol. 147, no. 3653, pp. 44–45, Jan. 1965.
[35] R. W. Whitworth, "The Core Structure and the Mobility of Dislocations in Ice," *J. Glaciol.*, vol. 21, no. 85, pp. 341–359, Jan. 1978.
[36] M. F. Ciappina, A. Iorio, P. Pais, and A. Zampeli, "Torsion in quantum field theory through time-loops on Dirac materials," *Phys. Rev. D*, vol. 101, no. 3, p. 036021, Feb. 2020.
[37] M. Montagnat and P. Duval, "Dislocations in Ice and Deformation Mechanisms: from Single Crystals to Polar Ice," *Defect Diffus. Forum*, vol. 229, pp. 43–0, Sep. 2004.
[38] E. M. Schulson and P. Duval, "Ductile behavior of polycrystalline ice: experimental data and physical processes," in *Creep and Fracture of Ice*, Cambridge: Cambridge University Press, pp. 101–152.
[39] G. W. Timco and W. F. Weeks, "A review of the engineering properties of sea ice," *Cold Reg. Sci. Technol.*, vol. 60, no. 2, pp. 107–129, 2010.
[40] E. M. Schulson, "Brittle failure of ice," *Eng. Fract. Mech.*, vol. 68, no. 17–18, pp. 1839–1887, Dec. 2001.
[41] E. M. Schulson and P. Duval, "Brittle compressive failure of unconfined ice," in *Creep and Fracture of Ice*, Cambridge: Cambridge University Press, 2010, pp. 236–265.
[42] E. M. Schulson and P. Duval, "Brittle compressive failure of confined ice," in *Creep and Fracture of Ice*, Cambridge: Cambridge University Press, pp. 266–319.

[43] “Tenth Report of the Joint Panel on Oceanographic Tables and Standards,” 1981.

[44] K. Hill, T. Dauphinee, and D. Woods, “The extension of the Practical Salinity Scale 1978 to low salinities,” *IEEE J. Ocean. Eng.*, vol. 11, no. 1, pp. 109–112, Jan. 1986.

[45] F. J. Millero, R. Feistel, D. G. Wright, and T. J. McDougall, “The composition of Standard Seawater and the definition of the Reference-Composition Salinity Scale,” *Deep Sea Res. Part I Oceanogr. Res. Pap.*, vol. 55, no. 1, pp. 50–72, Jan. 2008.

[46] C. Petrich and H. Eicken, “Overview of sea ice growth and properties,” in *Sea Ice*, Chichester, UK: John Wiley & Sons, Ltd, 2016, pp. 1–41.

[47] Intergovernmental Oceanographic Commission, Scientific Committee on Oceanic Research, and International Association for the Physical Sciences of the Ocean, “The international thermodynamic equation of seawater – 2010: Calculation and use of thermodynamic properties,” 2010.

[48] A. Assur, “Composition of sea ice and its tensile strength,” 1960.

[49] P. O. Moslet, “Field testing of uniaxial compression strength of columnar sea ice,” *Cold Reg. Sci. Technol.*, vol. 48, no. 1, pp. 1–14, Apr. 2007.

[50] G. F. N. Cox and W. F. Weeks, “Equations for Determining the Gas and Brine Volumes in Sea-Ice Samples,” *J. Glaciol.*, vol. 29, no. 102, pp. 306–316, Jan. 1983.

[51] M. Leppäranta and T. Manninen, “The brine and gas content of sea ice with attention to low salinities and high temperatures,” 1988.

[52] G. F. N. Cox and W. F. Weeks, “Brine Drainage and Initial Salt Entrapment in Sodium Chloride Ice.,” *US Army Corps Eng Cold Reg Res Eng Lab Res Rep*, no. 345, 1975.

[53] P. REID and R. A. MASSOM, “SUCCESSIVE ANTARCTIC SEA ICE EXTENT RECORDS DURING 2012, 2013, AND 2014,” in *STATE OF THE CLIMATE IN 2014*, 2015, pp. 163–164.

[54] F. Hicks, “An overview of river ice problems: CRIPE07 guest editorial,” *Cold Reg. Sci. Technol.*, vol. 55, no. 2, pp. 175–185, Feb. 2009.

[55] V. McFarlane, M. Loewen, and F. Hicks, “Measurements of the evolution of frazil ice particle size distributions,” *Cold Reg. Sci. Technol.*, vol. 120, pp. 45–55, 2015.

[56] S. F. Daly, “International Association for Hydraulic Research Working Group on Thermal Regimes Report on Frazil Ice,” 1994.

[57] S. Martin, “Frazil Ice In Rivers and Oceans,” *Fluid Mech.*, vol. 13, pp. 379–397, 1981.

[58] P. D. Barrette, “Understanding frazil ice: The contribution of laboratory studies,” *Cold Reg. Sci. Technol.*, vol. 189, no. May, p. 103334, Sep. 2021.

[59] P. G. Vekilov, “Nucleation,” *Cryst. Growth Des.*, vol. 10, no. 12, pp. 5007–5019, Dec. 2010.

[60] T. Koop, “Homogeneous Ice Nucleation in Water and Aqueous Solutions,” *Zeitschrift für Phys. Chemie*, vol. 218, no. 11, pp. 1231–1258, Nov. 2004.

[61] T. E. Osterkamp, “Frazil-Ice nucleation by mass-exchange processes at the air-water interface,” *J. Glaciol.*, vol. 19, no. 81, pp. 619–625, 1974.

[62] R. C. Schnell and G. Vali, “Biogenic Ice Nuclei: Part I. Terrestrial and Marine Sources,” *J. Atmos. Sci.*, vol. 33, no. 8, pp. 1554–1564, Aug. 1976.

[63] S. E. Lindow, “The Role of Bacterial ICE Nucleation in Frost Injury to Plants,” *Annu. Rev. Phytopathol.*, vol. 21, no. 1, pp. 363–384, Sep. 1983.

[64] F. MacIntyre, “The top millimeter of the ocean,” *Sci. Am.*, vol. 230, no. 5, pp. 62–77, 1974.

[65] P. V. Hobbs and A. J. Alkezweeny, “The Fragmentation of Freezing Water Droplets in Free Fall,” *J. Atmos. Sci.*, vol. 25, no. 5, pp. 881–888, Sep. 1968.

[66] S. P. Clark and J. C. Doering, “Frazil flocculation and secondary nucleation in a counter-

rotating flume," *Cold Reg. Sci. Technol.*, vol. 55, no. 2, pp. 221–229, 2009.

[67] F. N. P. and M. J. R. C., "Algorithms for computation of fundamental properties of seawater," 1983.

[68] S. Q. Ye, J. Doering, and H. T. Shen, "A laboratory study of frazil evolution in a counter-rotating flume," *Can. J. Civ. Eng.*, vol. 31, no. 6, pp. 899–914, 2004.

[69] C. Schneck, V. McFarlane, and M. Loewen, "Laboratory measurements of frazil ice properties in saline water," in *19th Workshop on the Hydraulics of Ice Covered Rivers*, 2017.

[70] L. H. Smedsrud, "Frazil-ice entrainment of sediment: large-tank laboratory experiments," *J. Glaciol.*, vol. 47, no. 158, pp. 461–471, 2001.

[71] T. O. D. Hanley and G. Tsang, "Formation and properties of frazil in saline water," *Cold Reg. Sci. Technol.*, vol. 8, no. 3, pp. 209–221, 1984.

[72] T. O. Hanley and B. Michel, "Laboratory formation of border ice and frazil slush," *Can. J. Civ. Eng.*, vol. 4, no. 2, pp. 153–160, 1977.

[73] T. Carstens, "Experiments with supercooling and ice formation in flowing water.," *Geofys. Publ.*, vol. 26, pp. 1–18, 1966.

[74] R. Ettema, M. F. Karim, and J. F. Kennedy, "Laboratory experiments on frazil ice growth in supercooled water," *Cold Reg. Sci. Technol.*, vol. 10, no. 1, pp. 43–58, 1984.

[75] S. Clark and J. Doering, "Experimental investigation of the effects of turbulence intensity on frazil ice characteristics," *Can. J. Civ. Eng.*, vol. 35, no. 1, pp. 67–79, 2008.

[76] L. Thompson, M. Smith, J. Thomson, S. Stammerjohn, S. Ackley, and B. Loose, "Frazil ice growth and production during katabatic wind events in the Ross Sea, Antarctica," *Cryosph.*, vol. 14, no. 10, pp. 3329–3347, Oct. 2020.

[77] H. H. Shen, S. F. Ackley, and M. A. Hopkins, "A conceptual model for pancake-ice formation in a wave field," *Ann. Glaciol.*, vol. 33, no. 3, pp. 361–367, Sep. 2001.

[78] H. R. Kivisild, "RIver and Lake Ice Terminology," in *Proceeding of IAHR Symposium on Ice and Its Action on Hydraulic Structures*, 1970.

[79] V. McFarlane, M. Loewen, and F. Hicks, "Field measurements of suspended frazil ice. Part II: Observations and analyses of frazil ice properties during the principal and residual supercooling phases," *Cold Reg. Sci. Technol.*, vol. 165, no. April, p. 102796, Sep. 2019.

[80] E. Reimnitz, J. R. Clayton, E. W. Kempema, J. R. Payne, and W. S. Weber, "Interaction of rising frazil with suspended particles: tank experiments with applications to nature," *Cold Reg. Sci. Technol.*, vol. 21, no. 2, pp. 117–135, 1993.

[81] W. F. Hosford, "Sintering," in *Materials Science*, Cambridge: Cambridge University Press, 2006, pp. 144–152.

[82] R. Ettema, Z. Chen, and J. C. Doering, "Making Frazil Ice in a Large Ice Tank," in *Workshop on the Hydraulics of Ice Covered Rivers*, 2003.

[83] T. R. Ghobrial, M. R. Loewen, and F. Hicks, "Laboratory calibration of upward looking sonars for measuring suspended frazil ice concentration," *Cold Reg. Sci. Technol.*, vol. 70, pp. 19–31, 2012.

[84] T. R. Ghobrial, M. R. Loewen, and F. E. Hicks, "Characterizing suspended frazil ice in rivers using upward looking sonars," *Cold Reg. Sci. Technol.*, vol. 86, pp. 113–126, 2013.

[85] G. Tsang, "An instrument for measuring frazil concentration," *Cold Reg. Sci. Technol.*, vol. 10, no. 3, pp. 235–249, 1985.

[86] S. F. Daly and S. Colbeck, "Frazil Ice Measurements in CRREL's Flume Facility," in *Proc. Syrup. Ice 1986. Int. Assoc. Hydraul. Res.,* 1986, pp. 427–438.

[87] T. E. Osterkamp and J. P. Gosink, “Frazil ice formation and ice cover development in interior Alaska streams,” *Cold Reg. Sci. Technol.*, vol. 8, no. 1, pp. 43–56, 1983.

[88] J. R. Marko and M. Jasek, “Frazil monitoring by multi-frequency Shallow Water Ice Profiling Sonar (SWIPS): present status,” in *20th IAHR International Symposium on Ice, Lathi, Finland, June 14 to 18*, 2010.

[89] M. Richard, B. Morse, S. F. Daly, and J. Emond, “Quantifying suspended frazil ice using multi-frequency underwater acoustic devices,” *River Res. Appl.*, vol. 27, no. 9, pp. 1106–1117, Nov. 2011.

[90] C. C. Schneck, T. R. Ghobrial, and M. R. Loewen, “Laboratory study of the properties of frazil ice particles and flocs in water of different salinities,” *Cryosph.*, vol. 13, no. 10, pp. 2751–2769, Oct. 2019.

[91] Z.-X. Zhang, “Effect of Temperature on Rock Fracture,” *Rock Fract. Blasting*, pp. 111–133, 2016.

[92] K. Newyear, “Comparison of laboratory data with a viscous two-layer model of wave propagation in grease ice,” vol. 104, pp. 7837–7840, 1999.

[93] R. Wang and H. H. Shen, “Gravity waves propagating into an ice-covered ocean: A viscoelastic model,” *J. Geophys. Res. Ocean.*, vol. 115, no. 6, pp. 1–12, 2010.

[94] X. Zhao and H. H. Shen, “Wave propagation in frazil/pancake, pancake, and fragmented ice covers,” *Cold Reg. Sci. Technol.*, vol. 113, pp. 71–80, 2015.

[95] P. Wadhams, F. Parmiggiani, and G. de Carolis, “Wave dispersion by antarctic pancake ice from SAR images: A method for measuring ICE thickness,” in *Proceedings of SEASAR 2006 Advances in SAR Oceanography from Envisat and ERS Missions*, 2006, no. ESA SP-613.

[96] W. E. Rogers, J. Thomson, H. H. Shen, M. J. Doble, P. Wadhams, and S. Cheng, “Dissipation of wind waves by pancake and frazil ice in the autumn Beaufort Sea,” *J. Geophys. Res. Ocean.*, vol. 121, no. 11, pp. 7991–8007, Nov. 2016.

[97] J. B. Keller, “Gravity waves on ice-covered water,” *J. Geophys. Res. C Ocean.*, vol. 103, no. 3334, pp. 7663–7669, 1998.

[98] R. Wang and H. H. Shen, “Experimental study on surface wave propagating through a grease-pancake ice mixture,” *Cold Reg. Sci. Technol.*, vol. 61, no. 2–3, pp. 90–96, 2010.

[99] T. Maksym, S. E. Stammerjohn, S. Ackley, and R. Massom, “Antarctic sea ice- A polar opposite?,” *Oceanography*, vol. 25, no. 3, pp. 140–151, 2012.

[100] J. Turner, “Solve Antarctica’s sea-ice puzzle,” *Nature*, vol. 547, no. 7663, pp. 275–277, 2016.

[101] M. Smith and J. Thomson, “Ocean Surface Turbulence in Newly Formed Marginal Ice Zones,” *J. Geophys. Res. Ocean.*, vol. 124, no. 3, pp. 1382–1398, 2019.

[102] M. Shokr and N. Sinha, *Sea Ice: Physics and Remote Sensing*. Hoboken, NJ: John Wiley & Sons, Inc, 2015.

[103] M. A. Lange and H. Eicken, “Textural characteristics of sea ice and the major mechanisms of ice growth in the Weddell Sea,” *Ann. Glaciol.*, vol. 15, no. 1984, pp. 210–215, Jan. 1991.

[104] H. Eicken, C. Bock, R. Wittig, H. Miller, and H. O. Poertner, “Magnetic resonance imaging of sea-ice pore fluids: Methods and thermal evolution of pore microstructure,” *Cold Reg. Sci. Technol.*, vol. 31, no. 3, pp. 207–225, 2000.

[105] R. J. Galley *et al.*, “Imaged brine inclusions in young sea ice—Shape, distribution and formation timing,” *Cold Reg. Sci. Technol.*, vol. 111, pp. 39–48, Mar. 2015.

[106] N. A. Mel’nichenko and A. B. Slobodyuk, “Nuclear magnetic resonance study of sea-water freezing mechanisms: 1. Temperature dependence of relative brine content in

sea ice," *J. Glaciol.*, vol. 59, no. 216, pp. 711–718, Jul. 2013.

[107] M. W. Hunter, R. Dykstra, M. H. Lim, T. G. Haskell, and P. T. Callaghan, "Using Earth's Field NMR to Study Brine Content in Antarctic Sea Ice: Comparison with Salinity and Temperature Estimates," *Appl. Magn. Reson.*, vol. 36, no. 1, pp. 1–8, Nov. 2009.

[108] O. Crabeck, R. J. Galley, L. Mercury, B. Delille, J. -L. Tison, and S. Rysgaard, "Evidence of Freezing Pressure in Sea Ice Discrete Brine Inclusions and Its Impact on Aqueous-Gaseous Equilibrium," *J. Geophys. Res. Ocean.*, vol. 124, no. 3, pp. 1660–1678, Mar. 2019.

[109] K. M. Golden, H. Eicken, A. L. Heaton, J. Miner, D. J. Pringle, and J. Zhu, "Thermal evolution of permeability and microstructure in sea ice," *Geophys. Res. Lett.*, vol. 34, no. 16, pp. 2–7, 2007.

[110] R. M. Lieb-Lappen, E. J. Golden, and R. W. Obbard, "Metrics for interpreting the microstructure of sea ice using X-ray micro-computed tomography," *Cold Reg. Sci. Technol.*, vol. 138, pp. 24–35, 2017.

[111] O. Crabeck *et al.*, "Imaging air volume fraction in sea ice using non-destructive X-ray tomography," *Cryosphere*, vol. 10, no. 3, pp. 1125–1145, 2016.

[112] S. Johnson, B. Matlakala, M. Vichi, and T. Rampai, "Crystal size and texture data of sea ice from the Antarctic Marginal Ice Zone collected in Winter 2019," *Zenodo, Aug. 09, 2022.*

[113] H. Eicken and M. A. Lange, "Development and properties of sea ice in the coastal regime of the southeastern Weddell Sea," *J. Geophys. Res.*, vol. 94, no. C6, p. 8193, 1989.

[114] J. P. Dempsey, D. M. Cole, and S. Wang, "Tensile fracture of a single crack in first-year sea ice," *Philos. Trans. R. Soc. A Math. Phys. Eng. Sci.*, vol. 376, no. 2129, p. 20170346, Sep. 2018.

[115] A. Totman, O. E. Uzorka, J. Dempsey, and D. Cole, "Sub-size fracture testing of FY sea ice," in *International Conference on Fracture Mechanics of Concrete and Concrete Structures*, 2007, pp. 1683–1690.

[116] D. M. Cole and J. P. Dempsey, "In situ Sea Ice Experiments in McMurdo Sound: Cyclic Loading, Fracture, and Acoustic Emissions," *J. Cold Reg. Eng.*, vol. 18, no. 4, pp. 155–174, Dec. 2004.

[117] R. A. Paige and C. W. Lee, "Preliminary Studies on Sea Ice in McMurdo Sound, Antarctica, During 'Deep Freeze 65,'" *J. Glaciol.*, vol. 6, no. 46, pp. 515–528, Jan. 1967.

[118] C. Ng, U. J. Alengaram, L. S. Wong, K. H. Mo, M. Z. Jumaat, and S. Ramesh, "A review on microstructural study and compressive strength of geopolymer mortar, paste and concrete," *Constr. Build. Mater.*, vol. 186, pp. 550–576, Oct. 2018.

[119] Q. Wang, Z. Li, R. Lei, P. Lu, and H. Han, "Estimation of the uniaxial compressive strength of Arctic sea ice during melt season," *Cold Reg. Sci. Technol.*, vol. 151, no. 7512, pp. 9–18, Jul. 2018.

[120] I. Sevčík, "3D Finite Elements with Rotational Degrees of Freedom," *FEM Consult. s.r.o, Brno*.

[121] Z. Li, L. Zhang, P. Lu, M. Leppäranta, and G. Li, "Experimental study on the effect of porosity on the uniaxial compressive strength of sea ice in Bohai Sea," *Sci. China Technol. Sci.*, vol. 54, no. 9, pp. 2429–2436, Sep. 2011.

[122] H. Han, Z. Li, W. Huang, P. Lu, and R. Lei, "The uniaxial compressive strength of the Arctic summer sea ice," *Acta Oceanol. Sin.*, vol. 34, no. 1, pp. 129–136, 2015.

[123] G. W. Timco and R. M. W. Frederking, "Confined compression tests: Outlining the failure envelope of columnar sea ice," *Cold Reg. Sci. Technol.*, vol. 12, no. 1, pp. 13–28,

Feb. 1986.

[124] J. P. Poplin and A. T. Wang, “Mechanical properties of rafted annual sea ice,” *Cold Reg. Sci. Technol.*, vol. 23, no. 1, pp. 41–67, Nov. 1994.

[125] J. A. Richter-Menge, “US research in ice mechanics: 1987-1990,” *Cold Reg. Sci. Technol.*, vol. 20, no. 3, pp. 231–246, 1992.

[126] P. O. Moslet *et al.*, “Sea Ice – Vertical Pile Interaction Experiment, Part III: Test Results 2004,” in *POAC ’05: Proceedings of the 18th International Conference on Port and Ocean Engineering under Arctic Conditions*, 2005, vol. 1, pp. 471–480.

[127] G. W. Timco and R. M. W. Frederking, “Compressive strength of sea ice sheets,” *Cold Reg. Sci. Technol.*, vol. 17, no. 3, pp. 227–240, Feb. 1990.

[128] African Maritime Solutions Group (PTY) LtD, “PASSENGER INFORMATION BROCHURE ‘S.A. AGULHAS II,’” 2017.

[129] IACS, “Requirements concerning Polar Class,” 2019.

[130] GCTS, “PLT-2W Wireless Point Load Test System: Description.”

[131] F. Paul, T. Mielke, and D. C. Lupascu, “Experimental setup to determine rheological properties of frazil ice,” *Rheol. Messungen an Baustoffen 2020*, pp. 75–84, 2020.

[132] J. F. Steffe, *Rheological Methods in Food Process Engineering*. Freeman Press, East Lansing, 1992.

[133] A. Y. Malkin and A. I. Isayev, “LIQUIDS,” in *Rheology Concepts, Methods, and Applications*, Elsevier, 2012, pp. 127–221.

[134] H. A. Barnes, “The yield stress—a review or ‘παντα ρει’—everything flows?,” *J. Nonnewton. Fluid Mech.*, vol. 81, no. 1–2, pp. 133–178, Feb. 1999.

[135] T. F. Tadros, *Rheology of Dispersions*. Weinheim, Germany: Wiley-VCH Verlag GmbH & Co. KGaA, 2010.

[136] M. Haist *et al.*, “Interlaboratory study on rheological properties of cement pastes and reference substances: comparability of measurements performed with different rheometers and measurement geometries,” *Mater. Struct.*, vol. 53, no. 4, p. 92, Aug. 2020.

[137] N. Q. Dzuy and D. V. Boger, “Yield Stress Measurement for Concentrated Suspensions,” *J. Rheol. (N. Y. N. Y).*, vol. 27, no. 4, pp. 321–349, 1983.

[138] I. M. Krieger, “Shear Rate in the Couette Viscometer,” *Trans. Soc. Rheol.*, vol. 12, no. 5, 1968.

[139] C. Haas, “Ice tank investigations of the microstructure of artificial sea ice grown under different boundary conditions during INTERICE II,” in *Proc. Of HYDRALAB workshop in Hannover*, 1999.

[140] S. Skatulla *et al.*, “Physical and mechanical properties of winter first-year ice in the Antarctic marginal ice zone along the Good Hope Line,” *Cryosph.*, vol. 16, no. 7, pp. 2899–2925, Jul. 2022.

[141] S. Skatulla *et al.*, “Physical and mechanical results for sea ice data - SCALE Winter Cruise 2019, SA Agulhas II,” *Zivahub, Jul. 08*, 2021.

[142] A. Kovacs, “Estimating the full-scale flexural and compressive strength of first-year sea ice,” *J. Geophys. Res. Ocean.*, vol. 102, no. C4, pp. 8681–8689, Apr. 1997.

[143] M. Wei and F. Dai, “Laboratory-scale mixed-mode I/II fracture tests on columnar saline ice,” *Theor. Appl. Fract. Mech.*, vol. 114, no. January, p. 102982, Aug. 2021.

[144] M. Wei, A. Polojärvi, D. M. Cole, and M. Prasanna, “Strain response and energy dissipation of floating saline ice under cyclic compressive stress,” *Cryosph.*, vol. 14, no. 9, pp. 2849–2867, Sep. 2020.

[145] F. Paul, T. Mielke, R. Audh, and D. C. Lupascu, “Sea ice strength development from

freezing to melting in the Antarctic marginal ice zone," in *Proceedings of the YIC 2021 - VI ECCOMAS Young Investigators Conference*, 2021.

[146] R. R. Audh *et al.*, "Sea ice core temperature and salinity data collected during the 2019 SCALE Spring Cruise," *Zenodo, Aug. 16, 2022*.

[147] World Meteorological Organization, "Sea-ice Information and Services," 2021.

[148] F. Paul *et al.*, "Frazil Ice in the Antarctic Marginal Ice Zone," *J. Mar. Sci. Eng.*, vol. 9, no. 6, p. 647, Jun. 2021.

[149] L. H. Smedsrud, "Grease-ice thickness parameterization," *Ann. Glaciol.*, vol. 52, no. 57 PART 1, pp. 77–82, 2011.

[150] C. W. Macosko, *Rheology: Principles, Measurements and Applications*. Wiley, New York, 1994.

[151] G. De Carolis, P. Olla, and F. De Santi, "SAR image wave spectra to retrieve the thickness of grease-pancake sea ice using viscous wave propagation models," *Sci. Rep.*, vol. 11, no. 1, pp. 1–14, 2021.

[152] P. D. Barrette, "Understanding frazil ice: The contribution of laboratory studies," *Cold Reg. Sci. Technol.*, vol. 189, no. October 2020, p. 103334, Sep. 2021.

8 Appendix

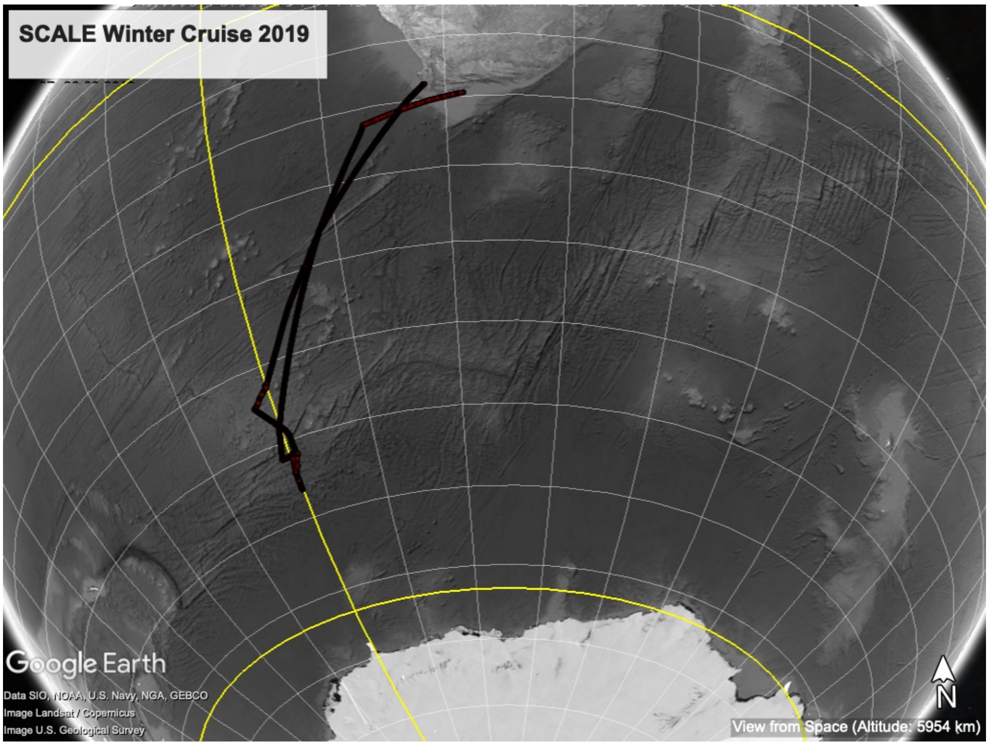

***Figure A 1** Trajectory of the SCALE Winter Cruise 2019.*

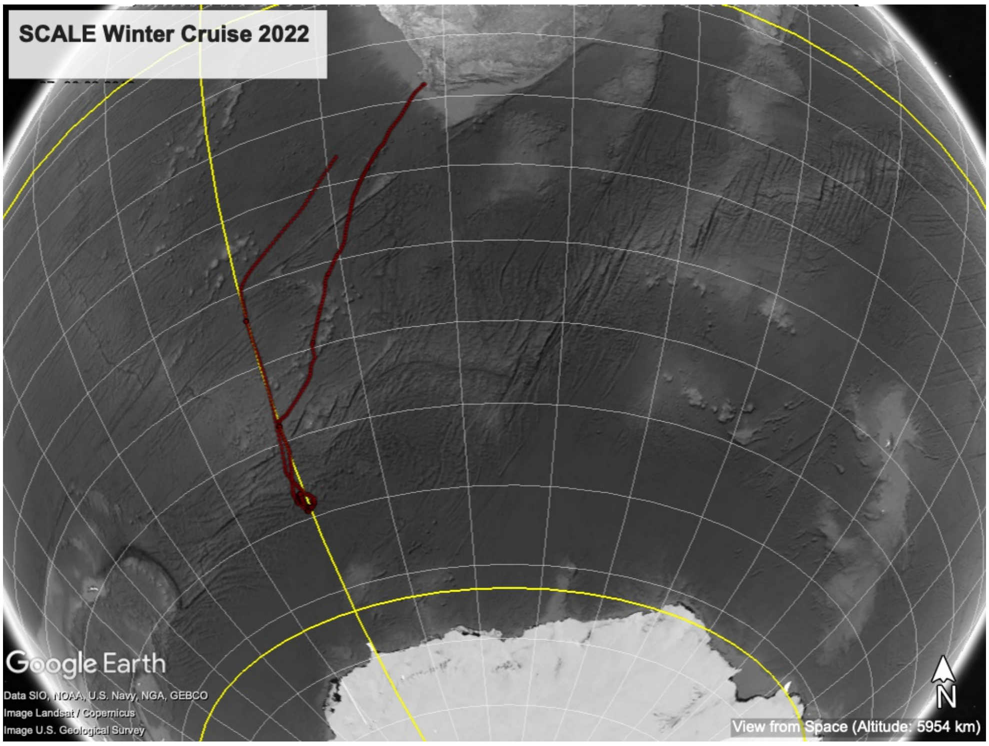

***Figure A 2** Trajectory of the SCALE Winter Cruise 2022.*

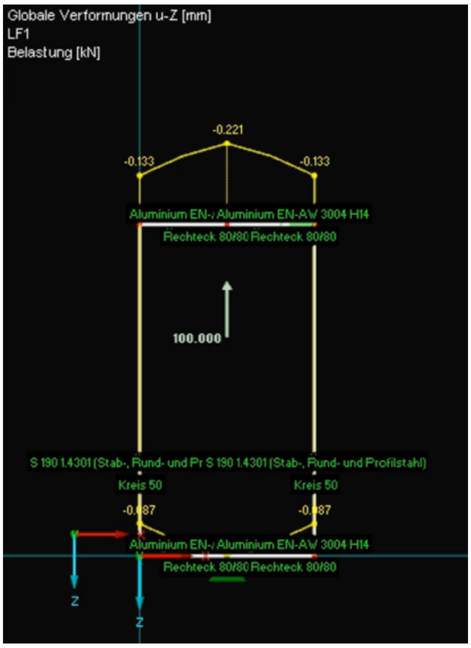

Figure A 3 *A two dimensional calculation of the maximum displacement by help of RFEM 6.02. The bottom and top bar have a surface of 80*80 mm, the vertical steel rods have a diameter of 50 mm. A support is attached in the center (z-direction) and left hand side of the bottom bar (x-direction). The maximum displacement is calculated to 0.221 mm.*

Figure A 4 *A-frame (height 4.79 m, the arm is 2.00 m long) of the SA Agulhas II. The door (e) is opened automatically, the A-frame can be swung out (b), the frazil sampler is attached to the small roll (c), loops for the opening and closing ropes of the frazil ice collector (f), operators can stand on the sides of the frame (a) to hold the sampler into position.*

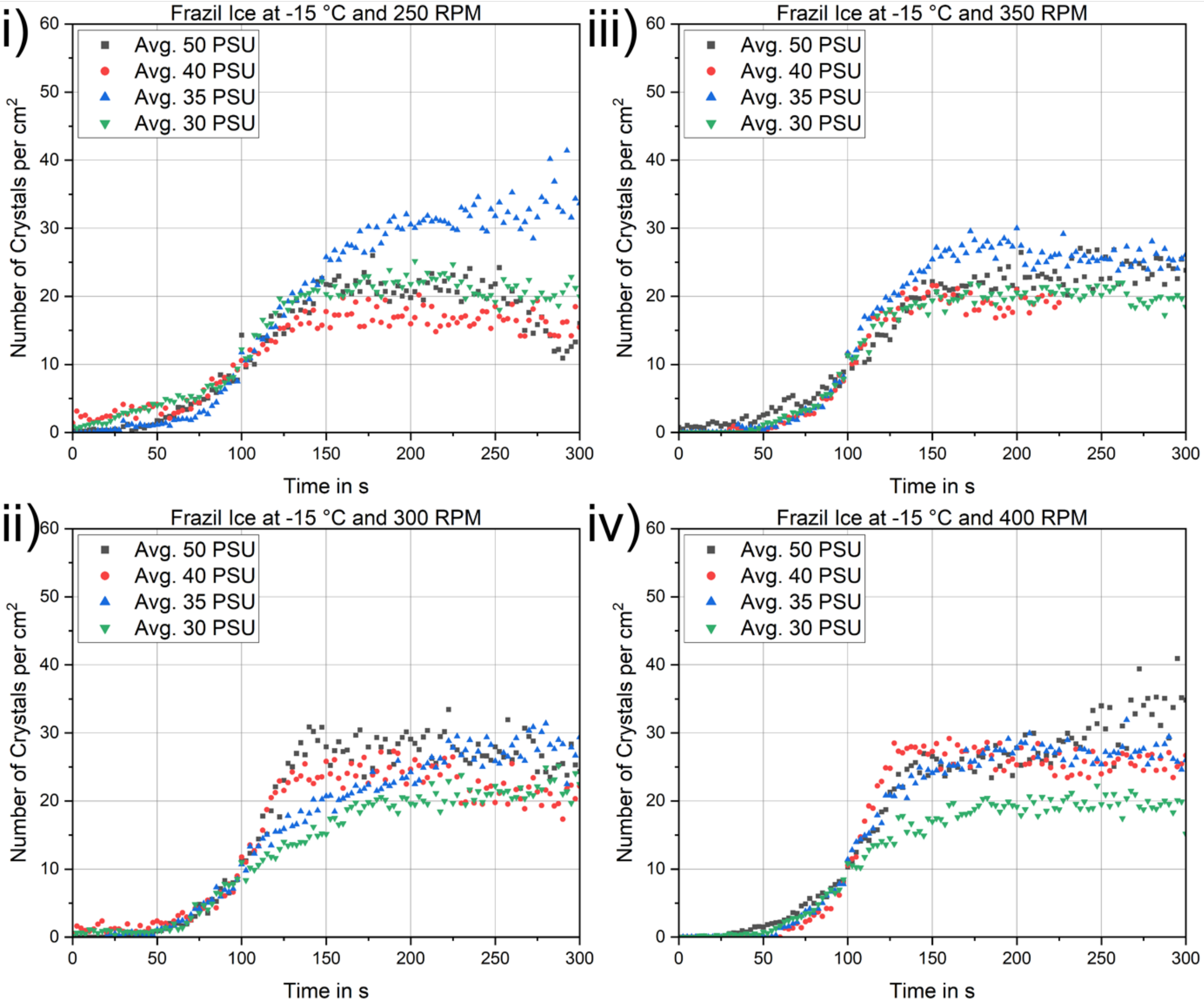

***Figure A 5** Average number of crystals per cm^2 for i) 250 RPM, ii) 300 RPM, iii) 350 RPM and iv) 400 RPM at different water salinities.*

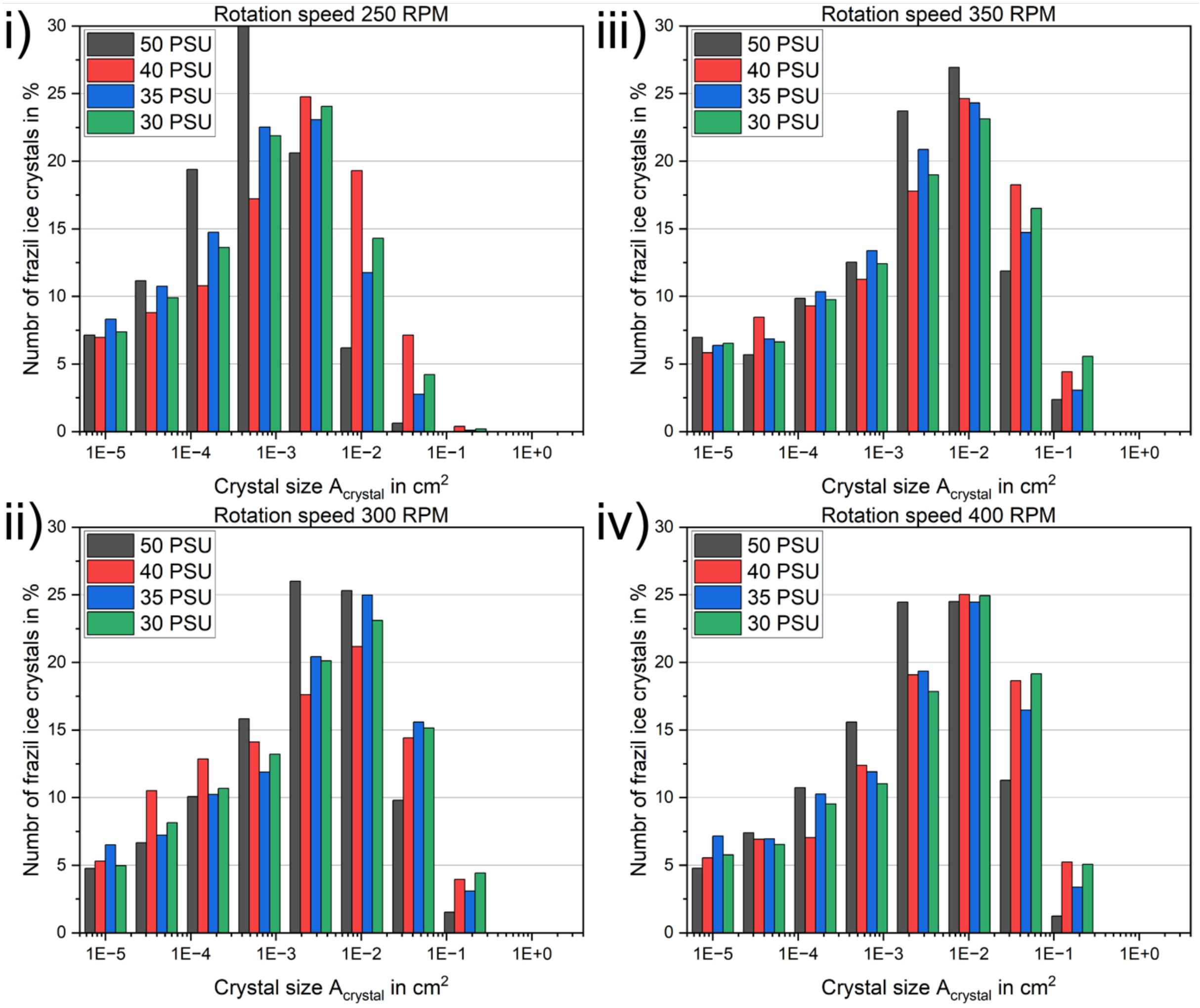

Figure A 6 *Water with varying salinity at -15 °C at i) 250 RPM, ii) 300 RPM, iii) 350 RPM and iv) 400 RPM.*

SCALE Spring Cruise 2019								
Name core	Length Core	Name sample	Length sample	Position from top	Max. force	Strength	Young's Modulus	Strain Rate
			l	d	F_c	σ_c	E	$\dot{\epsilon}$
	m		**m**	**m**	**kN**	**MPa**	**GPa**	**s^{-1}**
MIZ2-DE-07	0.51	MIZ2-DE-07-A	0.135	0.10	13	2.01	0.1	6.3E-04
	0.51	MIZ2-DE-07-B	0.135	0.24	32	5.03	-	6.5E-04
	0.51	MIZ2-DE-07-C	0.135	0.37	62	9.79	-	-
MIZ2-DE-08	0.55	MIZ2-DE-08-A	0.135	0.11	16	2.59	0.3	3.9E-04
	0.55	MIZ2-DE-08-B	0.135	0.24	54	8.41	0.5	-
	0.55	MIZ2-DE-08-C	0.135	0.38	53	8.35	-	-
MIZ2-DE-09	0.52	MIZ2-DE-09-A	0.135	0.11	19	3.00	0.2	8.3E-04
	0.52	MIZ2-DE-09-B	0.135	0.24	29	4.56	-	9.4E-04
	0.52	MIZ2-DE-09-C	0.1	0.46	57	8.90	0.3	7.1E-04
MIZ3-DE-01	0.59	MIZ3-DE-01-A	0.135	0.10	13	2.05	0.1	1.0E-03
	0.59	MIZ3-DE-01-B	0.135	0.23	54	8.54	1.2	6.4E-04
	0.59	MIZ3-DE-01-C	0.135	0.37	74	11.68	1.1	2.5E-04
	0.59	MIZ3-DE-01-D	0.135	0.50	50	7.90	0.9	-
MIZ3-DE-02	0.63	MIZ3-DE-02-A	0.135	0.09	17	2.60	0.1	7.0E-04
	0.63	MIZ3-DE-02-B	0.135	0.22	60	9.43	0.5	5.8E-04
	0.63	MIZ3-DE-02-C	0.135	0.38	88	13.83	0.7	3.8E-04
	0.63	MIZ3-DE-02-D	0.135	0.51	65	10.17	0.5	3.8E-04
MIZ3-DE-03	0.81	MIZ3-DE-03-A	0.135	0.08	4	0.62	-	4.3E-03
	0.81	MIZ3-DE-03-B	0.135	0.25	13	2.02	-	5.8E-04
	0.81	MIZ3-DE-03-C	0.135	0.38	60	9.45	-	5.3E-04
	0.81	MIZ3-DE-03-D	0.135	0.58	69	10.79	-	1.3E-03
	0.81	MIZ3-DE-03-E	0.135	0.71	95	14.96	-	-
MIZ6-DE-00	0.57	MIZ4.2-DE-00-A	0.135	0.09	7	1.07	-	-
	0.57	MIZ4.2-DE-00-B	0.135	0.22	8	1.31	-	-
	0.57	MIZ4.2-DE-00-C	0.135	0.36	15	2.42	-	1.1E-03
	0.57	MIZ4.2-DE-00-D	0.135	0.49	27	4.27	-	1.1E-03
MIZ6-DE-01	0.6	MIZ4.2-DE-01-A	0.135	0.22	21	3.27	-	9.9E-04
	0.6	MIZ4.2-DE-01-B	0.135	0.35	44	6.92	-	-
	0.6	MIZ4.2-DE-01-C	0.135	0.49	74	11.58	-	-
MIZ6-DE-02	0.6	MIZ4.2-DE-02-A	0.135	0.25	18	2.82	-	9.1E-04
	0.6	MIZ4.2-DE-02-C	0.135	0.48	55	8.64	-	-
MIZ6-DE-03	0.57	MIZ4.2-DE-03-A	0.135	0.10	14	2.18	-	1.1E-03
	0.57	MIZ4.2-DE-03-B	0.135	0.30	18	2.82	-	1.0E-03
	0.57	MIZ4.2-DE-03-C	0.135	0.43	42	6.54	-	-
MIZ7-DE-01	0.69	MIZ7-DE-01-A	0.135	0.09	20	3.21	-	1.1E-03
	0.69	MIZ7-DE-01-B	0.135	0.22	19	2.99	-	1.1E-03

SCALE Spring Cruise 2019								
Name core	Length Core	Name sample	Length sample	Position from top	Max. force	Strength	Young's Modulus	Strain Rate
			l	d	F_c	σ_c	E	$\dot{\epsilon}$
	m		**m**	**m**	**kN**	**MPa**	**GPa**	**s^{-1}**
	0.69	MIZ7-DE-01-C	0.135	0.36	30	4.79	-	1.2E-03
	0.69	MIZ7-DE-01-D	0.12	0.52	36	5.59	0.4	1.3E-03
MIZ7-DE-02	0.66	MIZ7-DE-02-A	0.135	0.42	29	4.55	-	1.1E-03
	0.66	MIZ7-DE-02-B	0.135	0.55	36	5.65	-	9.7E-04
MIZ7-DE-03	0.75	MIZ7-DE-03-A	0.12	0.13	11	1.71	-	1.2E-03
	0.75	MIZ7-DE-03-B	0.135	0.32	14	2.27	-	9.4E-04
	0.75	MIZ7-DE-03-C	0.135	0.53	32	4.97	-	1.0E-03
	0.75	MIZ7-DE-03-D	0.135	0.66	51	7.96	-	9.0E-04
MIZ8-DE-01-A	0.45	MIZ8-DE-01-A-A	0.135	0.17	11	1.78	-	9.5E-04
	0.45	MIZ8-DE-01-A-B	0.135	0.30	18	2.75	-	8.4E-04
	0.45	MIZ8-DE-01-A-C	0.135	0.44	35	5.44	0.5	6.6E-04
MIZ8-DE-02-A	0.46	MIZ8-DE-02-A-A	0.135	0.17	17	2.68	-	-
	0.46	MIZ8-DE-02-A-B	0.135	0.39	51	8.08	2.8	1.1E-03
MIZ8-DE-03-A	0.47	MIZ8-DE-03-A-A	0.135	0.25	14	2.16	-	1.1E-03
	0.47	MIZ8-DE-03-A-B	0.135	0.38	21	3.36	-	1.0E-03
MIZ8-DE-01-B	0.84	MIZ8-DE-01-B-A	0.135	0.21	11	1.66	-	1.0E-03
	0.84	MIZ8-DE-01-B-B	0.135	0.48	6	0.88	-	-
	0.84	MIZ8-DE-01-B-C	0.135	0.61	14	2.16	-	9.7E-04
	0.84	MIZ8-DE-01-B-D	0.135	0.76	16	2.53	-	9.7E-04
MIZ8-DE-02-B	0.78	MIZ8-DE-02-B-A	0.135	0.17	14	2.16	-	1.1E-03
MIZ9-DE-01-A	0.64	MIZ9-DE-01-A-A	0.135	0.31	13	1.99	-	8.3E-04
	0.64	MIZ9-DE-01-A-B	0.135	0.44	22	3.43	-	1.3E-03
MIZ9-DE-02-A	0.62	MIZ9-DE-02-A-A	0.135	0.24	24	3.82	0.7	1.1E-03
	0.62	MIZ9-DE-02-A-B	0.135	0.37	24	3.74	-	1.3E-03
MIZ9-DE-03-A	0.57	MIZ9-DE-03-A-A	0.135	0.19	9	1.38	-	1.2E-03
	0.57	MIZ9-DE-03-A-B	0.135	0.32	16	2.58	-	1.2E-03

Table S 1 *Summary of compression samples tested on the SCALE Spring Cruise 2019.*

SCALE Winter Cruise 2022								
Name core	Length Core	Name sample	Length sample	Position from top	Max. force	Strength	Young's Modulus	Strain Rate
			l	d	F_c	σ_c	E	$\dot{\epsilon}$
	m		**m**	**m**	**kN**	**MPa**	**GPa**	**s^{-1}**
OD4-DE-1	0.380	OD4-DE-1-A	0.141	0.09	37	5.74	2.4	5.1E-04
OD4-DE-2	0.430	OD4-DE-2-A	0.134	0.10	10	1.64	0.7	6.6E-04
	0.430	OD4-DE-2-B	0.224	0.28	36	5.67	2.3	3.5E-04
OD4-DE-3	0.650	OD4-DE-3-A	0.130	0.12	31	4.93	1.6	8.0E-04
	0.650	OD4-DE-3-B	0.225	0.29	22	3.43	1.9	5.6E-04
	0.650	OD4-DE-3-C	0.192	0.55	24	3.75	1.6	5.5E-04
B1-DE-1	0.490	B1-DE-1-A	0.200	0.12	24	3.83	1.1	8.3E-04
	0.490	B1-DE-1-B	0.217	0.33	21	3.24	1.1	1.1E-03
B2-DE-1	0.310	B2-DE-1-A	0.220	0.18	35	5.51	2.1	4.9E-04
IO-DE	0.250	IO-DE-(RIDGE)	0.205	0.12	3	0.51	-	-
OD2-A-DE-1	0.390	OD2-A-DE-1-A	0.134	0.09	26	4.01	1.6	8.2E-04
	0.390	OD2-A-DE-1-B	0.223	0.27	29	4.55	2.1	5.8E-04
OD2-A-DE-2	0.530	OD2-A-DE-2-A	0.207	0.18	24	3.70	1.8	4.2E-04
	0.530	OD2-A-DE-2-B	0.140	0.41	17	2.65	1.5	6.4E-04
OD2-A-DE-3	0.480	OD2-A-DE-3-A	0.225	0.19	27	4.23	1.7	6.5E-04
OD2-B-DE-2	0.490	OD2-B-DE-2-A	0.223	0.20	24	3.73	1.9	4.4E-04
OD2-B-DE-3	0.480	OD2-B-DE-3-A	0.195	0.12	24	3.75	1.5	5.5E-04
	0.480	OD2-B-DE-3-B	0.140	0.35	26	4.04	1.4	5.7E-04
OD2-B-XP-2	0.800	OD2-B-XP-2-A	0.225	0.16	31	4.91	1.5	5.2E-04
	0.800	OD2-B-XP-2-C	0.200	0.66	19	3.01	1.5	4.1E-04
OD3-D-DE-1	0.510	OD3-D-DE-1-A	0.137	0.18	34	5.30	2.7	4.8E-04
	0.510	OD3-D-DE-1-B	0.225	0.40	32	4.96	-	-
OD3-D-DE-2	0.550	OD3-D-DE-2-A	0.227	0.19	32	5.00	4.8	2.5E-04
	0.550	OD3-D-DE-2-B	0.110	0.38	25	3.87	2.8	4.3E-04
OD3-D-DE-3	0.480	OD3-D-DE-3-A	0.132	0.18	31	4.95	1.6	5.4E-04
	0.480	OD3-D-DE-3-B	0.203	0.36	32	5.05	2.2	4.1E-04

***Table S 2** Summary of compression samples tested on the SCALE Winter Cruise 2022.*

Sample name	Flow index
	n
OD1-FR-01	-
OD1-FR-02	-
OD1-FR-03	-
ICE22-FR-01	-
ICE22-FR-02	-
ICE22-FR-03	-
OD2-FR-01	0.6
OD2-FR-02	-
OD2-FR-03	0.4
SB061-FR-01	0.1
SB061-FR-02	-
SB061-FR-03	0.3
SB062-FR-01	0.1
SB062-FR-02	-
SB062-FR-03	0.3

Table S 3 *Flow index n for samples from the SCALE Winter Cruise 2022.*